INFORMATION TO USERS

This reproduction was made from a copy of a document sent to us for microfilming. While the most advanced technology has been used to photograph and reproduce this document, the quality of the reproduction is heavily dependent upon the quality of the material submitted.

The following explanation of techniques is provided to help clarify markings or notations which may appear on this reproduction.

1. The sign or "target" for pages apparently lacking from the document photographed is "Missing Page(s)". If it was possible to obtain the missing page(s) or section, they are spliced into the film along with adjacent pages. This may have necessitated cutting through an image and duplicating adjacent pages to assure complete continuity.

2. When an image on the film is obliterated with a round black mark, it is an indication of either blurred copy because of movement during exposure, duplicate copy, or copyrighted materials that should not have been filmed. For blurred pages, a good image of the page can be found in the adjacent frame. If copyrighted materials were deleted, a target note will appear listing the pages in the adjacent frame.

3. When a map, drawing or chart, etc., is part of the material being photographed, a definite method of "sectioning" the material has been followed. It is customary to begin filming at the upper left hand corner of a large sheet and to continue from left to right in equal sections with small overlaps. If necessary, sectioning is continued again—beginning below the first row and continuing on until complete.

4. For illustrations that cannot be satisfactorily reproduced by xerographic means, photographic prints can be purchased at additional cost and inserted into your xerographic copy. These prints are available upon request from the Dissertations Customer Services Department.

5. Some pages in any document may have indistinct print. In all cases the best available copy has been filmed.

University Microfilms International
300 N. Zeeb Road
Ann Arbor, MI 48106

Kokkinos, Dimitrios S.

LIDAR SYSTEM USING POLARIZATION DISCRIMINATION TECHNIQUES FOR MOLECULAR AIR POLLUTION MONITORING

City University of New York PH.D. 1984

LIDAR SYSTEM USING POLARIZATION DISCRIMINATION TECHNIQUES FOR MOLECULAR AIR POLLUTION MONITORING

by

DIMITRIOS S. KOKKINOS

A dissertation submitted to the Graduate Faculty
in Engineering in partial fulfillment of the
requirements for the degree of Doctor of Philosophy
The City University of New York

1984

This manuscript has been read and accepted for the Graduate Faculty in Engineering in satisfaction of the dissertation requirement for the degree of Doctor of Philosophy.

7/13/84
date

Chairman of Examining Committee

7/31/84
date

Executive Officer

Professor Samir Ahmed

Professor John Cooney

Professor George Eichmann

Professor Jamal Manassah
Supervisory Committee

The City University of New York

TO MY WIFE

ANGELA

ABSTRACT

LIDAR SYSTEM USING POLARIZATION DISCRIMINATION TECHNIQUES FOR MOLECULAR AIR POLLUTION MONITORING

by

Dimitrios S. Kokkinos

Advisor: Professor Samir Ahmed

A differential absorption of scattered energy (DASE) Lidar scheme which uses polarization discrimination to distinguish between simultaneously backscattered Lidar return signals at two close lying wavelengths was conceived, analysed, designed and built into a complete Lidar system. The system was then successfully used to first test out critical basic design premises related to atmospheric backscatter processes, and then to demonstrate its practical viability in field measurements of atmospheric Nitrogen Dioxide.

Lidar outputs are emitted simultaneously at two close-lying wavelengths, orthogonally polarized. The output wavelengths correspond to a peak and trough in the absorption spectrum of the pollutant being monitored. The concentration of pollutant is determined by using polarization discrimination techniques to separate and measure the relative attenuations of the Lidar backscattered signals at each of the wavelengths as they traverse the

sample region.

The polarization discrimination system was built producing orthogonally polarized laser outputs at two close-lying wavelengths. A similar arrangement was designed for the Lidar receiver, where the separated signals were detected by separate photomultipliers. Measurements on backscatter depolarization, a factor of key importance in the approach used, were then carried out both in laboratory tests and field tests. Atmospheric field tests confirmed theoretical prediction and laboratory tests, and showed depolarization consistent with a picture of 180^{o} backscatter depolarization plus depolarization due to multiple scatter. The latter effect was the predominant one, and could be largely eliminated by reducing the optical receiver aperture to match the 1 miliradian divergence of the outgoing Lidar beam.

Under these conditions, the depolarizations measured in backscattered signals were of the order of 1 percent. Because of the relative nature of measurements used in the scheme, it is found that undesirable backscatter depolarization effects can be neglected as a practical source of error in a polarization discrimination DASE Lidar system.

Finally field experiments were carried out, to measure, from the laboratory window, concentrations of Nitrogen Dioxide at kilometer ranges over the upper East Side of Manhattan. The results of these experiments, which measured

pollution concentrations of low ppm demonstrated the viability of the polarization discrimination DASE Lidar system.

in conjuction with the error analysis, it is found that undesirable backscatter depolarization effects can be neglected as a practical source of error in a polarization discrimination DASE Lidar system.

Finally field experiments were carried out, to measure, from the laboratory window, concentrations of Nitrogen Dioxide at kilometer ranges over the upper East Side of Manhattan. The results of these experiments, which measured pollution concentrations of low ppm demonstrated the viability of the polarization discrimination DASE Lidar system.

ACKNOWLEDGEMENTS

I would like to express my gratitude to all the members of my doctoral committee. In particular, I would like to thank my mentor, Professor Samir Ahmed, for his support and guidance in the development of this work.

I would like to dedicate this thesis to my wife, Angela, whose patience, great support and understanding during the course of this undertaking encouraged me to attain my goals. Without her continuous encouragement, I doubt I could have completed this task.

Finally I am greatfull to my parents and my wife's parents for their continuous encouragement.

TABLE OF CONTENTS

Chapter 1		Page
	INTRODUCTION AND BACKGROUND	1
1.1	Introduction	1
1.1.1	The Air Pollution Problem	1
1.1.2	Air Pollution Monitoring	2
1.2	Lidar Systems for Air Pollution Monitoring	4
1.2.1	Introduction	4
1.2.2	Earlier Lidar Schemes	5
1.2.3	Differential Absorption of Scattered Energy (DASE technique)	7
1.3	Objective and Outline of the Work	9

Chapter 2		
	LIDAR TECHNIQUES AND THE NEED FOR POLARIZATION DISCRIMINATION	18
2.1	Introduction	18
2.2	Atmospheric Scattering and Absorption	21
2.2.1	Introduction	21
2.2.2	Rayleigh Scattering	22
2.2.3	Atmospheric Particles and Mie Scattering	25
2.2.4	Raman Scattering	32
2.2.5	Absorption and Fluorescence Scattering by Molecular Pollutants	34
2.2.6	Atmospheric Propagation	36
2.3	Lidar Schemes, and the DASE Approach	42
2.3.1	Basic Lidar Equations	42
2.3.2	Lidar Receiver Parameters	44

2.3.3	The Raman Lidar	49
2.3.4	The Fluorescence Lidar	52
2.3.5	The DASE Lidar Approach	54
2.3.6	Evaluation of Required Systems Parameters	59
2.3.6.1	Transmitted Signal Requirements	59
2.2.6.2	Pump Depletion	61
2.3	Requirement for Simultaneous Output	62
2.4	Polarization Discrimination Approach for DASE Lidar	65

Chapter 3

	BASIC PARAMERS OF POLARIZATION ATMOSPHERIC DEPOLARIZATION AND ERROR ANALYSIS	82
3.1	Introduction	82
3.2	Properties of Polarized Light	83
3.2.1	Basic Definitions - Linear Polarization	83
3.2.2	Elliptic Polarization	84
3.2.3	Polarization and Depolarization Factors	87
3.3	Depolarization Mechanisms Affecting the Lidar Return Signal	90
3.3.1	Introduction	90
3.3.2	Depolarization Due to Clear Air Turbulence	90
3.3.3	Depolarization due to Rayleigh Scattering Due to Atmospheric Molecules	93
3.3.4	Scattering by Symmetric and Nonsymmetric Particles where $\lambda \nmid < \rho$	97
3.3.5	Scattering by Large Particles	101
3.3.6	Combined Effects of Various Depolarization Mechanisms	106
3.4	Depolarization Error Analysis	109

Chapter 4

	POLARIZATION DISCRIMINATION LIDAR SCHEME	124
4.1	Itroduction	124
4.2	Optical Receiver	125
4.3	The Dye Laser	127
4.3.1	The Laser Head	127
4.3.2	Dye Laser Mechanism - Main Features and Practical Factors Effecting Operation	128
4.3.3	Intra-Cavity Grating for Wavelength Selection	130
4.4	Cavity Design	131
4.4.1	Introduction	131
4.4.2	Dielectric Coated Polarizing Beam Splitter	132
4.4.3	Air Spaced Glan Taylor Prism	133
4.4.4	Stability of Output	135
4.4.5	Polarization of Laser Output	136
4.5	Laser Beam Transmitted in the Atmosphere	137
4.6	Conclusion	138

Chapter 5

	EXPERIMENTAL RESULTS	155
5.1	Introduction	155
5.2	Depolarization Due to Mie Scattering - Laboratory Experiments with Smoke	156
5.2.1	Introduction	156
5.2.2	The Experimental Arrangement	157
5.2.3	Laboratory Measurements of Depolarization by Smoke	161
5.2.3.1	Results	163

5.2.4 Conclusions 164

5.3 Depolarization in Atmospheric Backscattered Lidar Signals and Receiver Field of View 166

5.4 Simultaneous two Wavelength Measurements of Atmospheric NO_2 171

Chapter 6

SUMMARY AND CONCLUSIONS 194
REFERENCES 198

LIST OF TABLES

Number		Page
1.1.1	Classification of Air Pollutants	2
1.1.2	Composition of the Clean Atmosphere near Sea Level	16
1.1.3	Summary of Selected Remote Sensing Techniques	17
2.2.1	Aerosol Models - Vertical Distribution	79
2.2.2	Aerosol Complex Index of Refraction	79
2.2.3	Rayleigh and Mie Scattering Coefficients	80
2.2.4	Typical Cross Section Values for Scattering Processes	80
2.3.1	Effective Reflectivity for Different Scattering Processes	81
3.3.1	Polarizabilties and δ Factors for Atmospheric Molecules	123
5.2.1	Principal Transmittance Values for HN-32 Polarizer for Visible Wavelengths	175
5.2.2	Operating Conditions for a Q428SA-25 Centronic Photomultiplier	177
5.4.1	Range,Resolution,NO_2 Pollution Concentration for Various Times during the Day.	193

LIST OF FIGURES

Number		Page
2.2.1	Geometrical View for Rayleigh Scattering	69
2.2.2	Radiation Polar Diagram for Rayleigh Scattering	69
2.2.3	Junge Particle Size Distribution for Continental Air	70
2.2.4	Normalized Particle Size Distribution for Aerosol Models	70
2.2.5	The Raman Process	71
2.2.6	NO_2 Absorption Spectrum	72
2.2.7	SO_2 Absorption Spectrum	73
2.3.1	Lidar Backscatter and Obtainable Depth Resolution	74
2.3.2	The Raman Scheme	75
2.3.3	The Fluorescence Scheme	75
2.3.4	The DASE Scheme	76
2.3.5	Beam Spreading	77
2.3.6	Beam Scintillation	77
2.3.7	Beam Steering	77
2.4.1a	Lidar Transmitter for Simultaneous Cross Polarized Operation	78
2.4.1b	Optical Receiver for Simultaneous Cross Polarized Operation	78
3.2.1	Orientation of the Electric Vector E at an Instant of Time, with respect to the Plane of Reference for a Wave Propagating along the -z Direction	118
3.2.2	Linearly Polarized Plane Electromagnetic Wave	118
3.2.3	Vibration Ellipse for Electric Vector	119
3.2.4	Variation in the Form of an Elliptical Vibration with Phase Difference	119

3.3.1	Coordinate System Used for Describing a General Case of Polarization	120
3.3.2	Field Scattered from Flat Surface Element at Distant Point P	120
3.3.3	Single Step 180^{o} Backscatter from Small Non-symmetric Particle where ρ is Comparable to λ	121
3.3.4	Multiple Scattering Effects Showing Two and Three Step Scattering Processes	121
3.3.5	Reduction in Multiple Backscatter Detected as a Function of the Receiver Acceptance Angle α and α'	122
4.1.1	Schematic for DASE Lidar System Utilizing Polarization Discrimination	140
4.2.1	The Optical Receiver System for Polarization Discrimination	141
4.2.1a	Photographs of the Optical Receiver	142
4.2.2	Fresnel Lens	143
4.2.3a	Transmission Characteristic for the Broad Band Filter Centered at 4478.5 Å	144
4.2.3b	Transmission Characteristic for the Broad Band Filter Centered at 4500 Å	145
4.3.1	Schematic of Flashlamp Pumped Dye Laser	146
4.3.2	Energy Level Structure for Typical Dye Molecule	146
4.3.3	Typical Flashlamp-pumped Dye-Laser Output Pulse	147
4.4.1	Optical Arrangement for Simultaneous Two Orthogonally Polarized Wavelength Output	148
4.4.2	Photographs of the Laser Head and the Cavity	149
4.4.3	Dielectric-Interface Polarizing Beam Splitter	150
4.4.4	Air-Spaced Glan-Taylor Beam Splitter Polarizer	151
4.4.5	Experimental Arrangement for Testing the Polarization of the Laser Outputs	152

4.5.1	Aluminum Mirror Arrangement to Ensure Minimum Depolarization	153
4.5.2	Experimental Arrangement for Testing Depolarization Properties in Mirrors	153
4.5.3	Photograph of the Laser Head and the Aluminum Mirrors Guiding the Output Beam through the Window to the Atmosphere	154
5.2.1	Experimental Setup for Depolarization Measurements of He-Ne Laser Light Scattered by Smoke Particles at Different Angles	173
5.2.2	Photograph of the Experimental Setup for Depolarization Measurements of He-Ne Laser Light Scattered by Smoke Particles	174
5.2.3	Dependence of the Principal Transmittances k_1 and k_2 on the Wavelength in the Visual Range for HN-32 Polarizer. The Vertical Scale is Linear in log(1/k).	175
5.2.4	Spectral Response of the He-Ne Filter Used in the Receiver for the Experiment of Scattering by Smoke Particles	176
5.2.5a	Typical Cathode Sensitivity vs Wavelength for Centronic Q4283SA-25 Photomultiplier	177
5.2.5b	Typical Anode Sensitivity and Gain vs Voltage for a Centronic Q4283SA-25 Photomultiplier	177
5.2.6a	Plarization Angle of the Incident Linearly Polarized Light with respect to the Plane of Scatteing (Horizontal)	178
5.2.6b	Orientation of the Semiaxes of the Polarization Ellipse, with respect to the Plane of Scattering, for Light Scattered by Smoke Particles	178
5.2.7	Depolarization of Linearly Polarized Light Scattered by Smoke Particles Vs the Polarization Angle of the Incident Light with respect to the Plane of Scattering, at Different Angles of Scattering	179
5.2.8	Orientation Angle of the Major Axis of the Polarization Ellipsis of Light Scattered by Smoke Particles, Vs the Incident Polarization Angle, for Different Scattering Angle. Comparison with the Case of Reflection at the Same Angle (Straight Line)	182

5.2.9a	Depolarization of Linearly Polarized Light Scattered by Smoke Particles Vs the Optical Thickness of the Scattering Medium	185
5.2.9b	Depolarization of Linearly Polarized Light Scattered by Smoke Particles Vs the Optical Thickness of the Scattering Medium	186
5.3.1	Field of View of the Optical Receiver vs Aperture Diameter	187
5.3.2a	Parallel and Cross Polarized Backscatter Components for 2 and 10 mm Receiver Aperture Sizes	188
5.3.2b	Decrease of Received Power for Receiver Aperture Sizes below 1 mm	189
5.3.3a	Depolarization of Backscattered Signal vs Receiver Field of View	190
5.3.3b	Logarithmic Variation of Depolarization with respect to the Field of View of the Receiver	191
5.4.1	Typical Lidar Returns at the two Wavelengths 4500 Å and 4478.5 Å	192

CHAPTER 1

INTRODUCTION AND BACKGROUND

1.1 Introduction

1.1.1 The air pollution problem

The dangerous effects of air pollution on health are well known and great attention is given to the matter especially in heavily populated areas. In general the steps by the appropriate agencies towards controlling the air pollution are:

1. Detection of the atmospheric pollutant (kind of pollutant, physical or chemical procedure of its formation, sources of the pollutant, consequences in the environment from possible increase of its concentration).

2. Observation of the pollutant concentration (find an accurate and cost efficient method for each pollutant to measure its concentration in atmospheric regions of interest permanently).

3. Control of the pollution (knowing the sources and the level of the pollutant from measurements, find possible ways to prevent the increase of the pollutant concentration above specific level).

Table 1.1.1 shows classification of atmospheric air pollutants, while Table 1.1.2 shows typical concentrations

in which air pollutants are found.

	Particulate Matter
Solids:	Dust, Fumes, Smoke, Aerosols
Liquids:	Droplets, Mists, Fogs, Aerosols
	Gases
True gases:	Ozone, oxides of N, Sulfur Dioxide, etc.
Vapors:	Gasoline, Paint solvents, etc.

TABLE 1.1.1 Classification of air pollutants.

1.1.2 Air pollution monitoring

It is apparent that developing methods and using the appropriate ones for air pollution measurements is an important step towards pollution control.

Pollution monitoring activities can be divided into the following basic approaches: Space activities including Satellite monitoring and Aerial sensing, and Ground activities including Remote monitoring, Continuous monitoring at fixed sites and Air sampling. Space activities are lowest in resolution and their accuracy may not be sufficient to address many monitoring problems. Air sampling is extremely labor-intensive, requiring large number of samples to determine the air pollution levels generally close to the ground. Continuous monitoring at fixed sites involve analysis of relatively small volume of air close to

the measuring device and therefore many fixed-site stations are required to cover a large area like a town. Also the last two approaches use wet chemical techniques with integration times varying from one minute to a few hours. The four monitoring approaches-satellite monitoring, aerial sensing, continuous monitoring stations and air sampling-offer decreasing perspective with increasing accuracy and precision. They also represent increasing costs.

Table 1.1.3 shows selected remote-sensing techniques[3] which may be used for pollution monitoring. These are classified as either active or passive techniques. In the active techniques a controlled light source is used while in the passive techniques the pollutant itself or sunlight scattered by the atmosphere serves as the light source. Advantages of remote sensing include a large distance between sensor and the pollution being monitored, thus avoiding distortions due to the presence of the sensor itself. They also offer the potential for large-scale surveys of environmental parameters and a wide range of measurements permitted by the diversity of sensors.

Instrumental remote-sensing methods have been used for air pollution measurements for the last two decades, initially utilising spectroscopic techniques. More recently the development of tunable lasers[4], with adequate energy and spectral purity, reached a stage of development meeting the remote monitoring source requirements. Since then tunable

laser sources have became a unique tool in air pollution monitoring applications[1] and atmospheric studies in general.

1.2 Lidar systems for air pollution monitoring

1.2.1 Introduction

By using laser techniques, atmospheric pollution can be studied in experiments of atmospheric backscatter or long-path absorption. The laser radar or Lidar (LIght Detection And Ranging) approach, offers particular advantages because of its single-ended nature and great flexibility. It is in general a technique for probing the atmosphere remotely using a laser as source of pulsed energy in typical radar fashion. The radar principle was first applied to atmospheric observations at light wavelengths as early as 1938[5]. Pulses of light generated by electric sparks were reflecled from clouds to determine their height by reference to the roundtrip time of the light energy. Similarly attempts were made later to probe the atmosphere[6,7]. The development of the pulsed laser, however, marked the beginning of major progress in optical radar techniques and in 1963 the first laser powered radar (Lidar) was used for meteorological purposes[8,9]. Since then a wide range of Lidar applications have been explored with increasingly sophisticated techniques.

1.2.2 Earlier Lidar Schemes

Lidar schemes were developed using single frequency solid or gas lasers initially, and tunable dye lasers more recently. Their operation is based on mechanisms of atmospheric scattering or absorption of light. The earliest Lidar scheme for detection of atmospheric constituents, based on Raman scattering was implemented in 1967[10-12]. In that scheme, to obtain adequate sensitivity, it was necessary to use high-power lasers, large receiveing lenses, good filtering techniques and expensive signal processing instrumentation. It had however relatively low sensitivity.

More sensitive Lidar schemes depend upon tuning of the wavelength of the incident illumination to some resonance absorption of the species to be measured. Those schemes include resonance Raman, long path absorption, resonance fluorescence, and the differential absorption of scattered energy (DASE) scheme. Using resonance Raman 10 to 1000 times stronger intensities of the backscattered signal can be achieved[13,14], than with non-Resonance Raman. Power requirements are still large, however, due to small optical cross sections for the Raman process.

Resonance fluorescence schemes based on the mechanism of fluorescence scattering by the molecular pollutants, were used initially for measurements of Sodium in the upper atmosphere[18]. Later they were used for NO_2 concentration measurements with relatively good sensitivity[19]. The fluorescence cross section is much larger than the Raman

(100 times for NO_2) but the power requirements are still too high, and its sensitivities are severely limited during the day, due to background noise.

Long path absorption[16,18] laser techniques were developed to determine the average pollutant concentration along a laser beam path, based on resonance absorption of the laser radiation by the pollutant molecules. That scheme was first developed in 1968[15] and was further analyzed as a double-ended long path absorption scheme by Kildal and Byer[16]. A similar scheme, but single ended, using topographical reflectors was demonstrated in 1974[17]. The long path absorption system has very good sensitivity but it does not give range resolved information.

Comparison of earlier laser molecular pollution monitoring schemes lead to following conclusions: Long path resonance absorption techniques, while capable of excellent sensitivities, provide only average pollutant density between measuring points, and require remote detectors or retroreflectors. Single ended schemes which use Raman or resonance fluorescence backscatter, which in principal are capable of remotely measuring pollutant spatial distribution, are in practice severely limited in range and sensitivity. In the Raman case, the backscattered signal is small. In the case of resonance fluorescence backscatter, while the backscattered signal is relatively large, it is spread over a fairly large optical bandwidth. Therefore attempts to improve sensitivity by improving signal to noise

ratio by decreasing receiver optical bandwidth, are negated by the consequent reduction of the signal of interest.

The Differential Absorption of Scattered Energy (DASE) scheme combines the sensitivity advantages of resonance absorption measurements, with measurements of atmospheric elastic backscatterer to provide a generally more sensitive single-ended method of obtaining pollutant spatial distribution. The improvement and extention of DASE scheme through the development of Lidar polarization discrimination techniques is the basic topic of this thesis.

1.2.3 Differential absorption of scattered energy (DASE) technique.

The DASE scheme was first suggested by Schotland in 1964 using a searchlight as a source[20]. He also performed the early experimental work using lasers to measure the water vapor vertical profile by the DASE method[21]. The method was developed for Lidar schemes for pollution monitoring by Ahmed, Gergeley, Igarashi and others[16,22-29].

Basically, the DASE technique is used to determine the concentration of a pollutant in a sample region in space by comparing the relative attenuation of laser signals at two different, though close-lying, wavelengths as they traverse the same region twice, both as outgoing signal and backscattered return signal. Each of the signal wavelengths corresponds to a peak and a trough in the absorption spectrum of the molecule being monitored. The relative

attenuation at each wavelength is obtained by purely relative measurements of the backscattered return signals from the beginning and end of the sample lengths. Important factors affecting the potential of DASE Lidar systems are available spectrum and output powers of the lasers. Three types of laser operation have been considered in conjuction with the DASE method:

1- Broad band laser oscillation overlapping the required two probe wavelengths[30],

2- alternate oscillation at the two narrow lines[27],

3- simultaneous two-wavelength operation[31].

It is apparent that both cases, 2 and 3, are more power efficient since the power is concentrated in narrow spectral regions at around the two wavelengths required for the DASE scheme, rather than distributed over wide spectral region. However, the rapidity with which the Lidar optical path changes, due to thermal effects and particle drift in the atmosphere, makes the simultaneous two wavelength approach[3] optimum as far as obtaining accurate real-time range-resolved Lidar pollution measurements.

In the past, DASE Lidar systems have used two narrow-band fixed wavelength filters mounted in the optical Lidar receiver to discriminate between the two close-lying probe laser wavelengths. This approach prevents the DASE technique from being readily used in a more versatile tunable wavelength mode. Furthermore, the requiments for two narrow-band filters makes the use of the DASE technique

impractical and difficult at near UV wavelengths where only relatively wideband filters are readily available (wideband filters are unable to discriminate between each of the close-lying wavelengths). This is of importance in the use of simultaneous two wavelength monitoring of several pollutants of importance, in particular Ozone and Sulfur Dioxide. To overcome these limitations, as well as evolve a new approach which is also expected to more generally extend the utility and application of DASE techniques, the polarization discrimination scheme was developed. This thesis is therefore concerned with the definition, analysis, design and demonstration of a polarization discrimination scheme for use with DASE Lidar techniques.

1.3 Objective and outline of the work

In the work carried out, the requirements and design parameters for a polarization discrimination DASE scheme were analysed and defined and the system was then designed and built, and its viability demonstrated in laboratory and field tests.

In the polarization discrimination approach, the two close-lying output wavelengths of the DASE Lidar are emitted orthogonally polarized to each other. As will be seen, it is found that these initial polarizations are sufficiently well retained in the signals elastically backscattered from the atmosphere, to permit the use of polarization discrimination techniques alone, to separate the two close-lying

wavelengths in the Lidar optical receiver. This retention of polarization is an essential requirement for the polarization discrimination scheme to work.

Any undesirable depolarization effects are shown to have negligible impact on the accuracy of measurements by the Lidar system. The polarization discrimination technique entirely negates the neccessity for using narrow band filters individually matched to each of the close-lying laser probe wavelengths. This makes the DASE Lidar scheme, in its most important simultaneous two wavelength mode of operation, more versatile and readily applicable to all wavelength regions, as well as improving its signal to noise ratio, for a given laser output, and, through the generation of orthogonally polarized laser outputs greatly reducing undesirable competition effects between the two output wavelengths, which otherwise result in unstable outputs.

The tasks accomplished in this work are summarized below:

1. The basic requirements for a polarization discrimination scheme were analyzed in the context of Lidar systems in general, and the DASE system in particular. Basic parameters were evolved for the polarization discrimination scheme.
2. To examine the basic feasibility of the polarization discrimination scheme, atmospheric scattering features and their effect in depolarization of backscatter were examined in some detail. Included in the examination was

Rayleigh backscatter from atmospheric molecules and water vapor, Mie (particulate) backscatter from particles with sizes both comparable and large with respect to wavelength, with symmetric and non-symmetric shapes, as well as multiple scattering processes. From this examination, it was determined that depolarization effects were to be expected primarily from 180^{o} backscatter from non-symmetric small particles as well as from multiple scattering (two-step) from particles of all sizes and shapes.

3. A comprehensive error analysis was also carried out to determine the impact of undesirable depolarization backscatter effects that may still be found to exist. Because of the relative nature of the measurements required with the DASE approach, it was found that undesirable depolarizations, if they are found to exist, can be expected to have minor impact on the accuracy of measurements.
4. The design and construction of a polarization discrimination scheme, suitable for use with DASE Lidar was undertaken and completed.
5. Laboratory tests on polarization retention and depolarization by particulate backscatter were carried out. Results showed a large degree of specularity in scattering, as far as polarization properties are concerned in scattering by large particles, and substantial retention of polarization for 180^{o}

backscatter.

6. Field tests using the Lidar system built were carried out to determine the degree of polarization retention and depolarization occuring with backscattered Lidar signals received. The results showed very low levels of depolarization, and parametric tests with receiver geometry showed the detected depolarization effects to be in conformity with the pictures developed earlier (2 above) and related primarely to multiple scattering effects. Furthermore, the field tests showed that the depolarization of backscattered signal is very small, and when taken in conjuction with the results of the error analysis (3 above), it is found to be negligible for polarization discrimination Lidar schemes.
7. The viability of the overall polarization discrimination DASE Lidar system was demonstrated in measurements of atmospheric NO_2 from the laboratory window at ranges of a few kilometers over the upper East Side of Manhattan.

To facilitate the task of the reader, and provide him orientation, a listing of the material covered in each Chapter of this work follows:

Chapter 1

The main aspects of air pollution problems are presented and different methods for pollution monitoring are compared. The possibilities of Lidar schemes are discussed and their

development described. The DASE Lidar system is described and its simultaneous mode of operation explained. The need for a polarization discrimination scheme for use in conjuction with the DASE Lidar is discussed and its potential advantages described.

Chapter 2

The diffential absorption of scattered energy (DASE) Lidar technique is first examined in the overall context of Lidar schemes in general. The DASE technique is then more specifically analyzed in conjuction with the related atmospheric scattering and absorption mechanisms and their polarization properties, and relevant DASE Lidar system parameters are evaluated. This is followed by a description of the basic approach and expected properties of the polarization discrimination technique, and the factors expected to have important impact on its application to the DASE scheme.

Chapter 3

An examination of atmospheric features is carried out to determine the degree of polarization retention in elastic backscatter. In this context scattering from atmospheric molecules (Rayleigh scattering) is first examined, then particulate (Mie) scattering from symmetrical and non-symmetrical particles, both small and large compared with wavelength, is examined. The primary mechanisms

expected to be responsible for depolarization of backscattered Lidar signal received are identified, as (non-symmetrical) 180^{o} backscatter, and multiple scattering (two-step). A comprehensive analysis is carried out to determine the impact on the accuracy of the polarization discrimination scheme of any undesirable depolarization effects that might still occur.

Chapter 4

The design and construction and principal features and components of the polarization discrimination DASE Lidar system are discussed.

Chapter 5

The results of laboratory and field tests are presented. Laboratory experiments on smoke, show that incident polarization is largely retained for 180^{o} backscatter by large particles, which show a large degree of specularity in scattering as far as polarization properties are concerned. Field tests on atmospheric depolarization carried out with the complete polarization discrimination DASE Lidar system out of the laboratory window, show that depolarization detected in backscattered Lidar signals is small, and primarily due to multiple scattering. The results of both laboratory and field tests confirm the theoretical picture developed in Chapter 3, while the results of the field tests show that depolarization of backscattered Lidar signals is

very small, and when taken in conjunction with the results of the error analysis, it is found to be negligible. Field tests are carried out with the complete system through the laboratory window, to measure atmospheric Nitrogen dioxide concentrations over the upper East Side of Manhattan, and demonstrate the viability of the polarization discrimination technique as applied to the DASE Lidar system.

Chapter 6

The main conclusions of the work are presented. The factors which are relevant to the polarization discrimination approach and the results of the experiments and their significance are summarized.

Constituent	Percent by volume	Parts per million by volume
PERMANENT GASES		
Nitrogen	78.084+.004	780,800
Oxygen	20.946+.002	209,400
Argon	0.934+.001	9,300
Neon		18.2
Helium		5.2
Krypton		1.1
Hydrogen		0.5
Nitrous oxide		0.3
Xenon		0.09
VARIABLE GASES		
Water vapor	0-7	
Carbon dioxide	0.033+.001	315
Methane		1.5
Carbon monoxide		0.075
Ozone		0.02
Ammonia		0.01
Nitrogen dioxide		0.011-.04
Sulfur dioxide		0.0002
Hydrogen sulfide		0.0002

TABLE 1.1.2 Composition of the clean atmosphere near sea level.

ACTIVE TECHNIQUES

Technique or Instrument	Spectral Region	Species or Parameter
Differential absorption	VIS,UV,IR	Many gases
Lidar	VIS	Opacity
LDV	IR	Velocity
Long-path Absorption	VIS,UV,IR	Many gases
Raman	VIS,UV	Many gases
Fabry-Perot Raman	VIS,UV	Some gases
Fluorescence	VIS,UV	Many gases

PASSIVE TECHNIQUES

Matched filter correlation	VIS,UV	NO_2,SO_2
Gas-filter correlation	IR	SO_2
Photography	VIS	Opacity
Vidicon	UV,IR	SO_2 and velocity
Heterodyne radiometer	IR	Many gases
Spectrometer	IR	Many gases

TABLE 1.1.3 Summary of selected remote-sensing techniques.

CHAPTER 2

LIDAR TECHNIQUES AND THE NEED FOR POLARIZATION DISCRIMINATION

2.1 Introduction

All Lidar techniques for the real time determination of the spatial distribution of molecular trace constituents in the atmosphere, rely on time resolved measurements of backscattered signals. Two basically different categories of Lidar techniques exist.

In the first category the backscattered signals are inelastically backscattered by the trace molecular constituents and are characteristic of these constituents. This category includes: Raman, Resonance Raman and Fluorescence.

In the second category the backscattered signals are the elastically backscattered returns of the outgoing transmitted signals and have relative intensities that are related to the absorption spectra of the pollutants in their path.

Previous work had shown that this second approach, the Differential Absorption of Scattered Energy (DASE) technique had the greater potential for accurately monitoring the density and spatial distribution of atmospheric molecular pollutants.

In its simplest form, the DASE scheme determines the

concentration of a pollutant (Figure 2.3.4), at an arbitrary point, located at distance r in space, by measuring the optical resonance absorption due to the pollutant across an incremental path length, Δr. The absorption across Δr is obtained from the relative attenuation of two collinear laser beams at close-lying wavelengths, λ_1, and λ_2, respectively on and off the resonance absorption of the pollutant molecule in question. From comparisons (at the receiver) of the Rayleigh and Mie atmospheric elastic backscatter from the two laser beams as they traverse Δr, the relative attenuation is determined. Appropriate temporal resolution at the receiver permits determination of r and Δr, the range and spatial resolution of the pollutant distribution, respectively.

Some of the advantageous features of this scheme include:

1. The received signal, due to elastic backscatter from the atmosphere is relatively large (compared to Raman or fluorescent backscatter) and easily detected. Furthermore since it is at the same narrow band frequency as the outgoing laser beam, relatively narrow band filters can be used in the receiver, improving attainable signal to noise ratios.
2. Since the polution concentration is determined by an absorption method, detection sensitivity is high even where required spatial resolution is high.

To extend the use of the DASE method, overcome some of

its limitations, and further generalize it, the work reported on in this thesis developed a polarization discrimination Lidar system which makes use of polarization properties of both transmitted and received signals to differentiate between the backscattered signals at the different wavelengths.

In the following sections, the basic parameters which affect pollution monitoring Lidar schemes are examined, particularly in the context of their impact on a DASE Lidar scheme using polarization discrimination. The examination includes the following:

- basic atmospheric scattering processes and their effects on polarization,
- a brief background discussion of Raman scattering,
- absorption and fluorescence scattering by molecular pollutants,
- atmospheric propagation, including attenuation, due to elastic scattering and molecular absorption (by pollutants),
- the basic Lidar equation relating received and transmitted signals,
- a brief background description of Raman and fluorescence Lidar schemes,
- a description of the DASE Lidar approach and evaluation of its system parameters in the context of specific typical values for the scattering, attenuation and propagation factors discussed above,

- Previous limitations of the DASE Lidar scheme,
- Polarization discrimination approach applied to the DASE Lidar system.

2.2 Atmospheric Scattering and Absorption

2.2.1 Introduction

The atmosphere contains particles which range from air molecules, molecules of pollutants and other trace constituents, dust and condensation nuclei to cloud drops, rain and snow. An optical beam propagating through the earth's atmosphere is attenuated and distorted by several mechanisms: scattering by molecules, fog, dust and other aerosols, absorption by aerosols and by various atmospheric molecular trace constituents,including pollutants, and diffraction or refraction by inhomogeneities in atmospheric composition and density.

Normally scattering is distinguished from diffraction, the distinction depending on the ratio of the size of the scatterer to the wavelength of the radiation involved. For ratios less than unity, scattering is said to occur. For ratios of the order of unity, diffraction effects are significant and for ratios greater than 10, ray reflection and geometric shadows begin to be important.

For laser beams at optical wavelengths (4000 - 7000 A) propagating in the atmosphere, scattering is normally the dominant mechanism and is especially important as far as depolarization is concerned. In the case of the polarization

discrimination DASE scheme, it is specifically the depolarization that occurs in 180^{o} backscatter with which we are concerned.

2.2.2 Rayleigh Scattering

Atmospheric scattering by particles with size small compared to the wavelength of the incident radiation is known as Rayleigh scattering. Rayleigh scattering theory has been developed for scattering of light by spherical particles of radius less than 1/10 the wavelength, λ, of the light, and for very small particles, such as molecules, which are not necessary spherical. In general when the dimensions of a particle is much smaller than λ it is the volume of the particle that is most important, the shape being of secondary importance. Based on the standard problem of an isotropic, homogeneous, dielectric sphere in a uniform field, Rayleigh theory gives the intensity and polarization distributions of scattered light at different scattering angles. Generally changes in polarization due to the process of scattering are considered with respect to a reference plane, which is usually defined by the propagation directions of both, the incident and the scattered wave.

A convenient geometrical view is depicted in Figure 2.2.1, where the incident wave is propagating along the z-axis, the scattering plane is fixed as the yz-plane, and the incident electric vector is in the xy-plane. The two components of the field, E_x, E_y are referred to as the

perpendicular and parallel components ($E_\perp, E_\parallel$), or in the case where the yz-plane is horizontal, as the vertical and horizontal components (E_V, E_H) respectively. If ϑ is the angle of scattering, and φ the polarization angle of the incident linearly polarized light, the intensity I' of the scattered radiation at range R will be the sum of two terms corresponding to the components of the $\underline{E}$ field, $E_\parallel$ and $E_\perp$[36]:

$$I'_\parallel = I_o \frac{9\pi^2}{R^2} \left(\frac{m^2-1}{m^2+2}\right)^2 \frac{V^2}{\lambda^4} \cos^2\vartheta \cos^2\varphi \qquad (2.2.1)$$

$$I'_\perp = I_o \frac{9\pi^2}{R^2} \left(\frac{m^2-1}{m^2+2}\right)^2 \frac{V^2}{\lambda^4} \sin^2\varphi \qquad (2.2.2)$$

and

$$I' = I'_\parallel + I'_\perp = I_o \frac{9\pi^2}{R^2} \left(\frac{m^2-1}{m^2+2}\right)^2 \frac{V^2}{\lambda^4} (\cos^2\vartheta \cos^2\varphi + \sin^2\varphi) \qquad (2.2.3)$$

where

I_o = the intensity of the incident wave

m = the index of refraction of the scatterer

V = the volume of the scatterer

λ = the wavelength of the incident radiation

and where

the polarization angle φ for the incident radiation is defined by:

$$(I_{o\perp}/I_{o\parallel})^{1/2} = \tan\varphi \qquad (2.2.4)$$

Now if we make the normal Rayleigh assumption that

scattering is by small isotropic dielectric particles, there will be no phase difference, introduced beween the two components as a consequence of the scattering. From Equations 2.2.1 and 2.2.2, the polarization angle φ' of the Rayleigh scattered radiation will be given by:

$$(I'_{\perp}/I'_{\parallel})^{1/2} = \tan\varphi' = \tan\varphi/\cos\vartheta \qquad (2.2.5)$$

Thus the polarization angle φ' will be rotated for all scattering angles except for forward and backscattering ($\vartheta=0^{o}$, $\vartheta=180^{o}$ respectively). Furthermore, for $\varphi=0^{o}$, $\varphi'=0^{o}$, and for $\varphi=90^{o}$, $\varphi'=90^{o}$. The incident polarization is therefore retained both in forward and backscattering as well as for any other scattering angle where the incident field is parallel or perpendicular to the plane of scattering. From Equation 2.2.1 it is also apparent that the maximum scatter intensity occurs for $\vartheta=0^{o}$ or $\vartheta=180^{o}$ i.e. for forward and backscattering respectively, and that for $\vartheta=90^{o}$ the scattered field has only a component perpendicular to the plane of scattering. Figure 2.2.2 is a polar diagram of the Rayleigh scattered radiation for linearly polarized incident radiation at $\varphi=45^{o}$.

As previously mentioned, the above results are based on the assumptions that Rayleigh scatterers are small, homogeneous, isotropic non absorbing spheres. If, however, the scattering particle is non isotropic, or absorptive, it will be characterized by a complex relative refractive

index. This results in a phase difference between the parallel and perpendicular component of the scattered field which therefore becomes elliptically polarized. In fact, light from a linearly polarized source is elliptically polarized after undergoing Rayleigh scattering in the atmosphere, since, as is discussed later there is anisotropy associated with atmospheric molecules.

2.2.3 Atmospheric particles and Mie scattering

Elastic scattering when due to particles with sizes comparable to or larger than the wavelength of the incident radiation is called Mie scattering. The scattered radiation in this process has the same frequency as the incident radiation. Mie scattering is highly variable as a function of particle size and wavelength. Mie scattering therefore varies greatly with changing atmospheric conditions, in contrast to molecular Rayleigh scattering which obviously remains fairly constant.

Minute particles of various substances in the solid and liquid state, of both natural and industrial origin, are always present in suspension in normal atmospheric air. Owing to the small size of many of the particles, they remain in a suspended state in the atmosphere for a long time, and are transported by vertical and horizontal streams of air. The collective term aerosol is applied to these dispersed particles. Side by side with these particles, under different specific conditions, larger particles of

moisture, as well as large particles of dust are also found in the atmosphere. A significant fraction of these act as so-called condensation nuclei, which are necessary for the formation of fog, clouds and the elements of precipitation (raindrops, snowflakes etc.). According to origin, aerosols may typically include:

- particles of soil and products of rock weathering,
- particles of organic origin (microorganisms, plant pollen, etc.),
- particles of smoke of industrial origin as well as those formed in forest and peat fires,
- volcanic dust ejected by active volcanos,
- sea-salt particles entering the atmosphere in the evaporation of sea spray,
- particles which are products of the operation of industrial enterprises,
- Cosmic dust formed during the vaporization of meteors,

The shape and density of Mie scatterers are important factors for their depolarization properties.

Size Distribution of Particles

Since Mie scattering depends on the size of particle, it is important to know the side distribution of the particles in the atmosphere for the development of Mie scattering models. The sizes of atmospheric aerosols have been found experimentally to be mostly in the range $0.001\mu m \leq r \leq 10\mu m$, where r is the particle radius. The size distribution is

determined to a considerable extend by coagulation and sedimentation (settling), processes. Coagulation controls the lower size limit. Below a certain size this process is so rapid that particles cease to exist as independent species almost immediately. Coagulation also controls the size distribution of "Aitken" particles ($r<0.1\mu m$). Sedimentation controls the upper size limit.

Based on experimental measurements, Junge[32] proposed a power law model for the size distribution of particles. The model considered that particles are distributed throughout the atmosphere by eddy diffusion and have upper size limit of 20μm radius for the atmosphere above a continental landmass. The model proposed the relationship:

$$N(r) = Cr^{-(v+1)} \qquad (2.2.6)$$

where C, v are fitting parameters ($2 \leq v \leq 4$). A typical curve for a distribution based on this method is shown in Figure 2.2.3. Distributions more closely related to the actual atmospheric aerosol size were developed by Deirmendjian[33], and serve as the basis for the models discussed below. Table 2.2.1 gives values for the vertical distributions for two such aerosol models describing clear and hazy atmosphere[34], corresponding to visibility of 23 Km and 5 Km, respectively, at ground level. The aerosol size-distribution function for both models is the same at all atmospheric altitudes and the relationship between the number density N(r) and the

particle radius is given by[34]:

$$\frac{N(r)}{\Delta r} = \begin{cases} C_1 r^{-4} & \text{for } 0.1\ \mu m < r < 100\ \mu m \\ C_1 \times 10^4 & \text{for } 0.02\ \mu m < r, 0.1\ \mu m \\ 0 & \text{for } r < 0.02\ \mu m \end{cases} \qquad (2.2.7)$$

This differs from Deirmendjian's model in that the large particle cutoff has been extended from 5 to 100 μm. This distribution is normalized with $\Delta r = 1 \mu m$ and $C_1 = 0.883 \times 10^{-3}$ (i.e. the integral over the whole size range becomes 1) and is shown in Figure 2.2.4. Multiplying the normalized distribution function by the values of N in Table 2.2.1 we can obtain the actual size distribution at any height in the atmosphere. The numbers in the table have been adjusted so that the optical properties of the atmosphere (i.e. attenuation) at $\lambda = 5000$ Å are identical to those predicted by the model. The highest concentrations of particles are recorded in cities and especially in industrial cities, where values up to 4,000,000 particles/cm^3 have been found.

Another important quantity for the atmospheric particles is the index of refraction and its variation with the wavelength of the radiation propagated. A complex index of refraction indicates finite conductivity (absorption) that increases as the imaginary part increases and is responsible for depolarization of linearly polarized radiation scattered by particles.

Refractive Index of particles

Values of the refractive index for aerosol particles are given in Table 2.2.2 based on experimental data for a clear atmosphere of 23 Km visibility, published by Voltz[35]. From the table it is apparent that for λ=4500 Å, $\hat{n}$=1.53-j0.005 that has very small imaginary part. Urban aerosols at sea level, actually have larger values of the imaginary part, typically 1.5-j0.03, in the visible region (as obtained from Department of Air Resources, N.Y.C.)

Mie Scattering Parameters

From the foregoing discussion it is clear that the aerosol parameters such as the index of refraction, size, shape, density and distribution are variable quantities in the atmosphere. For that reason only simplified models have been considered, especially for the particle shape, in theoretical studies of scattering by particles.

Mie theory was developed for spherical, homogeneous isotropic particles, dielectric or otherwise, with radius comparable to or larger than the wavelength of the incident radiation. Single scattering mechanism is also assumed, which as will be seen later is the predominant mechanism of concern to the Lidar schemes being investigated here. Considering Figure 2.2.1, again as a geometrical view of scattering for linearly polarized incident radiation, it can be shown that, based on the simplifying assumptions above, the two components of the scattered field perpendicular and

parallel to the scatering plane at range R, are given respectively by [36,37]:

$$I_{\perp}' = I_o \frac{\lambda^2}{4\pi^2 R^2} |S_{\perp}(\vartheta, \hat{n}, r)|^2 \sin^2\varphi = \frac{\lambda^2}{4\pi^2 R^2} i_{\perp} \sin^2\varphi \qquad (2.2.9)$$

and

$$I_{\parallel}' = I_o \frac{\lambda^2}{4\pi^2 R^2} |S_{\parallel}(\vartheta, \hat{n}, r)|^2 \cos^2\varphi = \frac{\lambda^2}{4\pi^2 R^2} i_{\parallel} \cos^2\varphi \qquad (2.2.10)$$

where I_o: the incident lineary polarized radiation

λ : the wavelength of the incident radiation

: the incident polarization angle

: the scattering angle

r : the radius of the spherical particle

$\hat{n}$: the index of refraction ($\hat{n}=n-jn'$)

$S_{\perp}$, $S_{\parallel}$: the amplitude functions

$i_{\perp}$, $i_{\parallel}$: the intensity functions

In the case of absorbing spheres with a complex refractive index, the amplitude function will be a complex quantity. Therefore in general there will be a phase difference between the two components $E_{\perp}$ and $E_{\parallel}$ of the scattered field which will therefore be elliptically polarized. From the above equations it is also apparent however, that, for $\varphi=0^o$, or $\varphi=90^o$, only parallel or perpendicular components exist respectively for the scattered field. Therefore, when the incident field is either parallel or perpendicular to the

scattering plane, the polarization is retained after single scattering. The polarization is also retained for $\vartheta = 0^{o}$, forward or $\vartheta = 180^{o}$, backscattering, because any plane can be considered as the scattering plane for those scattering directions. Using the theoretical results for spherical aerosol particles with radius r and index of refraction n, scattering intensity functions $i_1,(\hat{n},\vartheta,x)$ and $i_2(\hat{n},\vartheta,x)$ have been generated for different size papameter $x=(2\pi r/\lambda)$, at many scattering angles and indices of refraction $\hat{n}$.[36,37]. For known size distribution the intensity functions are averaged with respect to the distribution to give averaged Mie Scattered intensity components (designated by subscript M)

$$I_{\perp M} = I_o \frac{\lambda^2}{4\pi^2 R^2} \sin^2\varphi \int_{r_1}^{r_2} i_1(\hat{n},\vartheta,x)n(r)dr \qquad (2.2.11)$$

$$I_{\parallel M} = I_o \frac{\lambda^2}{4\pi^2 R^2} \cos^2\varphi \int_{r_1}^{r_2} i_2(\hat{n},\vartheta,x)n(r)dr \qquad (2.2.12)$$

In general, however, atmospheric scattering is not isotropic and particles are not spherical. Therefore a deviation from the theoretical results should be expected in experiments involving atmospheric scattering, depending on geographical location and atmospheric conditions. For those reasons empirical expressions have been developed to estimate values of atmospheric parameters related to scattering. Furthermore

the depolarization due to scattering by spherical particles of known size may not apply for atmospheric aerosols. The depolarization due to Mie scattering will be discussed in more detail in the next chapter, while estimated values for other atmospheric parameters will be discussed in the following sections.

2.2.4 Raman Scattering

In the previous sections, elastic scattering processes (Rayleigh and Mie) have been considered. In those processes there is no exchange of energy between the photons of the incident radiation and the molecules or atoms of the atmospheric constituents. Consequently the scattered radiation is of the same wavelength as the incident radiation.

In contrast, inelastic scattering is a process in which there is an exchange of energy between the incident photons and the molecules in the atmosphere.

Raman scattering is an inelastic process that can be considered as a detail of Rayleigh scattering. The portion of the incident light that is temporarily absorbed in the Rayleigh process does not raise the molecule to an excited energy level as in classical resonance absorption. The molecule, after absorption, is in a virtual excited state and generally, all the energy is re-emitted in very short time (10^{12} sec.), at the same wavelength as that of the incident light.

Raman scattered light is however, also emitted, from a small portion (10^{-2} - 10^{-6}) or less of the irradiated molecules, at slightly different wavelengths than the incident light. In the spectrum of monochromatic light scattered by molecules, the Raman lines are weak lines displaced from the line of the incident radiation. The intensity of Raman lines is proportional to the density of molecules. Raman scattering results from the excitation of either vibrational-rotational or pure rotational transitions in a molecule.

Raman lines at wavelengths greater than the incident (Stoke's lines) are due to light absorption by molecules in the ground state, and reemission from those molecules returning to an excited vibrational level, instead of a ground level. Raman lines at wavelenghts shorter than the wavelength of the incident light (Anti-Stoke's lines), are due to the process of absorption of photons by the molecules while being in an excited vibrational level, instead of ground level, and reemission from these molecules returning to ground level. Figure 2.2.5 shows the Raman process. The frequency shifts Δ of the Raman lines are characteristic of the molecules causing the scattering, and are important pieces of information for identification of the molecules. For atmospheric gases, Raman scattering intensity is very weak, due to the small portion of molecules emitting Raman radiation. For N_2 at atmospheric pressure one (1) part in 10^{10} of incident light is Raman scattered, over a 1 cm path

length[38]. When the exciting frequency is tuned near or close to a resonance of a molecule, the fraction of light absorbed increases, causing a proportional increase in the intensity (1000 times higher) of the scattered radiation. This process is described as resonance Raman scattering and can be better utilized than Raman scattering for Lidar applications, as discussed in section 2.3.3 below.

2.2.5 Absorption and Fluorescence scattering by molecular Pollutants

When molecules are illuminated by monochromatic radiation with a wavelength within their resonance absorption band, a portion of the radiation is absorbed (Resonance Absorption). Some of the absorbed radiation will be re-emitted as fluorenscence radiation by the molecules over a broad spectral range characteristic of the specific molecular species. In that process, each excited molecule decays by isotropically re-emitting a photon spontaneously. This fluorescence radiation will be in all directions and, generally, shifted toward the longer wavelength end of the spectrum and will resemble the absorption spectrum of the molecules.

Figures 2.2.6 and 2.2.7 show the absorption spectra for NO_2 and SO_2 respectively. Nitrogen Dioxide has a clearly structured absorption spectrum in the blue, with well defined peaks and troughs[42]. Sulfure Dioxide has strong, discrete and sharp absorption bands in the near ultraviolet

region.

For the design of the DASE system the absorption spectra of the molecular pollutants as well as the fluorensence spectra of the available dyes used in lasers must be carefully examined. With knowledge of their fluorescence spectra, the proper dyes can be selected to give maximum laser efficiency at the two close-lying wavelengths (peak and trough) selected in the resonance absorption spectrum of the pollutant. These two wavelengths must be close enough to assure approximately the same behavior for other factors affecting beam attenuation,namely wavelength dependent elastic scattering processes.

In the DASE scheme, as discussed earlier, the two Lidar signals are transmitted simultaneously at close-lying wavelengths. Of the two elastically backscattered signals received and compared at Lidar receiver, clearly that at the absorption peak will be diminished relative to that at the absorption trough. The bigger the difference in the absorption coefficients of the pollutant at the two selected wavelengths, the larger the difference in the backscattered intensities compared, and therefore the measurements will be more accurate, for the same density of pollutant.

Both the absorption spectra of NO_2 and SO_2 are particularly well suited for the DASE approach discussed. In NO_2 for instance, the absorption peak at 4478.5 Å is close to the absorption trough at 4500 Å, and the two make good candidates for this purpose.

2.2.6 Atmospheric Propagation

The atmosphere attenuates a transmitted optical beam by elastic (Rayleigh, Mie) and inelastic scattering and by molecular absorption. Transmittance of radiation in the atmosphere is complicated by the dependance of scattering and absorption on a number of different physical properties of the atmosphere. In general, for propagation of monochromatic radiation of intensity I_o, along an atmospheric path, the attenuation is given by

$$I = I_o \exp\{-\int_o^r \alpha dr\} \qquad (2.2.14)$$

where I is the intensity at distance r from the source, and α is the atmospheric volume extinction coefficient, at r, given by

$$\alpha = \alpha_R + \alpha_M + \alpha_{ABS} \qquad (2.2.15)$$

where α_R, α_M, α_{ABS} are the Rayleigh, Mie and absorption coeficients respectively. The optical interaction of the molecules or particles with the incident radiation can be better formulated in terms of cross sections.

Considering a single particle illuminated by parallel light, and assuming that particle density is low enough to ensure the validity of a single scattering approach, the scattered field has the character of a spherical wave,in

which energy flows outward from each particle. If I_o is the incident intensity, $k=(2\pi/\lambda)$ the wavenumber, then I, the intensity of the scattered light at large distance ,r, from the particle is given by

$$I = I_o \frac{F(\vartheta,\varphi)}{k^2 r^2} \qquad (2.2.16)$$

where $F(\vartheta,\varphi)$ is a function of the scattering direction (ϑ,φ). The total power scattered from the particle will be

$$(P_{tot})_{scat} = \int I dS = \int \frac{I_o F(\vartheta,\varphi)}{k^2 r^2} dS = I_o \int \frac{F(\vartheta,\varphi)}{k^2} d\Omega \qquad (2.2.17)$$

where $d\Omega$ is the scattering solid angle element. Since the total scattered power is constant, the integral is also constant and has dimensions of area. That integral is the cross section, C_{scat}, for the scattering process and is given by

$$C_{scat} = \frac{1}{k^2} \int F(\vartheta,\varphi) d\Omega \qquad (2.2.18)$$

and

$$I = I_o C_{scat} \qquad (2.2.19)$$

The total energy scattered in all directions is in fact equal to the amount of energy of the incident wave falling

on the area C_{scat}. Likewise the energy absorbed inside the particle may by definition be put equal to the energy incident on the area C_{abs} and the total energy removed from the original beam may by definition be put equal to the energy incident on the area C_{ext}. Then the law of conservation of energy requires that

$$C_{ext} = C_{scat} + C_{abs} \tag{2.2.20a}$$

or

$$C_{ext} = C_{sm} + C_{sr} + C_{abs} \tag{2.2.20b}$$

where the quantities C_{sm}, C_{sr}, C_{abs} are the scattering cross sections for Mie scattering, Rayleigh scattering and absorption respectively.

For identical particles with density N the attenuation due to scattering is given by

$$-\frac{dI}{dr} = NC_{ext}I$$

or integrating for distance r

$$I = I_o \exp \int_o^r NC_{ext}\,dr \tag{2.2.21}$$

and comparing the last equation with Equation (2.2.14), gives:

$$\alpha = NC_{ext} \tag{2.2.22}$$

Thus for identical particles of density N the volume extinction coefficient is proportional to the extinction cross section.

The scattering from molecules or particles in general is not isotropic. Thus the cross section is a function of direction, depending on ϑ, the scattering angle, and φ the polarization angle, as is defined in section 2.2.2 and shown in the geometric view for Rayleigh scattering Figure 2.2.1. In this case differential cross section σ is used

$$\sigma(\vartheta,\varphi) = d\sigma/d\Omega \qquad (2.2.23)$$

where the angles and are shown in the geometric view for Rayleigh scattering Figure 2.2.1.

The differential cross section for molecular Rayleigh scattering of polarized light is given by [28]

$$\frac{d\sigma_R}{\Delta\Omega} = \frac{\pi^2(n^2-1)^2}{3\lambda^4N^2}(\cos^2\vartheta\cos^2\varphi+\sin^2\varphi) \qquad (2.2.24)$$

where n is the refractive index, N the density of molecules and λ the wavelength. For backscattering the Rayleigh backscatter coefficient is given by

$$\beta_R = \frac{8\pi}{3} N\sigma_R(\pi) \qquad (2.2.25)$$

Mie scattering, as discussed earlier, is more complicated

depending on the geometrical and physical properties of the scatterers. Assuming that the size distribution and the physical properties of the scatterers are known, the volume extinction coefficient can be written as

$$\alpha_M(\lambda)=\int_o^r \sigma(r,\lambda,m)\ N(r)dr \qquad (2.2.26)$$

where σ is the scattering cross section, r the radius of the particle, λ the wavelength of the incident light, m is the index of refraction of the particles and N(r) the number density of particles. Since the particle size distribution is unknown, empirical expressions are normally used for $\alpha(\lambda)$. A useful empirical relationship for Mie scattering coefficient is given by [16]

$$\alpha(\lambda)_{Mie} = (3.91/V)\ (.55/\lambda)^{.585V^{1/3}}\ \ Km^{-1} \qquad (2.2.27)$$

where λ is the wavelength in μm, of the incident radiation, V is the visibility in Km.

The above expression is an approximation and may not hold under unusual atmospheric conditions. (i.e. high particulate concentrations)[28]. Typical values for Mie scattering coefficients based on the empirical formula, as well as for Rayleigh scattering coefficients, are given in Table 2.2.3. Table 2.2.4 shows values of scattering cross sections for the different processes of elastic and inelastic scattering.

The third parameter in the atmospheric volume extinction coefficient is absorption. For wavelengths longer than about 2500 Å in the visible region, no problems are normally encountered with atmospheric absorption, other than that due to molecular pollutants discussed later in section 2.2.5 and the range of the beam is limited by the elastic scattering loss. At wavelengths shorter than 2500 Å, oxygen absorption becomes important for longer pathlengths (>100 m), and at wavelengths shorter than 1850 Å the atmosphere is totally opaque. At heavy ozone concentrations additional obsorption occurs due to the wide ozone absorption bands between 2000 and 3000 Å. At an ozone concentration of 0.1 ppm the absorption compares with the oxygen absorption at 2500 Å.

In the infrared, the atmosphere has several absorption bands because of water vapor and CO_2 absorption which limits the useful spectral region to the atmospheric windows. For visibility 5km, relative humidity 75% and air temperature $60^{o}F$, the absorption in the window 4.3 to 6μm is 0.08 km^{-1} while the corresponding Mie scattering coefficient is only 0.08 km^{-1}.

Two other properties of the atmosphere are important in remote sensing. They are atmospheric scintillation and background signal levels during both daytime and nighttime operating conditions. Atmospheric background radiation is of concern in evaluating detector signal to noise and system receiving parameters, and is discussed in section 2.3.2. Scintillation is discussed at the end of Chapter 2 where

other effects of the atmosphere on laser beam propagation are considered.

In the previous discussion the atmospheric scattering and absorption processes were considered. In the following sections monostatic Lidar schemes for pollution monitoring utilizing those processes are discussed, including

1. The Raman Lidar
2. The Fluorescence Lidar
3. The DASE Lidar

The Raman and Fluorescence lidars are only briefly discussed for background purposes, and emphasis is given to the Differential Absorption of Scattered Energy (DASE) Lidar scheme and the development of polarization discrimination to improve and extend its capabilities.

2.3 Lidar Schemes, and the DASE approach

2.3.1 Basic Lidar Equations

In its basic form Lidar uses a laser as a source of pulsed energy. Laser light in short pulses (a few hundred nanoseconds in duration), is transmitted into the atmosphere, and light backscattered from molecules or particles is collected by an optical receiver telescope and detected by a photomultiplier. The resulting signal is observed as a function of the time starting from the transmission of the pulse, in radar fashion, and is typically displayed on an oscilloscope.

For a Lidar, the backscattered optical signal, $P_r(R)$, received from range R is of the form[22]

$$P_r(R) = K(\rho/\pi)\frac{A}{R^2} P_o \exp\{-2\int_o^R \alpha(r,\lambda)dr\} \qquad (2.3.1)$$

where

K = The optical effiency of the receiver telescope,

(ρ/π) = the effective reflectivity of the remote target,

A = The optical telescope area,

p_o = the transmitted power,

$\alpha(r,\lambda)$ = the volume extinction coefficient, which is composed of a sum of terms due to atmospheric scattering , absorption and pollutant absorption.

The effective reflectivity term (ρ/π) in Equation 2.3.1 is for a Lambertian topographical reflector.[22] When the signal is backscattered from a distributed reflector, consisting of atmospheric molecules and particles, the corresponding reflectivity can be thought of in terms of an equivalent topographical reflectivity. For comparison purposes, Table 2.3.1 shows the equivalent topographical reflectivities for different types of Lidar schemes.

The depth resolution ΔR attainable from time-of-flight measurements in conjuction with backscatter methods is seen in Figure 2.3.1 to be given by:

$$\Delta R = \frac{c\tau}{2} \qquad (2.3.2)$$

where τ is in general the sum of the laser pulse width τ_P, the detector integration time τ_D and in the case of fluorescence Lidar schemes the fluorescence lifetime τ_F.

The expression $P_o \exp\{-2\int^R \alpha(r,\lambda)\} dr$ in Equation 2.3.1 accounts for the attenuation due to scattering and absortion processes, of the transmitted pulse out to range R and is common to all Lidar schemes.

2.3.2 Lidar Receiver parameters

Before considering the relative merits of each different Lidar scheme, the parameters related to the detection of received signal, which are common to all schemes, need to be considered. These include sources of noise etc. and determination of minimum detectable levels of received power.

In most Lidar receivers, the low level backscattered light is collected by a receiver telescope and then detected by a photomultiplier (PMT). The noise in Lidar receivers may arise from background radiation, from photon generated shot noise and dark currents. Those different factors are considered below:

Background and Shot Noise in the photomultiplier

An important source of noise in a Lidar system may be due a background of scattered radiation of sunlight etc. This sky background noise is considered in the following discussion. In this situation the background noise can be

considered to come from extended source filling the field of view. The background power, P_B, at the receiving mirror, due to an extended source filling the field of view is given by 28

$$P_B = T_\lambda \, \Delta_\lambda \, \Omega \, A \, B(\lambda) \qquad (2.3.3)$$

where

T_λ = The atmospheric transmittance at λ,

Δ_λ = the optical bandwidth of the detection system,

Ω = the field of view of the receiver, (solid angle),

A = the area of the receiving optics,

$B(\lambda)$ = the spectral radiance of the background source,

The spectral radiance of the clear daytime sky peaks in the visible due to scattered solar light at a value approximately 10^{-2}(W cm^{-2} μm^{-1} sr^{-1}). In Infra-red, the spectral radiance again peaks due to thermal radiation near 13 μm at approximately 10^{-3} W cm^2 μm^{-1} sr. Below 3000 Å the ozone absorption layer in the upper atmosphere screens the solar radiation, thus producing an effective night condition. Equation 2.3.3 shows that the background signal is reduced by decreasing the field of view, the optical bandwidth and the receiver area. In a receiver of the type used in this work, the daylight background noise in the 4500 Å region is of the order of 10^{-9} Watts.

The other two sources of noise in the photomultiplier are photon noise from the detected signal (Shot noise) and

internally generated dark current-noise.

For shot-noise limited detectors the signal-to-noise ratio, S/N, for single pulse, is given by[40]:

$$\frac{S}{N} = \frac{i_S^2}{2qB(i_S+i_D+i_B)} \tag{2.3.4}$$

where

i_S, i_B, i_D are the average photodetector currents due to signal radiation, background radiation and dark current, respectively, and

B = the electrical bandwidth of the detection system,

q = the electronic charge.

Introducing a detector sensitivity S_d, the signal and background radiation powers P_S and P_B are proportional to i_S and i_B respectively:

$$i_S = S_d P_S \quad \text{and} \quad i_B = S_d P_B \tag{2.3.5}$$

Depending on which source gives the largest contribution, the detectors are said to be photon shot noise, background or dark-current limited. If the minimum acceptable signal-to-noise ratio is $(S/N)_{min}$, the detector is dark current limited when[16]

$$2qB(S/N)_{min} < i_D \tag{2.3.6}$$

for single pulse operation. The minimum detectable power,

$P_{r,min}$ would be given by[16]:

$$P_{r,min} = \frac{2qB(S/N)_{min}}{S_d} \qquad (2.3.7)$$

For photon noise limited detection the opposite of Equation 2.3.6 is true, i.e.

$$2qB(S/N)_{min} > i_D \qquad (2.3.8)$$

and the minimum detectable signal power, $P_{r,min}$, would be[16]:

$$P_{r,min} = \frac{2qB(S/N)_{min} i_D^{1/2}}{S_d} \qquad (2.3.9)$$

Now the detector available for the experiments, the Amperex 56 AVP, has $S_d = 60 \times 10^{-3}$ A/W, a Bandwidth of 3 MHz and and $i_D = 15$nA. If the minimum acceptable signal to noise ratio is conservatively set at 10, then substituting in Equation 2.3.8, the detector is found to be dark current and/or background radiation limited. Under these conditions the minimum detectable signal power P_r,min is found from Equation 2.3.9 to be 6.32×10^{-9}W, for dark current limited detection. For the Lidar system used in the experiments, this represents a higher power than the background noise (10^{-9}W) in the 4500 Å region, and dark current limits, are therefore the dominant ones.

Now the minimun detectable change, $\Delta P_{r,min}$ relative to

the received signal power at the detector, for a dark current limited system, is given by[16]:

$$\frac{\Delta P_{r,min}}{P_r} = \frac{4qB}{S_d P_r} \left(\frac{S}{N}\right)_{min} \left(1+\frac{i_D}{S_d P_R}\right)^{1/2} \qquad (2.3.10)$$

For the Amperex 56 AVP, if the minimum acceptable signal-to-noise ratio is maintained at 10, and it is conservatively assumed that a 5 percent change in the received signal is the minimum that can be measured accurately, Equation 2.3.10 shows that the total received power into the photomultiplier must be at least 0.25 μWatts. This limitation, set by dark current values is much higher compared with powers of the order of 10^{-9} Watts for background noise.

The receiver requirements, discussed above, and the impact they have on the overall Lidar system will be further examined in detail in the context first of the Raman and Fluorescence schemes, and then in more detail in the DASE scheme, first without polarization discrimination, then with polarization discrimination. Evaluation of system parameters are carried out in all cases for the detection of NO_2, in the 4500 Å region. As equipment was available, this was the spectral region chosen for the development of the polarization discrimination scheme.

2.3.3 The Raman Lidar

The Raman scheme shown in Figure 2.3.2 determines the concentration of the pollutant at any arbitrary point in space by measuring the backscattered radiation at the characteristic Raman shifted frequencies. Using the expression of the effective reflectivity for Raman scattering (Table 2.3.1) in the basic Lidar equation 2.3.1, and assuming a free atmosphere up to the sampled region, ΔR, the received backscatter power, $P_r(R)$, from distance R is given by

$$P_r(R)=KP_oF\frac{c\tau\sigma_{RAM}(\lambda)N_r}{8\pi}\left(\frac{A}{R_2}\right)\exp\left\{-2\alpha_{sc}R-\sigma_{ABS}(\lambda)\bar{N}_r\Delta R\right\} \quad (2.3.11)$$

and

$$\alpha_{SC} = \alpha_R + \alpha_M$$

where

σ_{RAM} = The Raman cross section,

$\bar{N}_r$ = the average pollutant concentration over the sampled region ΔR,

F = the fraction of the total Raman scattering detected by the receiver.

α_{SC}, α_R, α_M = the total, the Rayleigh and Mie atmospheric volume scattering coefficients without absorption respectively, averaged over ΔR.

The other quantities have been previously defined in section 2.3.1.

The Raman differential cross section is given by[16]:

$$(d\sigma/d\Omega)_{RAM} = (1/2\pi\varepsilon_o c^2)^2 \ \nu_1 \nu_2 r^2\alpha^2 \qquad (2.3.12)$$

where

ν_1 = the pump frequency,

ν_2 = the Raman frequency,

$r\alpha$ = the Raman polarizability,

To obtain the minimum detectable power 6.32×10^{-9} Watts at the Amperex AVP 50 photomultiplier receiver (discussed in section 2.3.2) from Raman backscatter and a very low average pollution concentration of, say, 0.03 ppm of NO_2 over 100 meters at a range of 1000 meters, Equation 2.3.11 yields a required transmitted power of 1.8×10^{9} MW, or 4.43×10^{7} J of energy for the typical flashlamp-pumped dye laser pulse. This is very large indeed as will be seen in comparison to the DASE schemes. To detect more typical pollution levels of 0.1 ppm, the power and energy requirements are reduced by approximately a factor of 3.

Resonance Raman

To reduce transmitted power requirements the Lidar can be operated in the resonance Raman mode. The expression for the Resonance Raman cross section $(d\sigma/d\Omega)_{RES}$ is given approximately in terms of the Raman cross section $(d\sigma/d\Omega)_{RAM}$ by[16]:

$$\left(\frac{d\sigma}{d\Omega}\right)_{RES} = \left(\frac{d\sigma}{d\Omega}\right)_{RAM} \frac{\nu^2}{(\nu_1 - \nu_o)^2 + (\Delta\nu/2)^2} \qquad (2.3.13)$$

Where

ν_o = the electronic transition frequency

ν_1 = the laser pump frequency, and

$\Delta\nu$ = the linewidth of the electronic transition.

For NO_2 at a pump frequency $\nu_1 \simeq \nu_o = 6.69 \times 10^{14}$ Hz and $\Delta\nu = 2.24 \times 10^{12}$ Hz, Equation 2.3.13 yields Resonance Raman cross section of 1.21×10^{-23} cm^2. Inserting the value for the resonance Raman backscattering cross section into Equation 2.3.11 and evaluating the expression for 0.03 ppm NO_2 concentrations as for Raman case, the value 504 Mw(126j) is obtained for the required transmitted power. Again, if more typical concentrations of 0.1 ppm are used, power and energy requirements are reduced by a factor of 3 approximately.

The limitations of the Raman and resonance Raman schemes are summarized below.

1. The cross sections for Raman backscattering are 10 to 10^3 smaller than the Rayleigh and Mie backscattering cross sections.
2. The cross section for resonance Raman backscatter is larger that the sum of Rayleigh and Mie backscattering cross-section (1.21×10^{-23} cm^2 as compared to 3.21×10^{-28} respectively for NO_2). However the strength of the

resonance Raman return signal, as a function of the corresponding backscattering coefficient depends, upon the concentration of the molecular pollutant. Therefore, the advantage of large resonance Raman cross section is lost for low concentration of pollutant, since, the strength of the elastically backscattered signal depends upon the concentration of the atmospheric molecules and particles, which is much higher than the average pollutant concentration.

3. Interference due to the Raman backscatter of other atmospheric species along with large amounts of backscattered power in the form of elastic scattering and resonance fluorescence, puts limits on the use of the Raman scheme. Sensitive pollution concentration measurements would require increased transmitted power because of the necessity to reject these forms of interference.

2.3.4. The Fluorescence Lidar

The fluorenscence scheme shown in Figure 2.3.3 determines the pollution concentration at a distance r in space by measuring the fluorescence backscatter from pollutant molecules emitted after absorption of energy from the incident Lidar beam.

The effective fluorescence cross-section σ_F is given in Table 2.2.4 for several common molecular pollutants. The value of σ_F is determined by:

$$\sigma_F = \frac{\sigma_{ABS}(\lambda)\ t_{COL}\ z}{(1+(t_{SP}/z\ t_{COL})\ t_{SP}} \qquad (2.3.14)$$

where

$1/z$ = the probability of quenching per collision,

t_{COL} = the collision time, and

t_{SP} = the spontaneous decay time,

Quenching caused by collisions with other molecules in the atmosphere, reduces the fluorescence intensity and shortens the decay time of the re-emission. Substituting Equation 2.3.14 into 2.3.1, yields:

$$P_r(R) = (c\tau_F/2)KP_o\sigma_F(\lambda)N_rF\ A/4\pi R^2\ X$$
$$\exp\{-2\alpha_{SC}(\lambda)R - \sigma_{ABS}\bar{N}_r\Delta R\} \qquad (2.3.15)$$

where F is the fraction of the total fluorescence detected by the receiver and the other quantities as previously defined, in section 2.3.1 and 2.3.2.

For an average low pollutant concentration of 0.03 ppm across the sampled region, and a range of 1000 m, F=1 (Detection of the entire background spectrum), a depth resolution of 100 meters and a mininum detectable received power 6.32×10^{-9} W (for dark current limited detection), the required transmitted power turns out to be 382 MW (95.5 J, energy for typical dye laser pulses). During daytime operation, the blocking of the background radiation noise is necessary, and that results in reduction of the useful

fluorescence signal. Thus for a typically required reduction of F to F=0.1 at daytime operation, a transmitted energy of 995 J is required to detect 0.03 ppm. For a more typical average NO_2 concentration of 0.1 ppm yields a required transmitted power of 0.352 MW (8.8×10^{-2} J) for nightime operation and 1.4 MW (3.52×10^{-1} J) for daytime.

As can be seen the resonance fluorescence backscatter scheme suffers from the disadvantage that the detection sensitivity is severely limited for daytime operation, and in any event, as will be seen in the next section, very much higher pulse energies are required to achieve the same results as the DASE scheme.

2.3.5 The DASE Lidar approach

The previous two schemes, i.e. Raman and fluorescence backscatter, are capable of abtaining spatial distribution of pollutants. However their detection sensitivities are relatively low. On the other hand, long path optical absorption techniques, [16,38] which are capable of excellent sensitivities in the measurement of average pollutant concentration (along a probe beam path), do not give information on spatial distribution.

The DASE technique, briefly introduced in section 2.1, is used to determine Figure 2.3.4 the concentration of an atmospheric molecular pollutant at a distance r, averaged over a path length Δr, by comparing the relative attenuation of the elastically backscattered signals at two

laser wavelengths. One wavelength, λ_1 corresponds to an absorption peak of the pollutant to be measured, while the other wavelength , λ_2, corresponds to a trough, (as shown in Figure 2.2.6 for NO_2). The DASE scheme combining the advantages of resonance absorption measurements with those of elastic backscatter measurements, is a sensitive method of obtaining pollutant spatial resolution. The pollutant concentration is determined by an absorption method, thus achieving high detection sensitivity, even if high spatial resolution (100m) is required. Furthermore, the relative attenuation of the two collinear laser beams, as they traverse the sample length Δr, is easily detected, since it is determined from comparison (at the optical receiver) of elastically backscattered signals (at the same wavelengths as the transmitted signals) which are relatively large. The two close-lying wavelengths λ_1 and λ_2 can be easily achieved using tunable dye lasers.

For the DASE case the effective reflectivity of the atmosphere, as shown in Table 2.3.1 is given by:

$$\rho/\pi = (c\tau_P/2)\ \beta_R(R,\lambda)+\beta_M(R,\lambda) = (c\tau_P/2)\beta_E(R,\lambda) \quad (2.3.16)$$

where

$\beta_R(R,\lambda)$, $\beta_M(R,\lambda)$, $\beta_E(R,\lambda)$ are the Rayleigh, Mie and total Elastic backscatter coefficients respectively, at range R and wavelength λ, and

c = the speed of light

τ = the laser pulse length.

Using the above expression for the reflectivity and the basic Lidar equation, the received power $P_r(R,\lambda)$ from range R at wavelength λ, is given by:

$$P_r(R,\lambda) = (c\tau_p/2)\beta_E(R,\lambda)kP_o(\lambda)(A/R^2)\exp\{-2\int^R \alpha(r,\lambda)dr + \sigma_{ABS}(r,\lambda)N_r(r)\} \quad (2.3.17)$$

and

$$\alpha(r,\lambda) = \alpha_R(r,\lambda)+\alpha_M(r,\lambda)+\sigma_{ABS}(r,\lambda)N_r(r) \quad (2.3.18)$$

where

$\alpha_{SC}(r,\lambda)$ = the atmospheric volume scattering coefficient without absorption,

$\alpha_R(r,\lambda)$, $\alpha_M(r,\lambda)$ = the Rayleigh and Mie volume scattering coefficients respectively,

$\sigma_{ABS}(r,\lambda)$ = the absorption cross section,

$N_r(r)$ = the concentration of the pollutant molecules.

An expression for the concentration of the molecular pollutant N_r, averaged over a distance ΔR can be obtained from Equation 2.3.17 by forming twice the difference of the logarithms of $P_r(R)$ and $P_r(R+\Delta R)$, first for the wavelength λ, (absorption peak), and second for the wavelength λ_2 (absorption trough), as shown below:

$$\ln P_r(R,\lambda_1)-\ln P_r(R+\Delta R,\lambda_1) = (-2\Delta R/R)+\ln[\beta_R(R,\lambda_1)+\beta_M(R,\lambda_1)] - \ln[\beta_R(R+\Delta R,\lambda_1)+\beta_M(R+\Delta R,\lambda_1)] + 2\alpha_{SC}(\lambda_1)\Delta R + 2\sigma_{ABS}(\lambda_1)N_r\Delta R. \quad (2.3.19)$$

$$\ln P_r(R,\lambda_2) - \ln P_r(R + \Delta R,\lambda_2) = (-2\Delta R/R) + \ln[\beta_R(R, + \beta_M(R,\lambda_2)] - \ln[\beta_R(R + \Delta R,\lambda_2) + \beta_M(R+ \Delta R,\lambda_2)] + 2\alpha_{SC}(\lambda_2)\Delta R + 2\sigma_{ABS}(\lambda_2)N_r\Delta R. \quad (2.3.20)$$

Then $\bar{N}_r$, the value of N_r averaged for the depth resolution ΔR at range r can be obtained from Equations 2.3.19 and 2.3.20 as:

$$\bar{N}_r = \frac{1}{2\Delta\sigma\Delta R}\left[\ln \frac{P_r(R,\lambda_1)}{P_r(R + \Delta R,\lambda_1)} - \ln \frac{P_r(R,\lambda_2)}{P_r(R + \Delta R,\lambda_2)} + E + E'\right] \quad (2.3.21)$$

where,

$$E = -2\ \alpha_{SC}(\lambda_1) - \alpha_{SC}(\lambda_2)\ \Delta R, \quad (2.3.22)$$

$\alpha_{SC}(\lambda) = \alpha_R(\lambda) + \alpha_M(\lambda)$, the total volume scattering coefficient neglecting absorption, averaged over ΔR,

$\Delta\sigma = \sigma_{ABS}(\lambda_1) - \sigma_{ABS}(\lambda_2)$, the difference in absorption cross sections for the material of interest, and

$$E' = \ln\left[\frac{\beta_R(R+\Delta R,\lambda_1) + \beta_M(R+\Delta R,\lambda_1)}{\beta(R,\lambda_1) + \beta_M(R,\lambda_1)}\right] - \ln\left[\frac{\beta_R(R+\Delta R,\lambda_2) + \beta_M(R+\Delta R,\lambda_2)}{\beta(R,\lambda_2) + \beta_M(R,\lambda_2)}\right] \quad (2.3.23)$$

For simultaneous two wavelength Lidar operation at two close lying wavelengths the scattering properties of the atmosphere, and therefore the α_{SC}'s and β's are the same for

both wavelengths. Therefore E and E can be approximately taken to be zero[26,28,43] and Equation 2.3.21 reduces to

$$\bar{N}_r = \frac{1}{2\Delta\sigma\Delta R} \ln\left[\frac{\frac{P_r(R,\lambda_1)}{P_r(R,\lambda_2)}}{\frac{P_r(R+\Delta R,\lambda_1)}{P_r(R+\Delta R,\lambda_2)}}\right] \qquad (2.3.24)$$

or,

$$N_r = \frac{\ln(1 + \Delta F_r)}{2\Delta\sigma\Delta R} \qquad (2.3.25)$$

where,

ΔF_r = the fractional change in the ratio of ratios of the received signals.

As can be seen from Equation 2.3.25 the sensitivity of pollutant detection is improved by:

1. The ability of the instrumentation to detect smaller changes in ΔF_r,
2. Increasing the sampling length, Δr (at a cost of decreasing spatial resolution), and
3. A large resonance absorption cross section, σ_{λ_1}, and a small off-resonance cross-section σ_{λ_2}.

2.3.6 Evaluation of required system parameters

2.3.6.1 Transmitted signal requirements

Figure 2.2.6 shows the absorption spectrum of NO_2 as measured in our laboratory. It is seen that at 4478.5 and 4500 Å there is an adjacent peak and trough which are sufficiently close to be an ideal pair for application of the DASE scheme. Their cross sections are

$$\sigma_{ABS}(4478.5\ \text{Å}) = 6.38 \times 10^{-19}\ \text{cm}^2$$
$$\sigma_{ABS}(4500\ \text{Å}) = 3.5 \times 10^{-19}\ \text{cm}^2$$

Now if for simplicity an NO_2 free region is assumed up to the sample region ΔR, then solving Equation 2.3.17 for transmitted power yields:

$$P_o(\lambda) = \frac{P_r(R + \Delta R, \lambda)}{(c\tau_P/2)\left[\beta_R(R + \Delta R, \lambda) + \beta_M(R + \Delta R, \lambda)\right]} \times \frac{1}{\left[KA/(R + \Delta R)^2\right] \exp\left\{-2\left[\alpha_{SC}(\lambda)(R + \Delta R) + \sigma_{ABS}(\lambda)N_r\Delta R\right]\right\}} \qquad (2.3.26)$$

Now, if as in section 2.3.2, it is assumed that a 5% change in the ratio of the received signals is the minimum that can realistically be detected with a $(S/N)_{min}=10$, and the same AVP photomultiplier is used then a received signal of 0.25 μWatts is required at the photomultiplier. Furthermore if the 5% change in received signal ratios, is

to be used to detect (as in typical urban environment) a pollution concentration (or a change in pollution concentration) of 0.03 ppm of NO_2 over a sample length of 100 meters, at 10,000 meter range, and a visibility of 10 Km we can calculate the required transmitted power from the following considerations. The backscatter coefficient for Rayleigh backscatter is theoretically given by

$$\beta_R = (3/16\pi)\alpha_R \qquad (2.3.27)$$

and for Mie backscatter is effectively found in the 5000 Å region to be given by

$$\beta_M = 0.08\ \alpha_M \qquad (2.3.28)$$

As discussed in section 2.2.6, Table 2.2.3 gives the extinction coefficients for Rayleigh scattering by atmospheric molecules, and for Mie scattering at different visibilities, both as a function of the wavelength of the light being scattered. At the wavelengths of interest, 5000 Å it is seen that, at for instance 10 Km visibility

$$\alpha_M = 0.441$$

and

$$\alpha_R = 0.018$$

Therefore at 10 Km visibility

$$\beta_R = 0.00107 \text{ and } \beta_M = 0.03528$$

and

$$\beta_M = 20.75\beta_R \qquad (2.3.29)$$

The total backscatter coefficient β is the summation of β_M and β_R:

$$\beta = \beta_M + \beta_R = 0.037$$

Substituting in Equation 2.3.17 gives a required transmitted power of 2 MW. For the typical effective pulse length of 0.25 μsec for the flashlamp-pumped dye laser this is equivalent to an energy of 1/2 J.

2.3.6.2 Pump Depletion

In the previous discussion the Rayleigh and Mie backscatter returns were considered assuming an NO_2-pollutant free atmosphere up to the sampled region.

Consider now that the region of the atmosphere up to the sampled region contains a pollutant of same concentration. Then the transmitted energy requirements would have to increase in order to maintain the minimum detectable concentration level over the sampled region. For an NO_2-polluted free atmosphere up to the sampled region assuming an average pollution concentration of 0.315 ppm of NO_2 over 100 m, a range 1000 m, visibility 10 km and the minimum received power 0.25 μW (giving fractional change of ratio of ratios of received power 5%), yields on and off-line transmitted powers 0.0395 MW(9.88 MJ) and 0.0375MW (9.38MJ) respectively. Consider now the above density 0.315 ppm over the entire range 1000 m. Since 100 m cause approximately a 10% reduction in received signal power, as

previously discussed, 1000 m will cause a reduction by a factor exp(-1.08)=0.34. Therefore the received signal will be down by 34% of its original value of 5.41 μW and 5.37 μW off and on-line respectively and it would be possible to detect a minimum concentration of 0.51 ppm (0.45% change in the ratio of ratios). Thus a laser pulse energy of 1/2 J for each line can be used for detection of a change in NO_2 concentration of 0.051 ppm over 100 m, at a range 1000 m even when pollution concentration as high as 0.315 ppm exist along the entire probe beam path.

2.4 Requirement for Simultaneous Output

A special requirement of the DASE system, if it is to achieve its potential for accuracy, is the use of simultaneous outputs at the two transmitted wavelengths one on, and one off, the absorption peak of the monitored pollutant molecule. It is the use of simultaneous two wavelength outputs that makes this approach optimum as far as obtaining accurate real-time range-resolved Lidar pollution measurements. The requirement for simultaneous outputs arises from the rapidity with which the Lidar optical path changes, due to thermal effects and particle drift in the atmosphere. Turbulant mixing of atmospheric air masses causes the rapid variation of the temperature from point to point in the atmosphere, with consequent variation of the index of refraction. The interaction of a laser beam with a temperature inhomogeneous atmosphere, leads to random

variation in the beam amplitude and phase. Physically those fluctuations are caused by either wavefront distortion over a lateral beam distance or a plane wavefront being tilted. The first cause leads to beam spreading, and beam scintillation, while the second contributes to beam steering and image dancing. Furthermore temperature variations in the atmosphere can cause variations of the polarization angle along the beam.

The factors affecting the propagation of the Lidar beam which vary rapidly with time, are briefly discussed below.

1. Beam spreading This occurs when the beam wavefront (Figure 2.3.5) is distorted over some lateral beam distance. Corresponding to each phase coherent portion of the beam, there is a ray deviation angle which is relatively independent from one coherent area of the beam to another. Hence the beam energy is randomly spead in the receiver plane. It is physically due to small angle scattering, that increases the beam divergence and decreases the spatial power density at the receiver.[39]

2. Beam scintillation Small scale destructive interference within the beam cross-section, causes variations in the spatial power density at the receiver. Figure 2.3.6 shows the destructive and constructive regions of self-interference of the beam which are characterized by the light and dark patches in a photograph.[40] Under most conditions the power spectrum of intensity fluctuations for one-way propagation is quite small above 10,000 Hz and the

atmosphere can be considered frozen insofar as scintillation is concerned for time intervals smaller than 1 msec.[41]

3. Beam steering Angular deviation of the beam from the line-of sight path may cause the beam to miss the receiver. Beam steering is shown in Figure 2.3.7. The average angular deviation for a single ray, assuming that the plane waveform is tilted at an angle is proportional to this angle .[39] Compensation for beam steering may be effected simply by increasing the beam divergence angle so that, even if the beam is deviated by turbulence, the receiver will still be illuminated. The penalty paid, of course, is a reduction in spatial power density in the receiver plane.

4. Image Dancing Variations in the beam-arrival angle, can cause a displacement of the focus point from the focal point on the image plane of the receiver.[39] In most cases the deviation in beam arrival angle is small and image dancing is negligible. Compensation for image dancing, if it is of concern, may be effected by providing a larger detector area which increases the receiver field of view. Increasing the field of view, however, results in a greater amount of background radiation entering the receiver.

5. Polarization Fluctuations The changing index of refraction along a linearly polarized laser beam atmospheric path, results in fluctuations of the polarization angle of the received signal. As will be seen in the detailed discussion in Chapter 3, the change in polarization angle, or the depolarization due to atmospheric turbulance, is very

small (of the order of 10^{-8} radians). The experiments carried out verify that polarization fluctuations are not a problem for laser beam propagation in so far as the Lidar scheme is concerned.

6. Particulate drift As different particulate concentrations drift accross the scene being viewed by the Lidar, these can be expected to cause different backscatter and absorptions along the outgoing and returning Lidar signals.

Several of these factors, beam spreading, scintillation, steering and image dancing, would be expected to cause considerable problems, in the DASE Lidar scheme, if the measurements at the two wavelengths were made sequentially at intervals comparable to those in which changes occur in these factors (10^{-4} seconds).

However, the use of simultaneous measurments at close lying wavelengths avoid such problems, since the transmitted and received beams are both affected in exaclty the same manner.

2.5 Polarization Discrimination Approach for DASE Lidar

As is seen from the above discussions on the DASE Lidar scheme, a central element in it, is the use of two close-lying frequencies simultaneously, which avoids effects of temporal changes in the optical path, or in the scene being probed. For the DASE scheme to operate, it is clearly necessary to be able to distinguish between the returns at the two close-lying wavelengths. In the past, this has been

done through the use of narrow band filters. For example, filters with bandwidths of approximately 5 Å are used for monitoring NO_2 with Lidar beams at 4478.5 and 5000 Å. This approach of using narrow band filters, suffers from several limitations.

- Narrow band filters made on a glass substrate with several dielectric coatings are obviously made for a specific frequency, and are not tunable, whereas the dye lasers normally used with the DASE Lidar scheme are. The use of fixed frequency filters therefore limits the inherent versatility which the system would otherwise have by virtue of the tunability of the dye laser.

- Narrow band filters are not readily available at near UV wavelengths where close-lying wavelength discrimination is required for the monitoring of some trace constituents such as Ozone and Sulfure dioxide. Filters which can be produced for these wavelengths through the use of Fabry Perot resonators are very expensive and require careful alignement. Thus unless such filters are used, the DASE Lidar scheme can only be used in sequential operation.

- Narrow band filters suffer considerable losses, typically 70% of the signal for a 5 Å bandwidth filter in the 5000 Å spectral region.

To overcome some of the limitations discussed above, a scheme which makes use of polarization discrimination was developed in this thesis for use with DASE Lidar scheme. It's basic format is shown schematically in Figure 2.4.1.

Through the use of an intracavity polarizing beam splitter, Figure 2.4.1b, the transmitted laser beams at the two close lying wavelengths (at an absorption peak and trough respectively) are orthogonally polarized with respect to each other.

Then, on the basis that the scattered Lidar returns will likewise largely ratain the outgoing poparizations, the return signals, Figure 2.4.1a, at each of the two wavelengths are separated again by using a polarizing beam splitter and detected separately, by separate photomultipliers. A single, relatively large bandwidth filter 50-100 Å is sufficient to reduce even daylight background noise to acceptable levels. Its transmission losses are typically less than that of a narrow band filter by a fraction of 2-3 thereby enhansing signal to noise ratio in the (dark current limited) DASE scheme.

For the approach outlined above to be valid, depolarization backscatter due to Rayleigh and Mie scattering must represent a negligible factor in the return signals, in comparison to effects of the molecular pollution attenuation being measured. These factors, as well as others which may cause errors or limitations in the application of a polarization discrimination scheme are examined in the next chapter. It should be noted that the scheme permits the use of one wide band filter instead of two narrow band ones. Such wide band filters are readily available at visible and near UV wavelengths, permitting the ready extention of the

very important simultaneous operation aspect of the DASE Lidar to the monitoring of Ozone and SO_2 in the near UV, as well as permitting desirable tunability when it is required.

The development of a successful polarization discrimination scheme is expected to have implications for other lidar techniques, including Raman and fluorescence backscatter measurements. For instance, to improve the sensitivity for the measurement of fluorescence backscatter, the polarization discrimination scheme permits the use, in front of the photomultiplier detectors, of a wide bandwidth filter in conjuction with a polarizer set to pass through only the backscatter that is orthogonally polarized to the transmitted beam and hence, block the backscatter at the transmitted frequency. This approach would permit more of the fluorescence backscatter to be available for detection and hence increases the sensitivity of the system. Other potential applications of a successful polarization discrimination system are related to the Lidar detection of clear air turbulance.

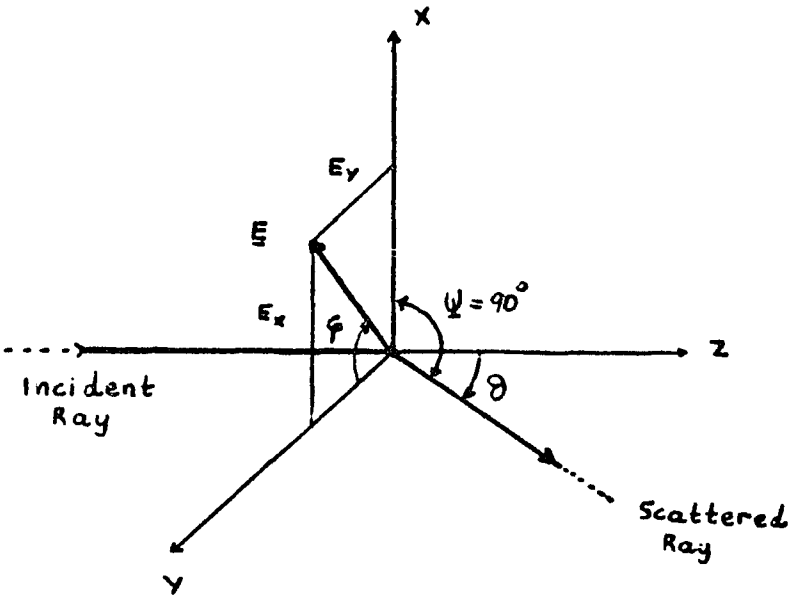

FIGURE 2.2.1 Geometrical view for Rayleigh Scattering.

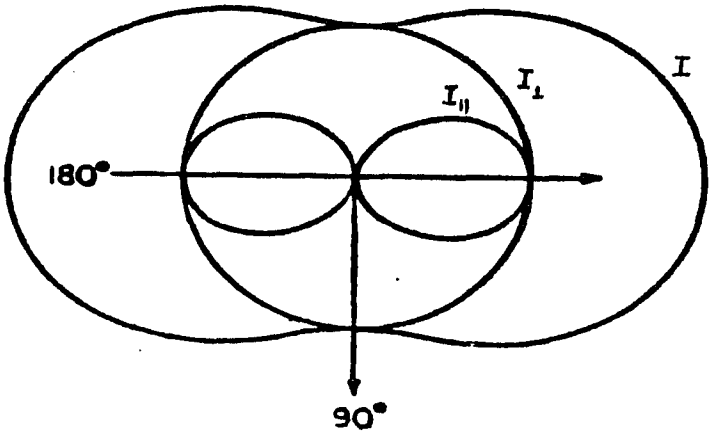

FIGURE 2.2.2 Radiation polar diagram for Rayleigh scattering

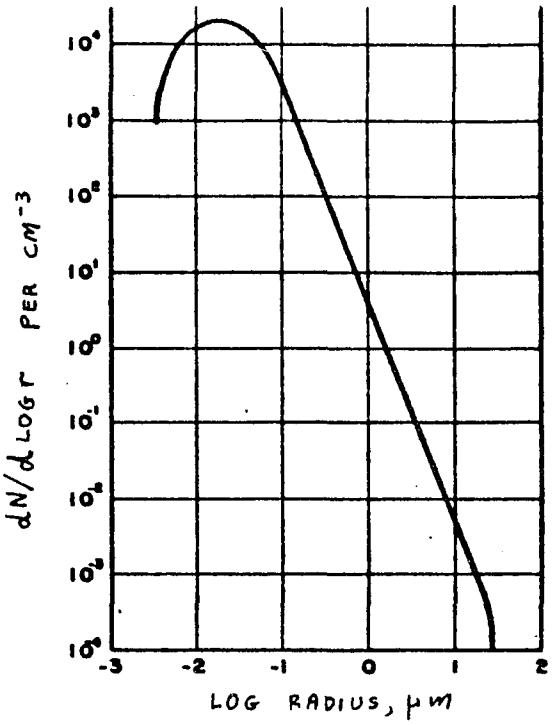

FIGURE 2.2.3 Junge particle size distibution for continental air.

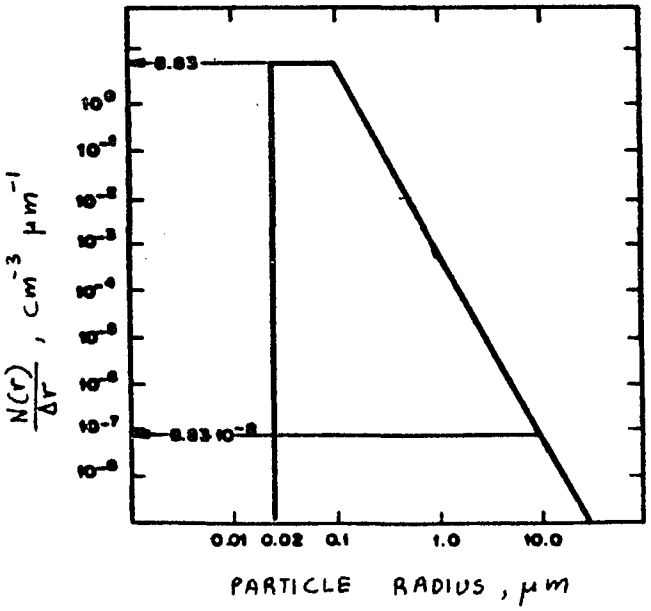

FIGURE 2.2.3 Normalized particle size distribution for aerosol models.

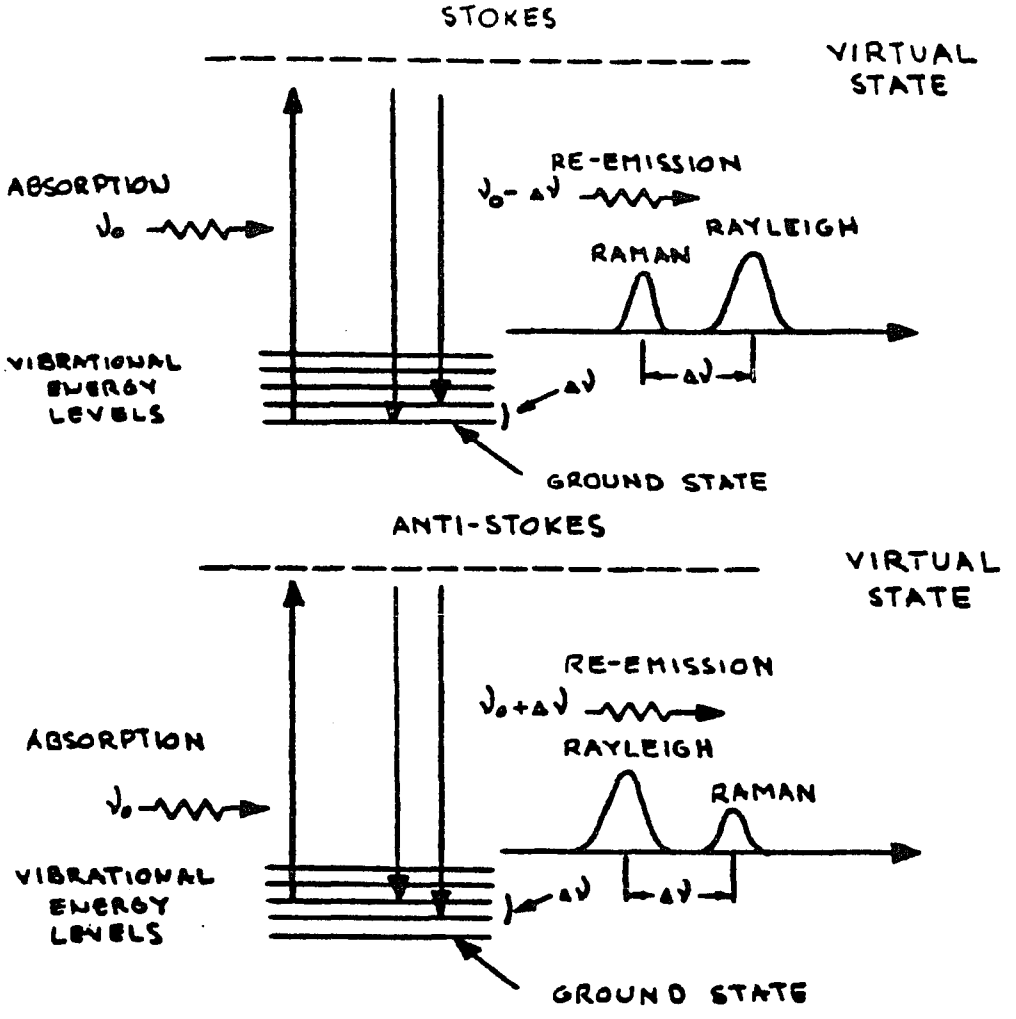

FIGURE 2.2.5 The Raman Process

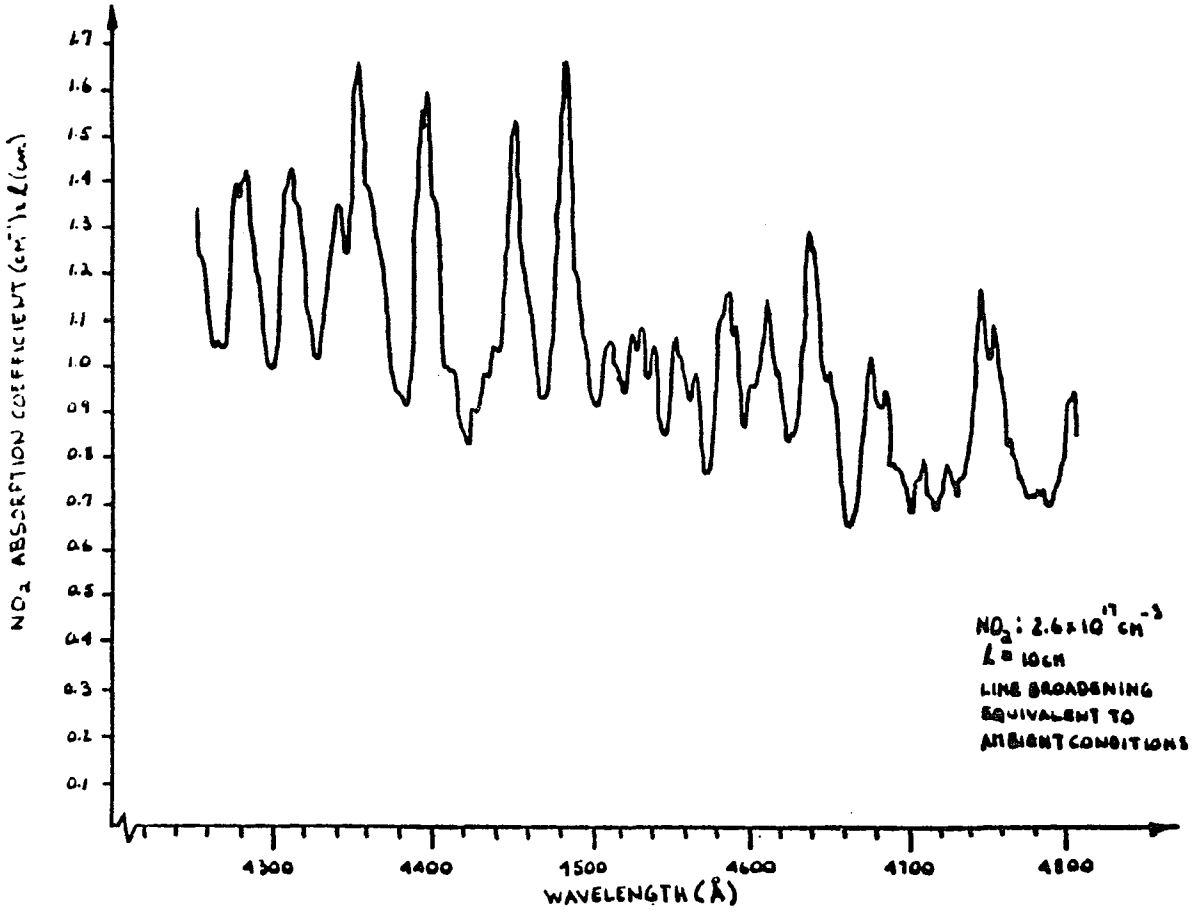

FIGURE 2.2.6 NO_2 Absorption spectrum.

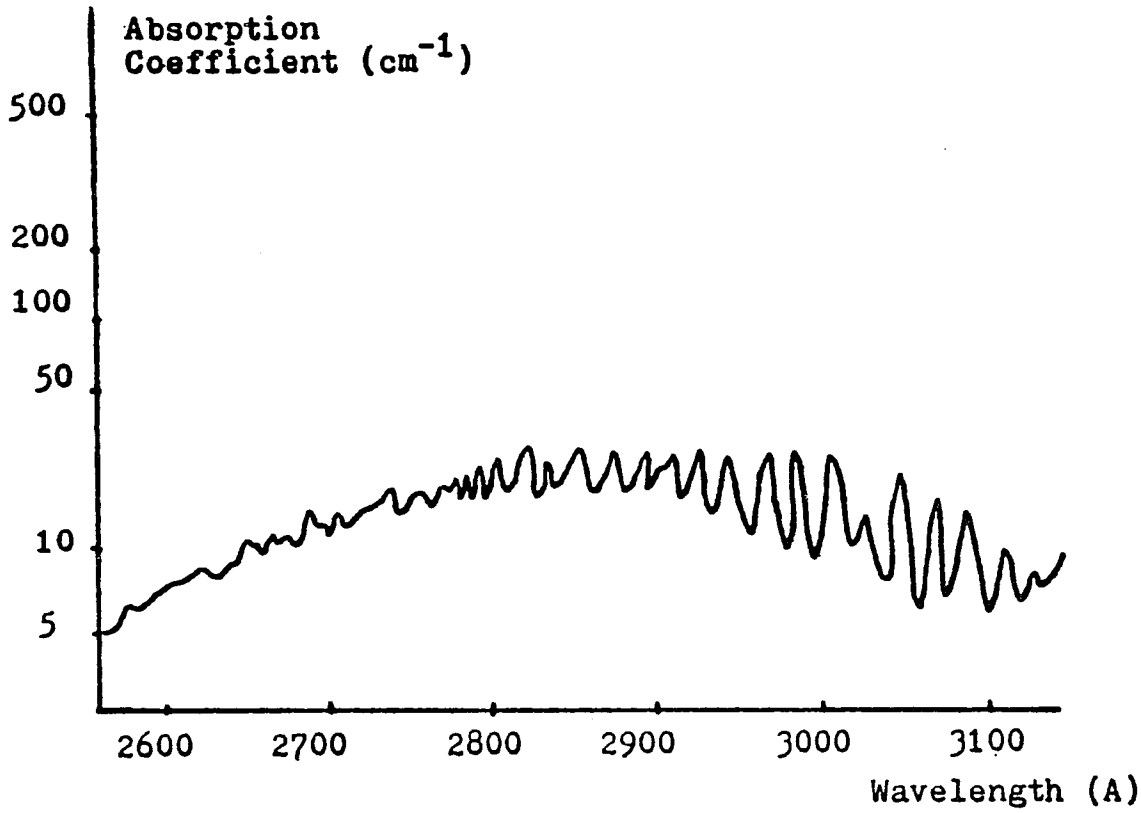

FIGURE 2.2.7 SO_2 Absorption spectrum.

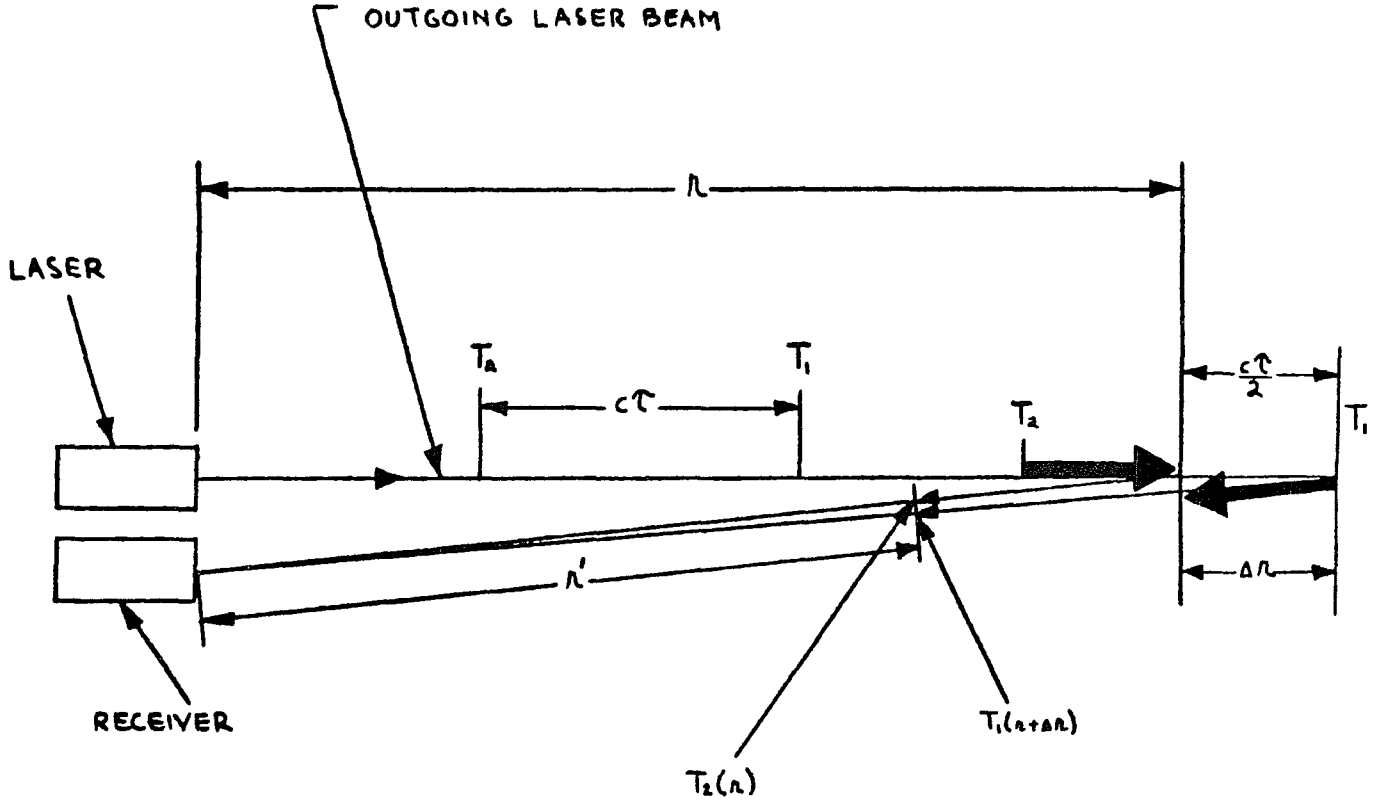

FIGURE 2.3.1 Lidar backscatter and obtainable depth resolution.

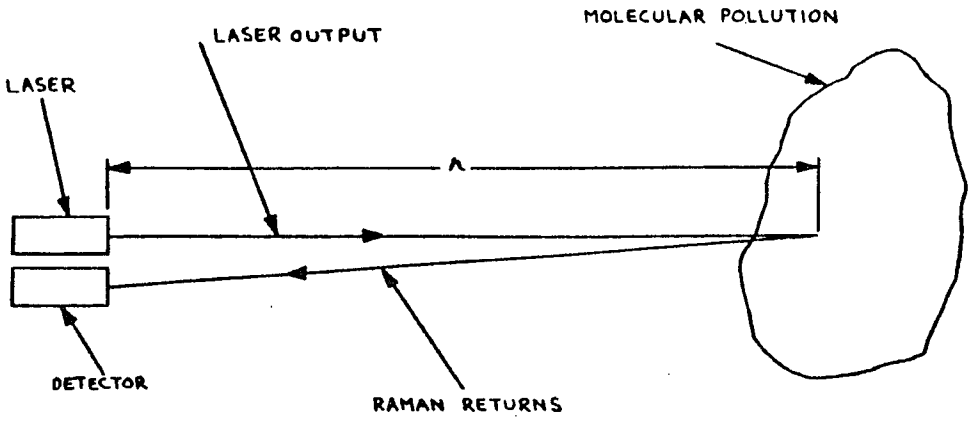

FIGURE 2.3.2 The Raman scheme.

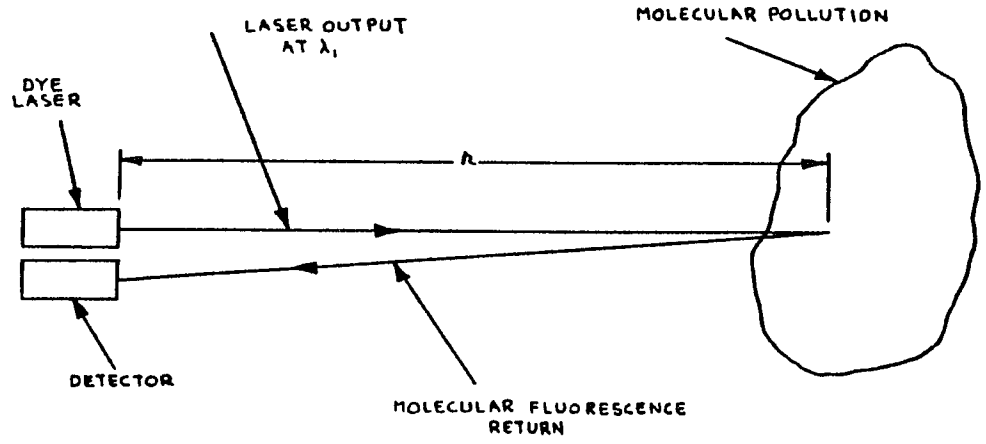

FIGURE 2.3.3 The Fluorescence scheme.

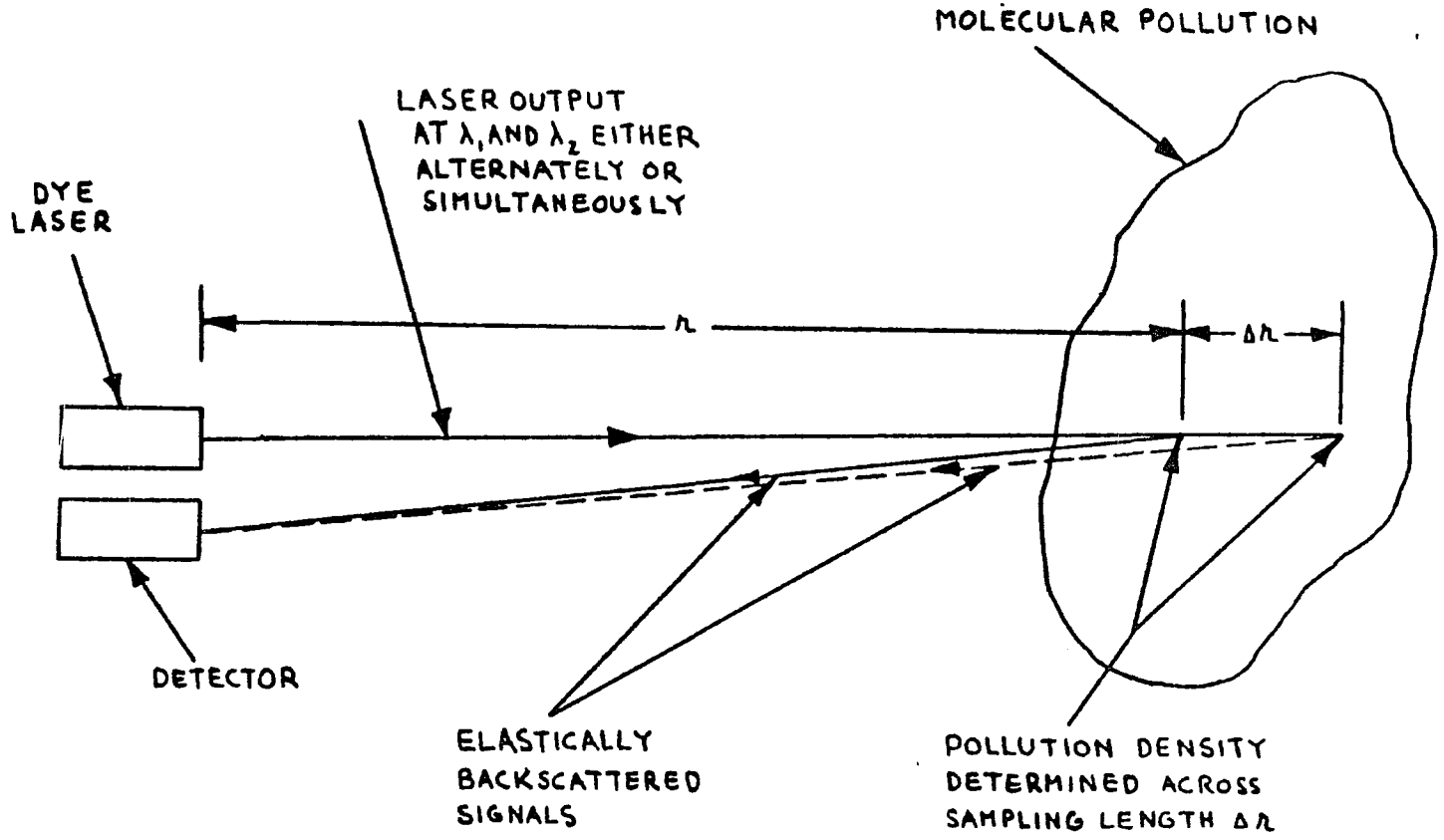

FIGURE 2.3.4 The DASE Scheme.

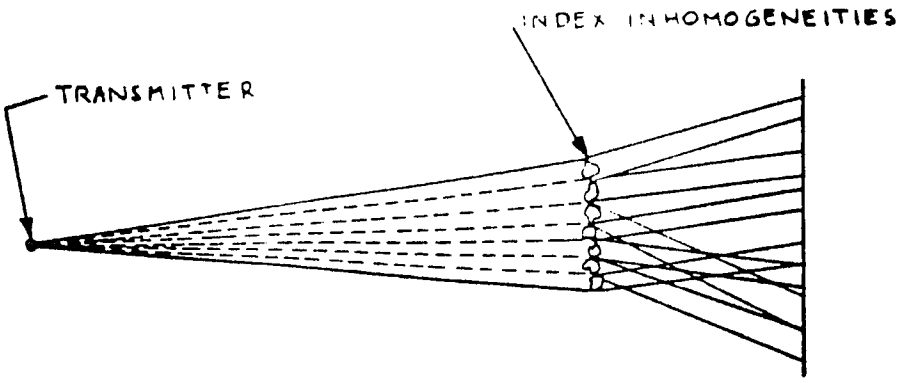

FIGURE 2.3.5 Beam Spreading.

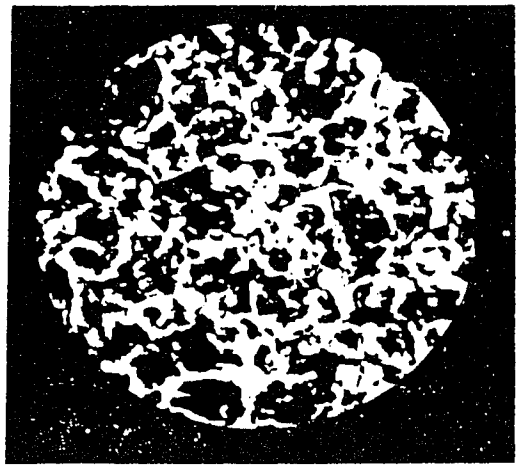

FIGURE 2.3.6 Beam Scintillation.

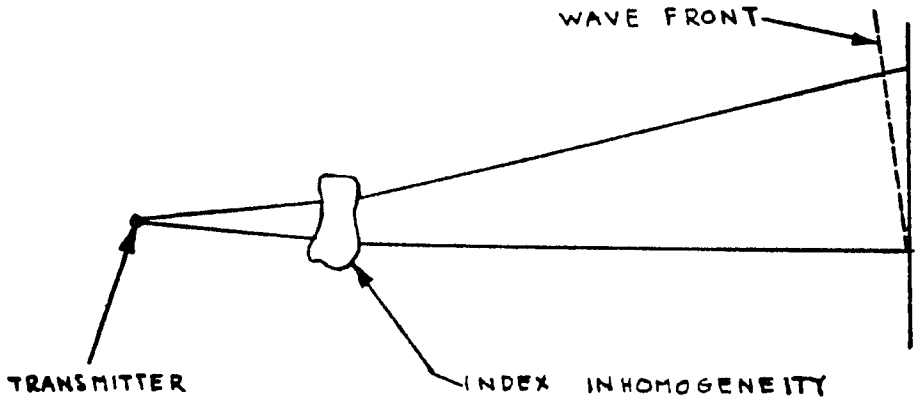

FIGURE 2.3.7 Beam Steering.

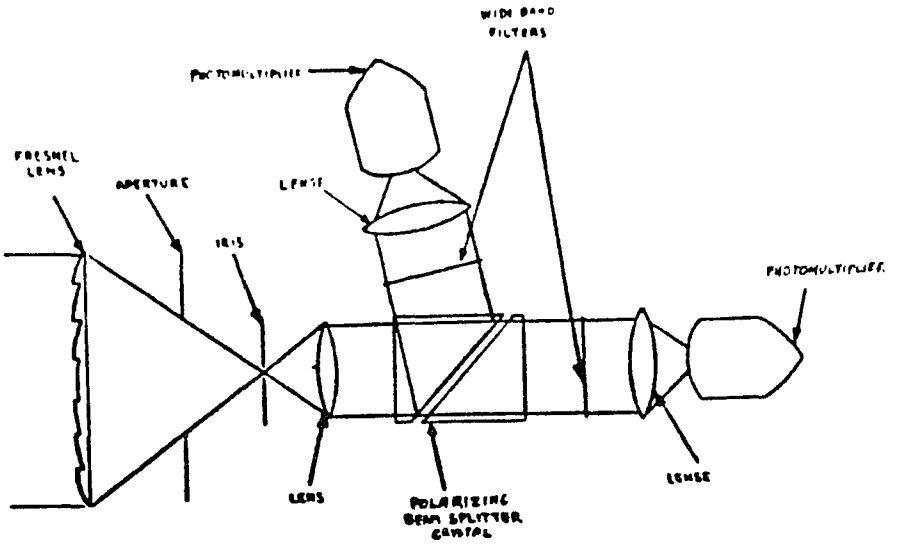

FIGURE 2.4.1a Optical receiver for simultaneous cross-polarized operation.

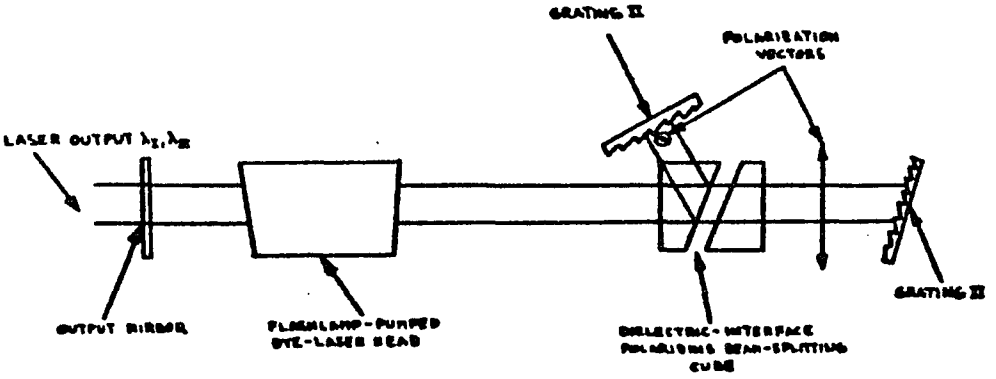

FIGURE 2.4.1b Lidar transmitter for simultaneous cross-polarized operation.

Altitude Km	Particle density N, particles/cm 23 Km Visibility Clear	5 Km Visibility Hazy
0	2,828	13,780
1	1,244	5,030
2	537.1	1,844
3	225.6	1,844
4	119.2	245'3
5	89.87	
10	56.75	
20	26.67	

Table 2.2.1 Aerosol models - Vertical distribution

Wavelength Dam	Refractive index Water-Soluble	Dustlike
0.3371	1.53-j0.005	1.53-j0.008
0.5145	1.53-j0.005	1.53-j0.008
0.6328	1.53-j0.006	1.53-j0.008
0.6943	1.53-j0.007	1.53-j0.008
0.8600	1.52-j0.0012	1.52-j0.008

TABLE 2.2.2 Aerosol complex index of refraction n-jn

λ (microm)	α_R (Km^{-1})	$\alpha_M(Km^{-1})$ V=1 Km	V=5 Km	V=10 Km
0.2	0.708	7.0	2.2	1.4
0.3	0.14	5.6	1.4	0.84
0.4	0.44	4.7	1.1	0.58
0.45	0.027	4.4	1.01	0.496
0.5	0.018	4.134	0.86	0.441
0.6	0.0083	3.7	0.72	0.35
0.8	0.0026	3.1	0.54	0.24

TABLE 2.2.3 Rayleigh and Mie Scattering Coefficients

Process	Differential Cross Section (cm^2)
Elastic Scattering	
Rayleigh Scattering	10^{-27}
Mie Scattering	10^{-21} to 10^{-24}
Inelastic Scattering	
Raman	10^{-30}
Resonance Raman	10^{-26}
Fluorescence (lifetime 10^{-6} to 10^{-8})	10^{-14} to 10^{-17}
Absorption	10^{-14} to 10^{-17}

TABLE 2.2.4 Typical Cross Section values for Scattering Processes.

Method	Effective Reflectivity	Magnitude
Long Path Absorption with Retroreflector	ρ/π	10^4 to 10^6
Long Path Absorption From Topographical Target	ρ/π	$1/\pi$
Differential Absorption of Scattered Energy	$(c\tau/2)(\beta_M/4\pi)$	10^{-4}
Resonance Fluorescence and Fluorescence	$(c\tau/2)(N\sigma_F/4\pi)$	10^{-5} (1 ppm) U.V. and Vis.
Raman	$(c\tau/2)(N\sigma_{RAM}/4\pi)$	10^{-15} (1 ppm) 10^{-9} (1 Atm)

TABLE 2.3.1 Effective Reflectivity for different scattering processes

CHAPTER 3

BASIC PARAMETERS OF POLARIZATION
ATMOSPHERIC DEPOLARIZATION AND ERROR ANALYSIS

3.1 Introduction

There are many reasons why problems of polarization and depolarization deserve intimate study. In many cases observation of changes in polarization permits deeper insight into physical phenomena. In addition, the solutions of polarization and depolarization problems have a host of practical applications, some of which come under one of the following three groups:

Optimization. In many cases, a certain type of polarization will accomplish a given task better than another.

Discrimination. Unwanted reflections and other causes, often lead to the presence of two signals of which only one is wanted and the other interferes, yet separation by frequency, amplitude or phase proves difficult or impossible. Often the two signals, differ, or can be made to differ in polarization, and this can be used to discriminate against one of them.

Identification. Since different types of scatterers and propagation media will produce different types and degrees of depolarization, it is often possible to infer what type of scatterers, what type of medium, what type of geometrical

configuration of scatterers, etc., must have been responsible for an observed type of depolarization.

Since the lidar system in the work reported utilizes polarization discrimination, some study of polarization and depolarization is necessary. In this chapter the various parameters related to polarization and depolarization that may have an impact on the polarization discrimination Lidar scheme are discussed and an error analysis is given, to show the expected effect of their variation on the accuracy of lidar measurements.

3.2 Properties of polarized light

3.2.1 Basic definitions- Linear Polarization

An electromagnetic wave propagating in the direction of the unit vector k has four basic characteristics: amplitude, phase, frequency and polarization.

The term **Polarization** is used to describe the statistical fluctuations of the direction of the electric vector E of the electromagnetic wave. Figure 3.2.1 shows the orientation of the electric vector E at an instant of time for an electromagnetic wave. The plane defined by E and the propagation vector k at a point is called the **polarization plane.** The orientation of the electric field E, with respect to a reference plane, at a given point in space, during one period of oscillation is called the **direction of polarization.** The angle between the polarization plane and the reference plane at a point is called the **polarization**

angle. As a reference plane is usually taken the Horizontal plane if the surface of the earth is relevant or the plane of incidence (determined by the incident and reflected or scattered beam axes) in scattering problems.

An electromagnetic wave is linearly polarized if the polarization plane has constant orientation (constant polarization angle) at any point. Figure 3.2.2 shows a linearly polarized electromagnetic wave. The components of the electric vector E are expressed using two mutually perpendicular unit vectors in the plane perpendicular to k. These two unit vectors are oriented in privileged directions i.e. parallel and perpendicular to the reference plane. Depending on the application the parallel and perpendicular components of the electric vector E have different notations i.e. E^- and E^+, E_p and E_c, $E_{\parallel}$ and $E_{\perp}$, E_h and E_v , E_x and E_y respectively. Figure 3.2.1 shows the orientation of the electric vector E at an instant of time for an electromagnetic wave. Considering the horizontal plane as the reference plane, a linearly polarized wave with polarization plane parallel or perpendicular to the horizontal plane is called **horizontally** or **vertically polarized** respectively.

3.2.2 Elliptic Polarization

For an electromagnetic wave propagated along the z-axis, with the E and H vectors vibrating harmonically in the xy plane, the two Cartesian components are given by

$$E_x = E_{xo}\exp\{j(\tau + \Delta_x)\}$$
$$E_y = E_{yo}\exp\{j(\tau + \Delta_y)\} \qquad (3.2.1)$$

where $\tau = (wt-kz)$

Considering the real parts for E_x, E_y and eliminating τ, the locus of E can be determined from the resulting equation

$$\left(\frac{E_x}{E_{xo}}\right)^2 + \left(\frac{E_y}{E_{yo}}\right)^2 - 2\left(\frac{E_xE_y}{E_{xo}E_{yo}}\right)\cos\Delta = \sin\Delta \qquad (3.2.2)$$

where $\Delta = \Delta_x-\Delta_y$

which is the equation of an ellipse and is depicted in Figure 3.2.3. The value of Δ determines the form of the elliptical vibration as shown in Figure 3.2.4. This ellipse represents a projection on the xy plane of the locus of the magnitude of the extreme values of the electric vector (the amplitude), and for this general case the wave is said to be elliptically polarized.

The sides of the rectangle in which the ellipse is inscribed are parallel to the coordinate axes and have lengths $2E_{xo}$ and $2E_{yo}$. The ellipse touches the sides at the points $(\pm E_{xo}, \pm E_{yo}\cos\Delta)$ and $(\pm E_{xo}\cos\Delta, \pm E_{yo})$. The major axis of the ellipse is inclined at an angle Ψ with respect to the x-axis given by

$$\tan 2\Psi = \left(\frac{2E_{xo}E_{yo}}{E_{xo}^2 - E_{yo}^2}\right)\cos\Delta \ , \qquad 0 \leq \Psi \leq \pi \qquad (3.2.3)$$

The major and minor axes of the ellipse, A and B respectively, are given by

$$A^2 = E_{xo}^2\cos^2 + E_{yo}^2\sin^2 + 2E_{xo}E_{yo}\cos \sin \cos\Delta \qquad (3.2.4)$$

$$B^2 = E_{xo}^2\cos^2 + E_{yo}^2\sin^2 - 2E_{xo}E_{yo}\cos \sin \cos\Delta$$

Defining

$$\frac{E_{yo}}{E_{xo}} = \tan\alpha \ , \qquad (0 \leq \alpha \leq \pi/2) \qquad (3.2.5)$$

and

$$\pm \frac{B}{A} = \tan\gamma \ , \qquad (-\pi/4 \leq \gamma \leq \pi/4) \qquad (3.2.6)$$

where the ratio B/A is called the ellipticity, the following usefull relationships are valid

$$\tan 2\Psi = (\tan 2\alpha)\cos\Delta \qquad (3.2.7)$$

$$\sin 2\gamma = (\sin 2\alpha)\sin\Delta \qquad (3.2.8)$$

$$\cos 2\alpha = \pm(\cos 2\gamma)\cos 2\Psi \qquad (3.2.9)$$

In addition conservation of light intensity (Energy) gives

$$E_{xo}^2 + E_{yo}^2 = A^2 + B^2 \qquad (3.2.10)$$

Also if Z_0 is the intrinsic impedence for plane waves the intensity is given by

$$I = \frac{(A^2 + B^2)}{2Z_o} \qquad (3.2.11)$$

3.2.3 Polarization and depolarization factors

For a plane electromagnetic wave with propagation vector k the electric field E as vector-phasor can be resolved in two components Horizontal and Vertical

$$E = E_x e_x + E_y e_y \qquad (3.2.12)$$

where e_x and e_y are the corresponding unit vectors. Considering E_x and E_y as complex phasors, for monochromatic wave with frequency ω, the complex polarization factor is defined as

$$p = \frac{E_y}{E_x} \qquad (3.2.13)$$

The polarization factor is in general a complex quantity.

$$p = |p| \exp\{j\arg(p)\} = (E_y/E_x)\exp\{j\arg(E_y) - j\arg(E_x)\}$$
$$= (E_{yo}/E_{xo})\exp\{j\Delta\} \qquad (3.2.14)$$

where

$$|p| = \frac{E_{yo}}{E_{xo}} \qquad (3.2.15a)$$

and

$$\arg(p) = \Delta \qquad (3.2.15b)$$

are the ratio of the amplitudes and the phase difference respectively between the two components of the wave.

Since any elliptic polarization can be produced by superposition of two mutually perpendicular polarizations, with the corresponding amplitude and phase shift, it follows that the complex polarization factor describes the polarization of an electromagnetic wave uniquely. It is shown in Equations 3.2.15 that all the parameters of the polarization ellipse, involved in Equations 3.2.1 through 3.2.11, can be obtained from p .

Another important quantity for polarization studies is the degree of polarization defined as

$$P = \frac{I_p}{I_p + I_u} \qquad (3.2.16)$$

where I_p is the intensity of the polarized component and I_u is the intensity of the unpolarized component.

A change in polarization suffered by an electromagnetic wave as consequence of propagation, reflection, scattering, diffraction or any other interaction with matter, is called depolarization. For an incident linearly polarized field E_1 subjected to electromagnetic process causing depolarization, the resulting field E_2 can be expressed as

$$E_2 = E_{2p} + E_{2c} \qquad (3.2.17)$$

where E_{2p} is the component parallel to the incident field E_1 and E_{2c} is the cross-polarized component, perpendicular to the incident field E_1. If I_2 and P_2 are the intensity and power respectively corresponding to E_2, the linear depolarization ratio δ is defined as

$$\delta = \frac{E_c}{E_p}^2 = \frac{P_c}{P_p} = \frac{I_c}{I_p} \qquad (3.2.18)$$

In case of depolarization due to backscattering, using β_c and β_p, the backscattering coefficients of the two components of E_2, δ can be expressed as

$$\delta \quad \frac{\beta_c}{\beta_p} \qquad (3.2.19)$$

Depending on the interaction, E_c may be completely unpolarized or polarized with phase difference with respect to E_p, resulting in elliptically polarised field E_2. In the second case the depolarization ratio can be expressed in terms of the parameters of the polarization ellipse. In general, after an interaction, the orientation of the major semiaxis of the polarization ellipse with respect to the reference plane is different from the orientation of the incident field E_1. If the orientation difference is an angle

Ψ, the depolarization ratio δ can be expressed as

$$\delta = \frac{B^2 + A^2\tan^2\Psi}{B^2\tan^2\Psi + A^2} \qquad (3.2.20)$$

3.3 Depolarization Mechanisms Affecting the Lidar Return Signal

3.3.1 Introduction

In the following sections the different physical mechanisms that can cause depolarization in elastic scattering and in particular in 180^o backscatter will be examined. The mechanisms considered include

- Clear air turbulance
- Rayleigh Scattering
- Particulate Scattering from symmetric and non-symmetric particles
- Scattering from large particles

The combined effects of these scattering mechanisms will then be examined in the context of potential impact on the lidar return signal backscattered into the receiver in conjunction with the DASE polarization discrimination approach.

3.3.2 Depolarization due to clear air turbulence

The effects of thermal air turbulence on a laser beam propagating through the earth's atmosphere were briefly discussed in Section 2.3.4. In this section emphasis is

given in polarization fluctuations due to clear (molecular) air turbulence, and the amount of possible expected depolarization is estimated.

Thermal turbulences affect primarily the refractive index of the medium. The refractive index change, Δn and temperature change, ΔT are related under isobaric conditions by[44]

$$\Delta n = \frac{(1-n)}{T}\Delta T \qquad (3.3.1)$$

Taking the refractive index of air as $n=1.0003$ and $T=300\,^{\circ}K$, the magnitude of the change in n is approximately

$\Delta n \quad 10^{-6}$ per $^{\circ}K$

The electric field entering a region of turbulence can be analyzed into two components, one parallel to the plane of incidence and one perpendicular to the plane of incidence. Considering the xz plane as the plane of incidence, Figure 3.2.1, the polarization angle of the incident field will be given by

$$\varphi = \tan^{-1}(E_{y1}/E_{x1}) \qquad (3.3.2)$$

After leaving the turbulence region, the electric field components are changed to E_{x2} and E_{y2} due to a change of the index of refraction of the medium. The polarization angle is then given by

$$\varphi + \Delta\varphi = \tan^{-1}(E_{y2}/E_{x2}) \qquad (3.3.3)$$

where Δ is the change in polarization angle.

An expression for the mean square change in the polarization angle for an isotropic atmosphere is given by[45]

$$\sqrt{\overline{\Delta\varphi^2}} = 2\pi \sqrt{\overline{\Delta n^2}}\,(L/L_o) \qquad (3.3.4)$$

Where

Δn^2 = the mean square change in index of refraction due to thermal variations

L = the atmospheric path length

L_o = the turbulence dimension.

The mean square change in the refractive index, $\overline{\Delta n^2}$, has been empirically determined to be related to the altitude of observation, H_o, in meters by the relation

$$\overline{\Delta n^2} = 10^{-12} \exp\{-H_o/160\} \qquad (3.3.5)$$

Considering now transmission over a horizontal, low altitude ($H_o \simeq 0$) turbulent path of 1 Km, with a turbulence dimension of $L_o = 1$ meter, the rms change in polarization angle is found to be

$$\sqrt{\overline{\Delta\varphi^2}} = 10^{-9} \text{ rad/Km}$$

It is interesting to note that other expressions for the

mean square polarization angle fluctuation have been abtained[46] showing a λ^2 dependance, and less than 10^{-10} rad/Km polarization angle rms change for optical wavelengths.

Therefore, for clear air over 1 Km path, the cross polarized component produced is -180 dB or a factor of 10^{-9} of the power of the original polarization. As will be seen from the error analysis given later in this Chapter, these values of depolarization effects, due to clear air turbulence, are negligible as far as practical Lidar considerations are concerned.

3.3.3 Depolarization due to Rayleigh scattering by Atmospheric Molecules

In the previous Chapter (section 2.2.2), the basic expressions from Rayleigh theory were presented, for the scattering of linearly polarized light by isotropic non-conductive particles, with size small compared to the incident radiation. Furthermore, from the discussion, it was clear that while Rayleigh theory predicts no depolarization of the incident polarized light after scattering from isotropic particles (Equations 2.2.1 to 2.2.3) a depolarization should be actually expected due to actual anisotropy of the Rayleigh molecular scatterers. The purpose of the following discussion is to estimate the amount of depolarization due to Rayleigh scattering by atmospheric molecules, by determining the linear depolarization ratio δ

equal to (I_c/I_p), where I_p is the intensity corresponding to the scattered field component which is parallel to the incident field, and I_c the intensity corresponding to the perpendicular to the incident field component.

The scattering process is better formulated by using Stoke's parameters to express the polarization properties of each wave, i.e. incident and scattered wave, and a scattering matrix corresponding to the scattering geometry and the properties of scatterers. Considering as reference plane the plane that includes the directions of the incident and the scattered light, the four Stoke s parameters $I_{\parallel}$, $I_{\perp}$, U, V for incident laser light polarized perpendicular to that plane are 0, $I_{\perp_0}$, 0, 0. The Stoke's parameters $I_{\parallel}$, $I_{\perp}$, U, V correponding to the scattered light by a single particle related to those corresponding to the incident light by

$$\begin{bmatrix} I_{\parallel} \\ I_{\perp} \\ U \\ V \end{bmatrix} = \underset{\sim}{A} \begin{bmatrix} 0 \\ I_{\perp_0} \\ 0 \\ 0 \end{bmatrix} \qquad (3.3.6)$$

where $\underset{\sim}{A}$ is the transformation matrix for the scattered light by a single particle, which is a function of the polarizability tensor a_{ij}, which in turn depends on the particle's symmetry, and on the scattering angle ϑ.

For random orientation of many non-absorbing particles,

having the same polarizability tensor and sizes much smaller than the laser wavelength λ, the matrix $\underset{\sim}{A}$ is given by[37]

$$\underset{\sim}{A}=C_{\lambda}\begin{bmatrix} 2A+3B\cos^2\vartheta+A-B & A-B & 0 & 0 \\ A-B & 3A+2B & 0 & 0 \\ 0 & 0 & (2A+3B)\cos\vartheta & 0 \\ 0 & 0 & 0 & 5B\cos\vartheta \end{bmatrix} \quad (3.3.7)$$

where

$$A = 1/15 \sum_{i=1}^{3} a_{ii}^{2}$$

$$B = 1/30 \sum_{i} (a_{ii} \quad a_{jj}) \qquad i,j=1,2,3 \quad (3.3.8)$$

$$a_{ij} = 0 \quad i \neq j$$

C_{λ} = constant depending on λ

substituting Equation 3.3.7 into Equation 3.3.6 gives

$$\begin{bmatrix} I_{\parallel} \\ I_{\perp} \\ U \\ V \end{bmatrix} = \begin{bmatrix} A-B \\ 3A+2B \\ 0 \\ 0 \end{bmatrix} \quad (3.3.9)$$

From the above we find that the depolarization factor δ, will be given by

$$\delta = I_c/I_p = I_{\parallel}/I_{\perp} = (A-B)/(3A+2B) \quad (3.3.10)$$

which is independent of the scattering angle ϑ.

Now, for linear molecules as O_2, N_2, CO_2, the

polarizability tensor is $a_{\parallel}=a_{11}$ and $a_{\perp}=a_{22}=a_{33}$[47]. Substituting these values in equations 3.3.8 gives A and B, from which Equation 3.3.10 gives

$$\delta = \frac{(a_{\parallel}-a_{\perp})^2}{(a_{\parallel}+2a_{\perp})^2 + 2a_{\parallel}^2+4a_{\perp}} \qquad (3.3.11)$$

The polarizability factor for wavelengths in the 5000 to 6000 A visible range for N_2, O_2 and CO_2 molecules as given in recent literature are shown in Table 3.3.1.

Substituting these into Equation 3.3.11 gives values for δ. It should be noted that while these δ's are values for individual molecules, if it is assumed, as is reasonable with the small Rayleigh cross-sections, that only singly scattered Rayleigh radiation is relevant to the Lidar signal received, then the aggregate δ's will be the sum of the individual δ's. In fact the weighted sum of the δ's for N_2, O_2 and CO_2 is given in Table 3.3.1 as 0.0154 which is reasonable agreement with the value of δ=0.0142 measured for atmospheric dry air. The depolarization factor measured for water vapor (H_2O) molecules is[48] δ=0.01. Thus for 100% humidity at 20 °C this could add approximately 1.3% of 0.01 or 0.00013 to the value of δ=0.0142 for dry air (i.e. a negligible amount). It should be noted that this is contribution due to water vapor, not water droplets, which as will be seen in a later section, make no contribution to 180° backscatter depolarization since they are symmetrical.

As discussed in section 2.3.6.1 the Rayleigh backscatter at our 5000 Å wavelength range, for typical 10 Km visibilities, is less than the Mie backscatter by a factor of 20. Thus $\delta_{RAY}=0.0142$ will result in an effective contribution $\delta_{RAY}/20$ to the total δ resulting from both Rayleigh and Mie backscatter. As will be seen later, in the error analysis section, this amount of depolarization can be expected to have negligible effect on the accuracy of the system in measuring pollutant concentration.

3.3.4 Scattering by Symmetric and Non-Symmetric particles where $\lambda \not\ll \rho$

The general case of scattering by particles is when these particles are non-symmetric and when the wavelength, λ, is not much less than ρ, the radius of curvature at the incident surface (where $\lambda \ll \rho$ scattering is the equivalent of that from a plane surface, and will be discussed in the next section).

Now the electric vectors of incident and scattered radiation E_i and E_s can be expressed in the form

$$E_i = \begin{bmatrix} E_i \\ E_i \end{bmatrix} \text{ and } \quad E_s = \begin{bmatrix} E_s \\ E_s \end{bmatrix} \tag{3.3.12}$$

where $\perp$, $\parallel$, denote the perpendicular and parallel components respectively, with respect to the scattering plane.

The scattering matrix

$$\underset{\sim}{A} = \begin{pmatrix} A_{11} & A_{12} \\ A_{21} & A_{22} \end{pmatrix} \tag{3.3.13}$$

is defined by the relationship

$$E_s = \underset{\sim}{A} E_i \tag{3.3.14}$$

Clearly for a general case of scattering by an arbitrary shaped particle all the matrix elements are non-zero and are functions of the scattering angle, the particle shape, size orientation and material.

If for any particular particle shape or orientation the scattering matrix is diagonal (e.g. $A_{12} = A_{21} = 0$) and if the incoming radiation is linearly polarized perpendicularly to the scattering plane (i.e. $E_{i_{\parallel}} = 0$) then the Equation $E_s = \underset{\sim}{A} E_i$ shows that the scattered radiation is polarized in the same direction, i.e. $E_{s_{\parallel}} = 0$. The same is obviously true if we started of with a $\parallel$ polarization. Thus a necessary and sufficient condition for conservation of linear polarization with the electric vector perpendicular or parallel to the scattering plane is the diagonality of the scattering matrix $\underset{\sim}{A}$.

Symmeric Particles

If the scattering matrix of a given arbitrarily shaped particle with respect to a scattering plane is given by $\underset{\sim}{A}$, then it can be shown that the scattering matrix of the mirror image of the particle, $\underset{\sim}{A}'$, as reflected by the scattering plane, is given by[37]

$$\underset{\sim}{A}' = \underset{\sim}{P}^{-1}\underset{\sim}{A}\underset{\sim}{P} = \begin{pmatrix} A_{11} & -A_{12} \\ -A_{21} & A_{22} \end{pmatrix} \tag{3.3.15}$$

where

$$\underset{\sim}{P} = \underset{\sim}{P}^{-1} = \begin{pmatrix} -1 & 0 \\ 0 & 1 \end{pmatrix} \tag{3.3.16}$$

Now if the scattering particle has a reflectional symmetry with respect to the scattering plane, i.e., if the particle is identical with its mirror image about the scattering plane, then the scattering matrices $\underset{\sim}{A}$ and $\underset{\sim}{A}'$ must be identical that is

$$\underset{\sim}{A} = \begin{pmatrix} A_{11} & A_{12} \\ A_{21} & A_{22} \end{pmatrix} = \underset{\sim}{A}' = \begin{pmatrix} A_{11} & -A_{12} \\ -A_{21} & A_{22} \end{pmatrix} \tag{3.3.17}$$

This is possible only if

$$A_{12} = A_{21} = 0$$

and therefore

$$\underset{\sim}{A} = \underset{\sim}{A}' = \begin{pmatrix} A_{11} & 0 \\ 0 & A_{22} \end{pmatrix} \tag{3.3.18}$$

Thus, in general, the scattering matrix of a particle that has reflectional symmetry about the scattering plane is a diagonal matrix.

As discussed earlier this will mean that an incident wave which has its electric vector perpendicular or parallel to the scattering plane will not be depolarized by scattering from a particle which has mirror symmetry about the scattering plane.

For 180° backscatter there will therefore be no depolarization for particles which have rotational symmetry about the backscatter direction. Thus water droplets which are spherical will cause no depolarization of backscatter light nor will spherical dust particles. However, scattering at other angles that do not meet the above criteria will in general be depolarized.

Therefore, scattering from any particles, including spherical particles at other angles than 180° backscatter would be depolarized. Also clearly if the particles are not symmetrical about the backscatter direction then the backscatter would also be depolarized. Thus in the case of many rotationally symmetric particles with axes of symmetry randomly oriented, scattering at all angles, including backscattering would be depolarized . The aggregate scattered signal in any one direction from such a collection of randomly oriented symmetrical particles, e.g. needle shaped, would also therefore be depolarized.

Non symmetrical particles

Particles without an axis of symmetry would have for any orientation

$$A_{12} \neq A_{21} \neq 0$$

Under these conditions the scattering matrix

$$\underset{\sim}{A} = \begin{pmatrix} A_{11} & A_{12} \\ A_{21} & A_{22} \end{pmatrix}$$

could never reduce to a diagonal matrix thus scattering in any direction will undergo changes in polarization. The scatter from an aggregate of randomly shaped particles in any direction, given by

$$E_s = \underset{\sim}{A} E_i$$

will also be depolarized with respect to the incident signal, even for 180 backscatter.

3.3.5 Scattering by Large Particles

For large particles, at an incident surface where it can be assumed that the radius of curvature, $\rho >> \lambda$, the wavelength of the scattered light, it is reasonable to analyze the scattering from such a surface in the context of scattering from a plane, and determine the extent of depolarization that can be expected for scattered light in these circumstances.

Let a plane wave E_1 linearly polarized be incident on a

plane sheet with arbitrary electrical characteristics bounded by a contour C located at, or about the origin of a rectangular coordinate system x,y,z with unit vectors x_o, y_o, z_o as shown in Figure 3.3.1. Let k_1 be a unit vector in the direction of the incident wave, lying in the xy plane and making an angle ϑ_1, with the z axis. The polarization factor p_1 of the incident wave E_1 is defined through its components E_1^+, E_1^-, in the direction of the unit vectors e_1^- parallel to y_o, and e_1^+ perpendicular to e_1^- and k_1, so that e_1^-, e_1^+, k_1 form an orthogonal triplet, with $p_1 = E_1^+/E_1^-$. The scattered wave from the plane sheet propagating into direction ϑ_2, ϑ_3, as indicated in Figure 3.3.2, far from the scatterer must become plane and transversal. Then its electric field may be resolved into two components in the directions of the unit vectors e_2^- parallel to the xy plane, and e_2^+ such that e_2^+, e_2^-, k_2 form an orthogonal triplet, where k_2 is a unit vector in the direction of the scattered wave.

The basic problem is to find p_2 when p_1, the input-output geometry ϑ_1, ϑ_2, ϑ_3, and the geometrical and electrical characteristics of the scatterer are given. Let P be the point of observation of the scattered field by the surface S. Then the scattered field E_2 at P is given by the Helmholtz integral[49]

$$E(P) = \frac{1}{4\pi} \iint \left(E\frac{\partial}{\partial n} - \frac{\partial E}{\partial n} \right) dS \qquad (3.3.19)$$

where

$$\Psi = \frac{\exp(j2\pi R/\lambda)}{R'}$$

and R' is the distance from a variable point B on S. Considering the scattering surface flat lying in the xy plane we get on the surface S (except near its edges)

$$(E^{\pm})_S = (1+R^{\pm})\, E_1^{\pm}$$

e.g. equals to the incident plus the reflected field by taking the magnetic field $(H^{+})_S = (1-R^{+})\, H_1$ and using Maxwell's Equation $\nabla \times E = -\epsilon \frac{\partial H}{\partial t}$

we get

$$(\frac{\partial E^{\pm}}{\partial z})_S = (1-R^{\pm})E_1^{\pm}\, k_1 \cdot z_o$$

where R is the Reflection coefficient depending on the angle of incidence, the electric properties of the reflecting material and the polarization of the incident wave. Using the field expressions for the two components + and - we get

$$(E^{+})_S = (1+R^{+})E_1 \ , \quad (E^{-})_S = (1+R^{-})E_1$$

$$(\frac{\partial E^{+}}{\partial n})_S = (1-R^{+})E^{+}k_1 \cdot z_o,$$

and,

$$\left(\frac{\partial E^-}{\partial n}\right)_S = (1-R^-)E^- k_1 . z_o,$$

where R^+, R^- are the Fresnel reflection coefficients for the two components.

Let $r = xx_o + yy_o + zz_o$

be the radius vector of the coordinate system. Then if P is sufficiently distant from the origin (in the Fraunhofer zone) we can write (Figure 3.3.2)

$$R' = R_o - k_2 . r$$

Substituting the above equations into the integral equation we obtain.

$$E_2 = -\frac{j \exp\{j\, 2\pi\, R_o/\lambda\}}{4\pi R_o} E_1 \left[(1+R)\cos\vartheta_2 - (1-R)\cos\vartheta_1 \right. \tag{3.3.20}$$

$$\left. \times \iint_S \exp\{(j(k_1 - k_2).r)\}dxdy \right.$$

On taking the ratio of the components (+ and -) for E_1 and E_2 we obtain the polarization relation

$$p_2 = \left[\frac{(1+R^+)\cos\vartheta_2 - (1-R^+)\cos\vartheta_1}{(1+R^-)\cos\vartheta_2 - (1-R^-)\cos\vartheta_1}\right] p_1 \tag{3.3.21}$$

where

$$p_1 = \frac{E_1^+}{E_1^-} \qquad \text{and} \qquad p_2 = \frac{E_2^+}{E_2^-}$$

Thus in general depolarization will occur. This is true theoretically even for 180 backscattering where $\vartheta_2 = -\vartheta_1$ and $\vartheta_3 = 0$ where the above Equation 3.3.21 reduces to

$$p_2 = (R^+/R^-)p_1$$

giving depolarization (even for perfect conductors where $R^+ = 1$, $R^- = -1$) except for radiation with polarization $p_1 = 0$ or ∞, i.e. with polarization parallel or perpendicular to the scattering surface. According to Equation 3.3.21 above, however, there will also be no depolarization ($p_1 = p_2$) when $\vartheta_1 = \vartheta_2 = \vartheta_3 = 0$, i.e. when the incident and reflected radiation are normal to the scattering surface, i.e. this is true for 180 backscatter from a normal surface of incidence.

Furthermore, while Equation 3.3.21 shows theoretical depolarization existing for $\vartheta_1 = -\vartheta_2$, $\vartheta_3 = 0$ corresponding to non-perpendicular 180° backscatter, it should be noted that the amplitude of scattered radiation from a plane will vanish to zero when the scattering is 180 backscattering, where the normalized amplitude is given by[71]

$$v = \sqrt{\sin^2\vartheta_1 - 2\sin\vartheta_1\sin\vartheta_2\cos\vartheta_3 + \sin^2\vartheta_2}$$

which gives $v = 0$ for $\vartheta_1 = -\vartheta_2$ and $\vartheta_3 = 0$. Since the analysis given above was arbitrary with respect to conductivity, the results are true regardless of conductivity.

Thus in general, scattering from particles where, for the scattering surface $\rho >> \lambda$, 180° backscatter will not be depolarized, while scattering at other angles will be.

3.3.6 Combined effects of various Depolarization mechanisms

The previous sections have shown that direct ($\vartheta = 180^{\circ}$) backscatter will not be depolarized with respect to the primary beam for backscatter from:

- Particles (whether conductive, dielectric or lossy) which have rotational symmetry, about the incident direction including water droplets.
- particles where, ρ, the radius of curvature of the reflecting surface is much larger than the wavelength of the scattered light. In this case direct backscattering is, in a sence, specular and as such is not depolarized.

It was also seen in the earlier discussion that very small, i.e. negligible depolarization, occurs due to Rayleigh backscattering (180°) from atmospheric molecules, including water vapor molecules.

On the other hand from the physical optics approximation, it was also seen that depolarization occurs in the case of particulate 180° backscattering where the wavelength, λ is of the same order, or bigger than ρ, the radius of curvature at the incidence surface. Furthermore as discussed in the previous sections, scattering by large particles or symmetric particles at angles other than single step 180° backscatter will also result in depolarization

with respect to the incident beam.

As a consequence of the above, the two expected main sources of depolarization in signals backscattered to the Lidar receiver can be identified.

These are shown schematically in Figures 3.3.3 and 3.3.4. The first one , Figure 3.3.3, is the depolarization of $\vartheta = 180^{\circ}$ single process backscattered radiation from non-symmetric particles, where the wavelength λ is not much smaller than ρ, the radius of the particle reflecting surface. In that case the backscattered component would be, as discussed earlier, depolarized.

Figure 3.3.4, illustrates possible multiple scattering effects resulting from both symmetric and non-symmetric particles where the scattering path is ABCA, say. Under these circumstances the light scattered both times at an angle other than $\vartheta = 180^{\circ}$ backscatter, or forward scatter, will be depolarized. Again, it can be deduced because of the random orientation of particles and scattering angles that backscattered light scattered more than once reaching the Lidar receiver will generally be unpolarized. Because the backscatter coefficients are all relatively small, for typical visibilities (5-20 Km), multiple scattering resulting from more than two interactions can be neglected (e.g. ABDEA, Figure 3.3.4).

Clearly detected depolarization resulting from multiple scattering, will be decreased if the acceptance angle of the receiver, is reduced from α, Figure 3.3.5a, to α', Figure

3.3.5b since the multiple scattered component in the total backscatter received is reduced. Furthermore, since the amount of multiple scattering entering the receiver is approximately dependant on the area in the backscattering plane that is viewed by the receiver it can be expected to increase with the square of the receiver field of view α, at least for small receiver acceptance angles, until intensity along the scattering plane starts to be decreased more rapidly, by the inverse square law and hence reduce the rate of increase of the polarized backscatter with acceptance angle (ultimately theoretically to $\mathring{0}$).

Thus the total depolarized backscatter is expected to be the sum of the single step 180^{o} backscatter processes from non-symmetric particles, plus the component due to multiple (two-step) scattering from both symmetric and assymetric, large ($\rho>>\lambda$) and small particles. If the field of view, α is larger than the outgoing beam divergence D, the first component due to single process backscatter will be constant as the receiver acceptance angle α is further increased. Thus the total depolarized component under these circumstances will be a component constant with increasing α, (beyond α=D) due to single step 180^{o} backscatter, plus a component that increases initially approximately with α^2 then more slowly due to multiple (two-step) backscatter process.

Without knowing the density distribution of nonsymmetric particles, and the relative density of symmetric ones it is

not possible to make an estimate of relative magnitude of the components. As will be seen in the results of field experiments the amount of depolarization in received backscatter does bear the expected relationship to the acceptance angle. Furthermore for small and readily attainable output beam divergence and receiver acceptance angles total undesired depolarization light detected in the receiver can be kept to negligible values.

3.4 Depolarization Error Analysis

In the previous sections, the depolarization of a linearly polarized component of light was seen as the result of its interaction with matter. Physically it was associated with the appearence of an additional cross-polarized component and mathematically it was expressed using the linear depolarization ratio δ.

In the polarization discrimination lidar scheme the transmitted signals at each of the two wavelengths are orthogonally polarized and the backscattered signal components are measured with respect to the incident polarization directions. The undesired depolarization that occurs with backscatter is shown in previous sections of this Chapter as well as in Chapter 5 to be small, generally of the order of 1.5% under typical visibility conditions. That depolarization though small, would introduce errors into the lidar return data and hence into the computation for pollution concentration discussed in Chapter 2.

To analyse errors arising from depolarization effects it is necessary to reexamine Equations 2.3.24 and 2.3.25 which show how pollution concentration at range R, ΔR, is derived from the lidar return signals at wavelengths λ_1 and λ_2.

$$\bar{N}_r = \frac{1}{2\Delta\sigma\Delta R} \ln \left[\frac{\dfrac{P_r(R,\lambda_1)}{P_r(R,\lambda_2)}}{\dfrac{P_r(R+\Delta R,\lambda_1)}{P_r(R+\Delta R,\lambda_2)}} \right] = \frac{\ln(1+\Delta F_r)}{2\Delta\sigma\Delta R} \qquad (3.4.1)$$

Ideally, with the polarization discrimination scheme, the returns at λ_1 will be orthogonally polarized to those at λ_2. In practice, the backscatter process will introduce a depolarized component at each of the two wavelengths.

If it is assumed that at range R, both return signals are depolarised by the same ratio δ_1, and at range R+ΔR by the ratio δ_2, then the ratio of received signal intensities are altered as discussed below.

at range R.

$$\frac{P_r(R,\lambda_1)}{P_r(R,\lambda_2)} \longrightarrow \frac{P_r(R,\lambda_1) + \delta_1 P_r(R,\lambda_2)}{P_r(R,\lambda_2) + \delta_1 P_r(R,\lambda_1)} =$$

$$\frac{P_r(R,\lambda_1) + \delta_1 P_r(R,\lambda_2)}{P_r(R,\lambda_2)} \left[\frac{1}{1 + \frac{\delta_1 P_r(R,\lambda_1)}{P_r(R,\lambda_2)}} \right] \simeq$$

$$\frac{P_r(R,\lambda_1) + \delta_1 P_r(R,\lambda_2)}{P_r(R,\lambda_2)} \left[1 - \frac{\delta_1 P_r(R,\lambda_1)}{P_r(R,\lambda_2)} \right] =$$

$$\frac{P_r(R,\lambda_1)}{P_r(R,\lambda_2)} - \frac{\delta_1 P_r^2(R,\lambda_1)}{P_r(R,\lambda_2)} + \frac{\delta_1 P_r(R,\lambda_2)}{P_r^2(R,\lambda_2)} - \frac{\delta_1^2 P_r(R,\lambda_1)}{P_r(R,\lambda_2)} \simeq$$

and neglecting second order δ_1 terms it becomes approximately equal to

$$\frac{P_r(R,\lambda_1)}{P_r(R,\lambda_2)} \left[1 - \frac{\delta_1 P_r(R,\lambda_1)}{P_r(R,\lambda_2)} + \frac{\delta_1 P_r(R,\lambda_2)}{P_r(R,\lambda_1)} \right] \qquad (3.4.2)$$

At range $r+\Delta R$.

$$\frac{P_r(r+\Delta R,\lambda_1)}{P_r(R+\Delta R,\lambda_2)} \longrightarrow \frac{P_r(R+\Delta R,\lambda_1) + \delta_2 P_r(R+\Delta R,\lambda_2)}{P_r(R+\Delta R,\lambda_2) + \delta_2 P_r(R+\Delta R,\lambda_1)} = \qquad (3.4.3)$$

$$\frac{P_r(R+\Delta R,\lambda_1)}{P_r(R+\Delta R,\lambda_2)}\left[1-\frac{\delta_2 P_r(R+\Delta R,\lambda_1)}{P_r(R+\Delta R,\lambda_2)}+\frac{\delta_2 P_r(R+\Delta R,\lambda_2)}{P_r(R+\Delta R,\lambda_1)}\right]$$

and using Equations 3.4.2 and 3.4.3 into Equation 3.4.1

$$\bar{N}_r=\frac{1}{2\Delta\sigma\Delta R}\ln\left[\frac{\frac{P_r(R,\lambda_1)}{P_r(R,\lambda_2)}}{\frac{P_r(R+\Delta R,\lambda_1)}{P_r(R+\Delta R,\lambda_2)}}\left[\frac{1-\frac{\delta_1 P_r(R,\lambda_1)}{P_r(R,\lambda_2)}+\frac{\delta_1 P_r(R,\lambda_2)}{P_r(R,\lambda_1)}}{1-\frac{\delta_2 P_r(R+\Delta R,\lambda_1)}{P_r(R+\Delta R,\lambda_2)}+\frac{\delta_2 P_r(R+\Delta R,\lambda_1)}{P_r(R+\Delta R,\lambda_2)}}\right]\right]$$

$$\bar{N}_r=\frac{1}{2\Delta\sigma\Delta R}\ln\left[\frac{\frac{P_r(R,\lambda_1)}{P_r(R,\lambda_2)}}{\frac{P_r(R+\Delta R,\lambda_1)}{P_r(R+\Delta R,\lambda_2)}}\left[1-\frac{\delta_1 P_r(R,\lambda_1)}{P_r(R,\lambda_2)}+\frac{\delta_1 P_r(R,\lambda_2)}{P_r(R,\lambda_1)}\right]\times\left[1+\frac{\delta_2 P_r(R+\Delta R,\lambda_1)}{P_r(R+\Delta R,\lambda_2)}-\frac{\delta_2 P_r(R+\Delta R,\lambda_2)}{P_r(R+\Delta R,\lambda_1)}\right]\right]$$

Again, neglecting second order δ terms

$$\bar{N}_r = \frac{1}{2\Delta\sigma\Delta R} \ln \left[\frac{\frac{P_r(R,\lambda_1)}{P_r(R,\lambda_2)}}{\frac{P_r(R+\Delta R,\lambda_1)}{P_r(R+\Delta R,\lambda_2)}} \left[1 + \frac{\delta_2 P_r(R+\Delta R,\lambda_1)}{P_r(R+\Delta R,\lambda_2)} - \frac{\delta_2 P_r(R+\Delta R,\lambda_2)}{P_r(R+\Delta R,\lambda_1)} + \right. \right.$$

$$\left. \left. + \frac{\delta_1 P_r(R,\lambda_2)}{P_r(R,\lambda_1)} - \frac{\delta_2 P_r(R,\lambda_1)}{P_r(R,\lambda_2)} \right] \right] \qquad (3.4.4)$$

Let

$$\frac{P_r(R,\lambda_1)}{P_r(R,\lambda_2)} = Q \qquad (3.4.5a)$$

and using ΔF_r from equation 3-21

$$\frac{P_r(R+\Delta R,\lambda_1)}{P_r(R+\Delta R,\lambda_2)} = \frac{Q}{1+\Delta F_r} \qquad (3.4.5b)$$

where ΔF_r is dependent on pollution concentration and is typically 0.1.

Then from Equations 3.4.4 and 3.4.5

$$\bar{N}_r \quad \frac{1}{2\Delta\sigma\Delta r} \ln \left[(1+\Delta F_r) \left[1 + \frac{\delta_2 Q}{1+\Delta F_r} - \frac{\delta_2 (1+\Delta F_R)}{Q} + \frac{\delta_1}{Q} - \delta_1 Q \right] \right] =$$

$$\frac{1}{2\Delta\sigma\Delta r} \ln \left[1+\Delta F_r+\delta_2 Q - \frac{\delta_2 (1+\Delta F_r)^2}{Q} + \frac{\delta_1 (1+\Delta F_r)}{Q} - \delta_1 (1+\Delta F_r) Q \right] =$$

$$\frac{1}{2\Delta\sigma\Delta r}\ln\left[1+\Delta F_r+\delta_2 Q - \frac{\delta_2(1+\Delta F_r^2+2\Delta F_r)}{Q} + \frac{\delta_1}{Q} + \frac{\Delta F_r}{Q} - \delta_1 Q - \delta_1 \Delta F_r Q\right]$$

or cancelling the ΔF_r products

$$\bar{N}_r \simeq \frac{1}{2\Delta\sigma\Delta r}\ln\left(1 + \Delta F_r + \delta_2 Q - \frac{\delta_2}{Q} + \frac{\delta_1}{Q} - \delta_1 Q\right)$$

or

$$\bar{N}_r \simeq \frac{1}{2\Delta\sigma\Delta r}\ln\left[1 + \Delta F_r + (\delta_2 - \delta_1)Q - \frac{(\delta_2 - \delta_1)}{Q}\right] \qquad (3.4.6)$$

Furthermore, since ΔF_r and the remaining terms are small, Equation 3.4.6 can be approximated by

$$\bar{N}_r \simeq \frac{1}{2\Delta\sigma\Delta r}\left[1 + \Delta F_r + (\delta_2 - \delta_1)Q - \frac{(\delta_2 - \delta_1)}{Q}\right] \qquad (3.4.7)$$

In the ideal polarization discrimination scheme, Lidar $\delta_1=\delta_2=0$. In practice, as will be seen in the results of Chapter 5, δ_1 and δ_2 are likely to be of the order of 0.015. However, since it is the term $\delta_2-\delta_1$ that is in the equation, the errors arising from depolarization will be less. And unless there are very different characteristics to the

backscatter depolarizations, δ_1 and δ_2, at range R and R+ΔR, then $\delta_1-\delta_2$ will be very small. With an upper limit of δ in the region of 1.5 percent, it is difficult to see $\delta_2-\delta_1$ >0.005 say.

Now Q, the ratio of the return signals at $\lambda_1$and λ_2, can be practically expected to be limited to a range between 1 and 1.6 approximately (depending on the pollution concentrations and ranges of measurement).

Comparison of Equation 3.4.1 with Equation 3.4.7 shows that the error in the calculation of the pollutant concentration, due to depolarization is given by

$$e = (\delta_2 - \delta_1)Q - \frac{(\delta_2 - \delta_1)}{Q} \qquad (3.4.8)$$

Thus the largest value of the error occuring within the range of the expected values of Q is for Q=1.6 which gives, using Equation 3.4.8

$$e = \delta_2 - \delta_1$$

which is likely to be less than 0.005. This in turn, represents a possible error of 5 percent of the value of ΔF_r if ΔF_r=0.01 (typical value), and hence in the computation of pollution concentration at range R, over a sample length ΔR. If ΔF_r is actually less than the typical 0.1 (assumed above) then the fractional error is

proportionally greater.

Examination of Equation 3.4.8 shows that if Q = 1 then errors introduced due to depolarization disappear and N_r is given by the error free equation.

$$\bar{N}_r = \frac{\Delta F_r}{2\Delta\sigma\Delta R} \tag{3.4.9}$$

Thus if it is desired to obtain greater accuracy it is possible to vary the relative intensity of the laser output at λ_1 and λ_2 to ensure that Q for a given range is nearly equal to 1. That can be readily achieved through the insertion of an intracavity variable attenuator into one of the two legs of the simultaneous two-wavelength laser cavity configuration. This attenuation can then be adjusted in successive shifts so that the ratio of the received signals from range R becomes nearly equal to 1, and hence practically eliminate errors due to backscatter depolarization.

Conclusion

Depolarization effects due to atmospheric scattering show that undesired depolarized signals may be detected by the Lidar receiver in the polarization discrimination scheme due to 180^o backscatter from small non-symmetric particles plus multi (two step) backscatter processes from any particles. The latter effect may be reduced by decreasing

receiver field of view. Error analysis shows that because of the relative nature of measurements needed to be carried out with the polarization discrimination scheme, errors due to unwanted depolarizations in received backscatter signal are likely to be minimized, and if desired can be eliminated.

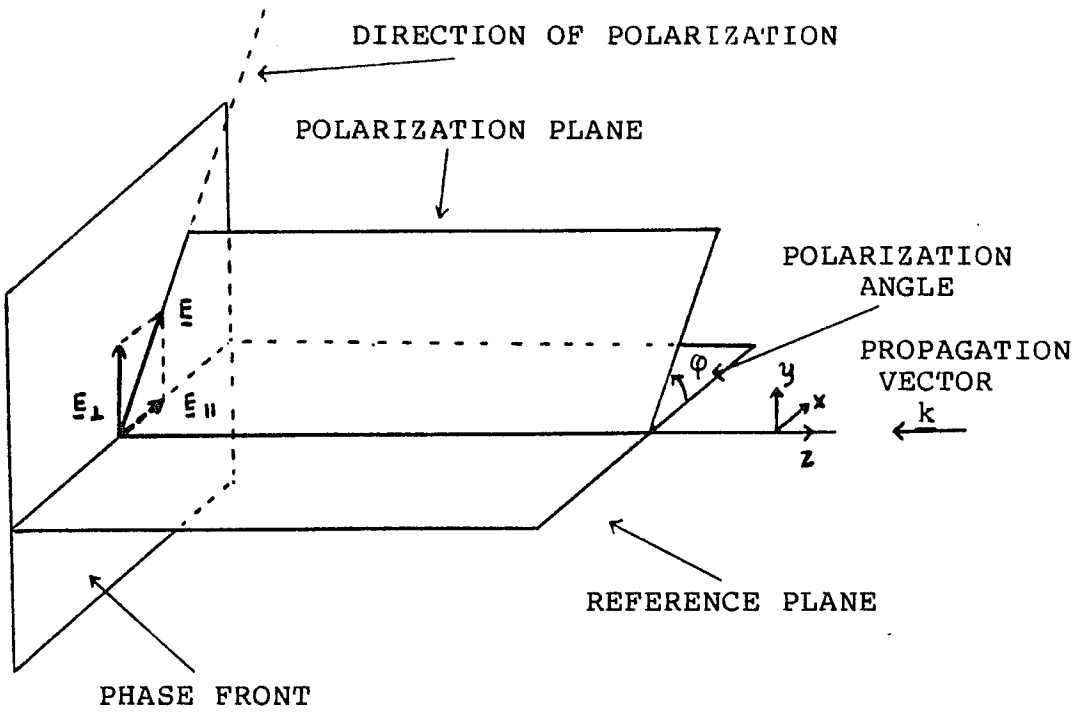

FIGURE 3.2.1 Orientation of the electric vector $\underline{E}$ at an instant of time, with respect to the plane of reference for a wave propagating along the -z direction.

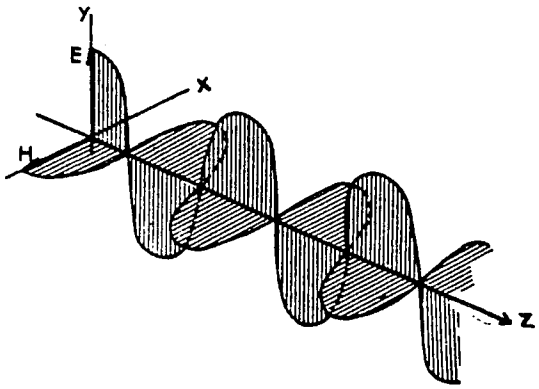

FIGURE 3.2.2 Linearly polarized plane electromagnetic wave.

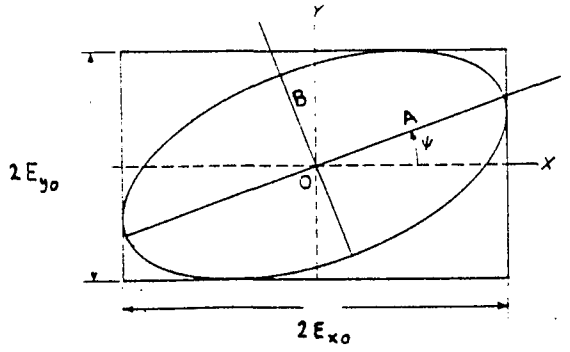

FIGURE 3.2.3 Vibration ellipse for the electric vector.

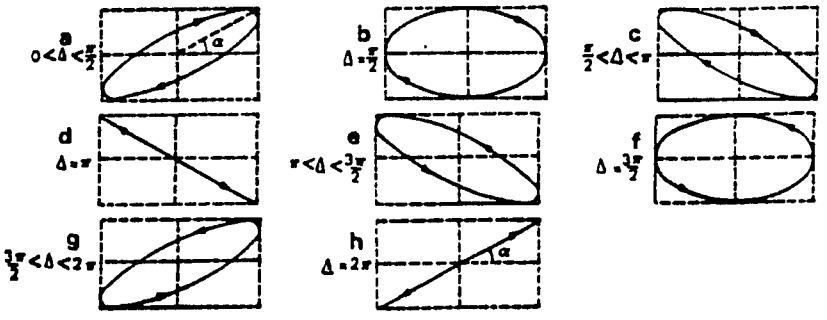

FIGURE 3.2.4 Variation in the form of an elliptical vibration with phase difference.

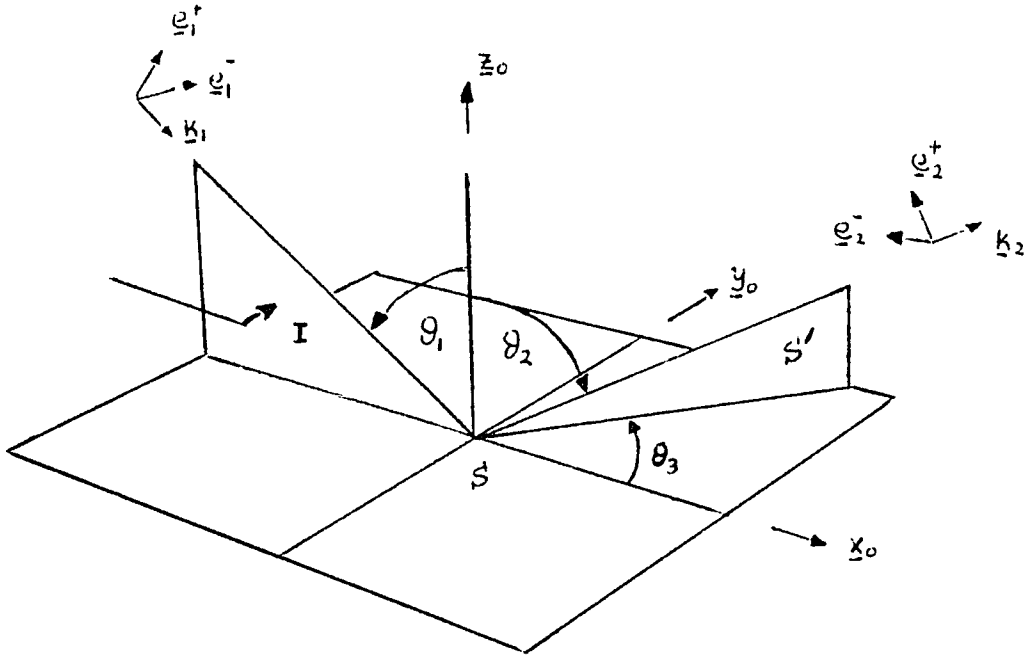

FIGURE 3.3.1 Coordinate system used for describing a general case of depolarization

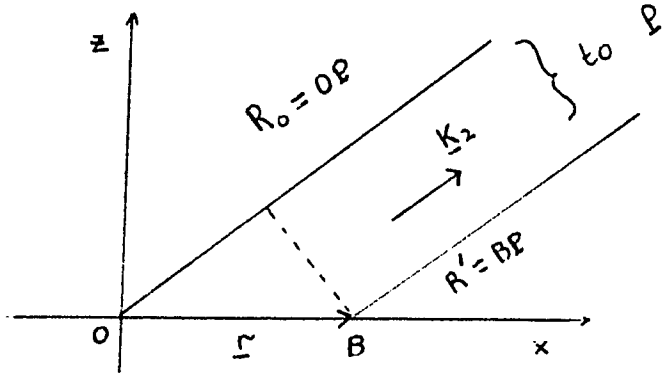

FIGURE 3.3.2 Field scattered from flat surface at distant point P.

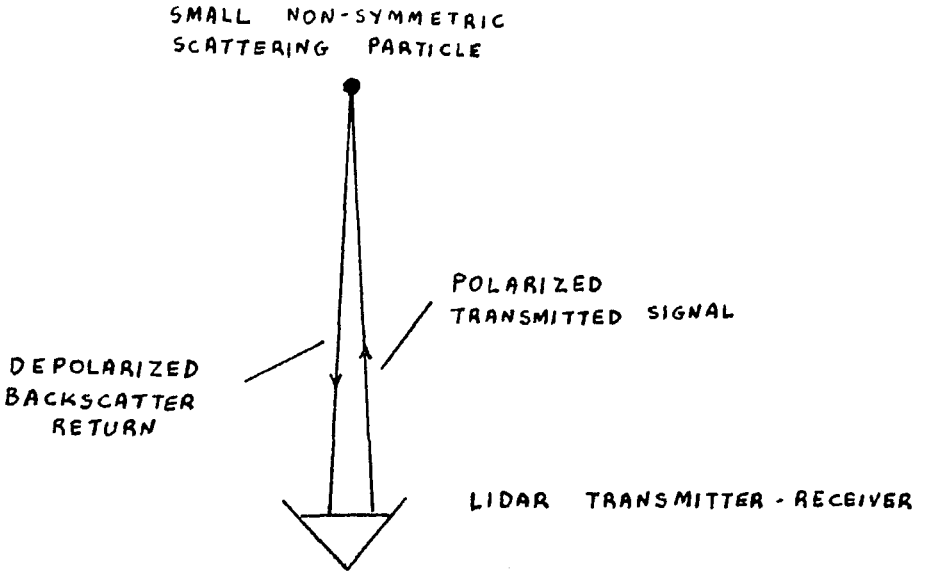

FIGURE 3.3.3 Single step 180 backscatter from small non-symmetric particle where ρ is comparable to λ.

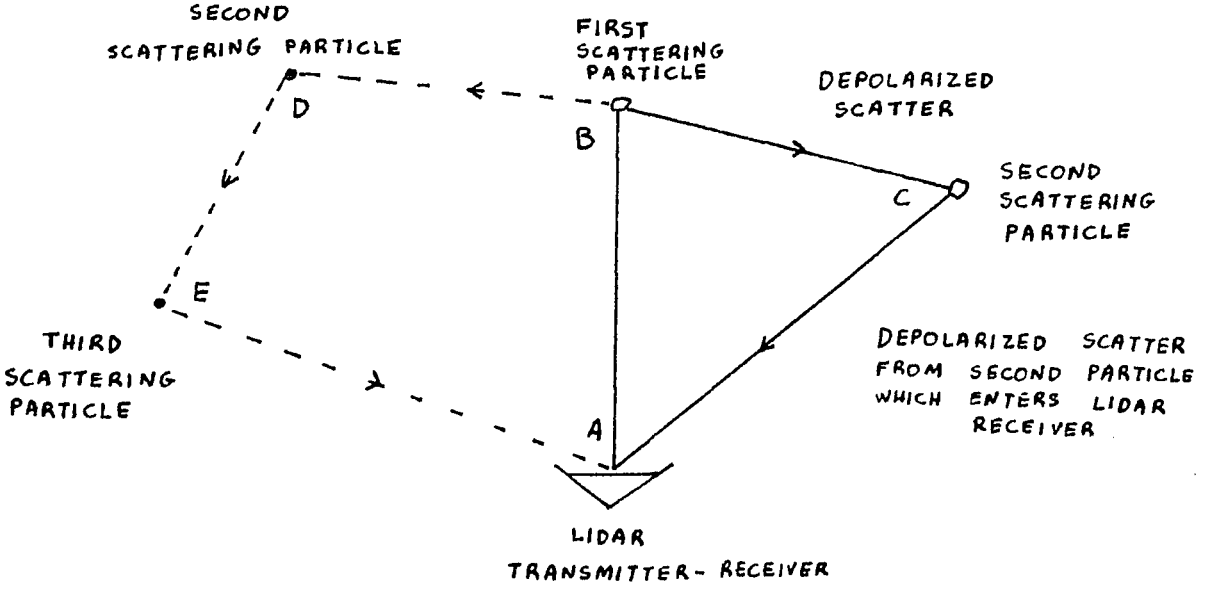

FIGURE 3.3.4 Multiple scattering effects showing two and three step scattering processes.

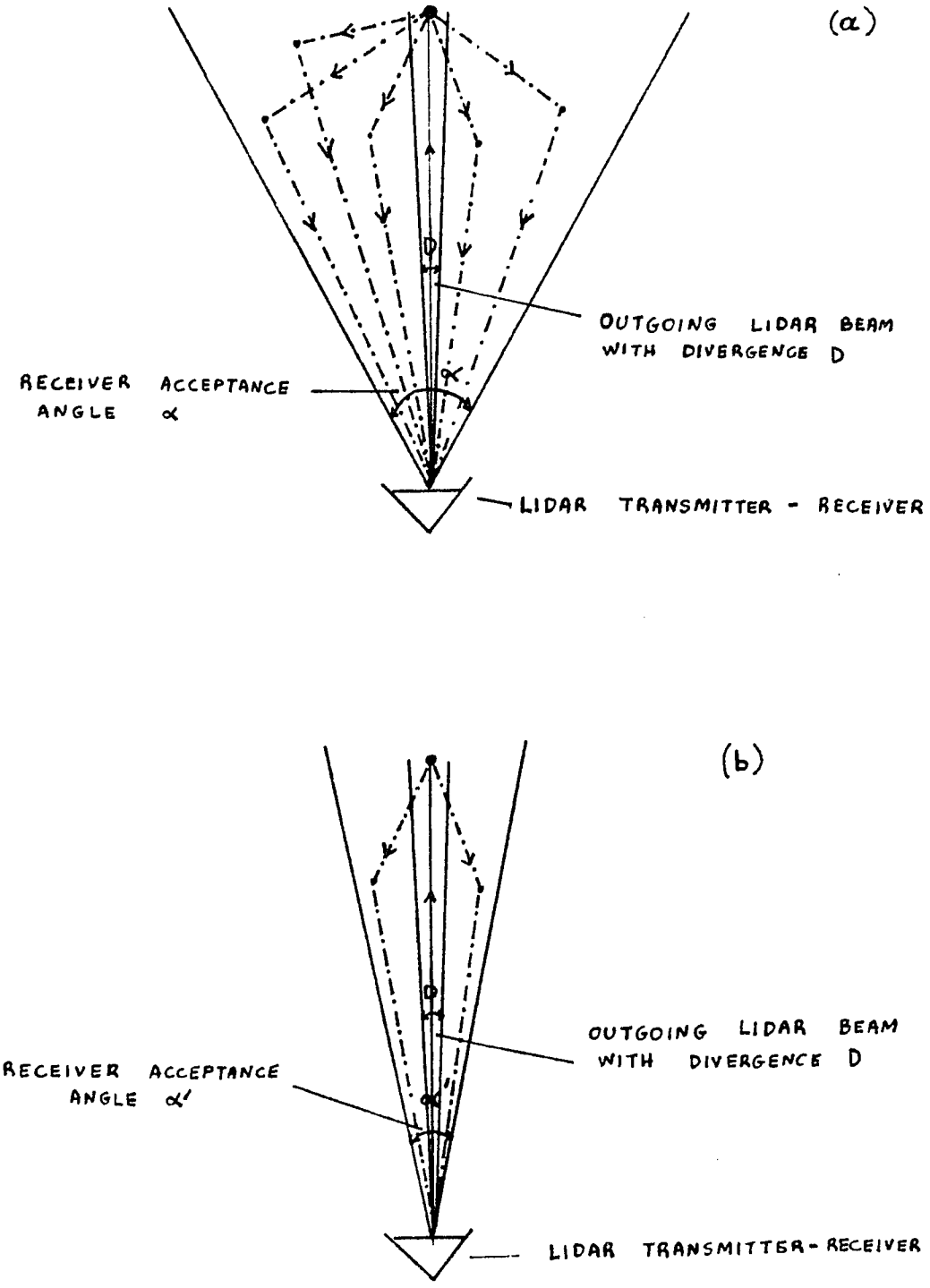

FIGURE 3.3.5a,b Reduction in multiple backscatter detected as a function of the receiver acceptance angle α and α'.

Molecule	Per cent per unit air volume	$a_{\parallel}$ ($10^{24}cm^3$)	$a_{\perp}$ ($10^{24}cm^3$)	δ	Weighted value of δ (δ x percentage in air)
N_2	78.084	2.22	1.53	0.010	0.0078
O_2	20.946	2.32	1.23	0.030	0.0063
CO_2	0.033	4.03	1.93	0.040	0.0013
Dry Air	100			0.0142	0.0154

TABLE 3.3.1 Polarizabities and δ factors for atmospheric molecules.

CHAPTER 4

POLARIZATION DISCRIMINATION LIDAR SYSTEM

4.1 Introduction

The basic polarization discrimination Lidar system consists of a flashlamp pumped dye laser transmitter and an optical receiver shown schematically in Figure 4.1.1. The system is required to produce co-linear laser outputs at two close-lying wavelengths λ_1 and λ_2, simultaneously, that are orthogonally polarized. These outputs are transmitted from the system as a single beam co-linear with the axis of the Lidar optical receiver. In the receiver, the backscattered returns, at each of the two wavelengths, still each orthogonally polarized with respect to the other, are separated (discriminated between) and detected separately.

To demonstrate the viability of the polarization discrimination scheme, the Lidar system was designed for the detection of NO_2 with the two close-lying wavelengths situated at 4478.5 Å and 4500 Å corresponding to an absorption peak and trough in the NO_2 absorption spectrum. The main elements of the Lidar system are discussed briefly below, with consideration given to their features, which impact on the polarization discrimination scheme.

4.2 Optical Receiver

A schematic diagram of the optical Lidar receiver is shown in Figure 4.2.1, while photographs of it are shown in Figure 4.2.1a, indicating the different components.

The primary lens of the optical receiver is an acrylic Fresnel lens (purchased from Fresnel II, Inc.) mounted on a light-tight steel frame which was designed for the purpose. This lens is basically a flat thin piece of a plastic on which a series of concentric stepped zones extending from the center to the edge are molded. Figure 4.2.2 illustrates the geometric relationship between the zones on the Fresnel lens and the surface of an ordinary lens. Each zone refracts the incident light so that the combined action of each refracting facet focuses light essentially in the same manner as a conventional lens.

The lens used has a focal length of 24 inches, a diameter of 15 inches, and a thickness of 1/8 inch. With concentric zones spaced approximately 125 grooves per inch, the lens is capable of forming a sharp image for objects near the optical axis. This is appropriate, since our Lidar receiver does not require a wide field of view for collecting the light directly backscattered from the outgoing beam which has a divergence of less than 1 miliradian.

For the Fresnel lens, the circle of least confusion for collimated light directed parallel to the optical axis was measured and found to be approximately one centimeter. In

the plane containing the circle of least confusion, the spatial distribution of the collected light is a bright spot of the above diameter with the surrounding area weakly illuminated by light spuriously scattered at the edges of the concentric zones of the Fresnel lens. To eliminate the spurious light, an iris was placed in the plane containing the circle of least confusion. By varying the iris diameter, the receiver field of view may be narrowed or expanded. The Frensnel lens used in this system costs far less than a comparable parabolic mirror, yet its quality is quite acceptable for our Lidar application.

The backscattered light collected by the Fresnel lens is collimated by a 1.5 inch diameter lens. The collimated light is then split according to polarization by means of a calcite polarizing beam splitter which has a principal transmittance ratio of approximately 10^6.

To properly achieve the critically important alignment of the beam splitter with respect to the (orthogonal) polarizations of the outgoing and return signals, all alignments were made with respect to vertical and horizontal direction with water levels and plumblines, then checked optically for final accuracy with a He-Ne laser and front surface reflectors. Each of the separated beams (which correspond to each of the probe wavelengths, 4478.5 Å and 4500 Å respectively) is directed to a separate photomultiplier, each covered with a broadband filter centered at each of the two wavelengths at 4478.5 and 4500 Å

respectively. In fact only one filter centered at an in between wavelength 4490 Å was really needed, and could have been placed in front of the calcite beam splitter to cover both wavelengths. The two broadband filters were used, because they were readily available from previous experiments, and using them eliminates the necessity for ensuring light tightness of the receiver region from the collimator to the photomultipliers. The interference filters have both measured half bandwidth of 48 and 55 Å, centered at 4478.5 Å and 4500 Å respectively. See Figures 4.2.3a and 4.2.3b.

The photomultipliers used are Amperex type 56 AVP and their outputs, corresponding to the backscatter return signals are displayed on Tektronix type 549 storage oscilloscopes and recorded photographically.

4.3 The Dye Laser

4.3.1 The Laser Head

The basic laser system consists of a flashlamp-pumped organic-dye laser. The laser head is constructed in a coaxial arrangement in which the flowing dye is uniformily excited by an annular discharge surrounding the active medium. See Figure 4.3.1. The laser head, model DL2100B, and discharge circuitry was purchased from the Phase-R Company, and was chosen for maximum energy output and shortest possible pulse width. Figure 4.4.2 shows the laser head situated in the Lidar system, and Figure 4.3.3 shows a

typical output pulse.

The organic dye, 7-diethylamino-4-methyl coumarine, dissolved in ethanol was used as the lasing medium. A concentration of 3×10^{-5} M/l was found to give maximum output energy consistent with a laser line-width that was less than the halfwidth of the absorption peak of NO_2 to be measured, i.e., less than approximately 10 A for the 4478.5 Å absorption peak. In this manner, it was possible to maximize the return signal, thereby increasing range, and still retain the maximum difference between absorption peak and trough, and thus attain the sensitivities that the system is capable of.

4.3.2 Dye Laser Mechanism - main features and practical factors effecting operation

Organic molecules possess a lowest excited singlet state, $^1S^*$, and fluorescence when it occurs, originates from this state. In making a fluorescent transition the molecule reverts back to its ground state, ^1S_o, while simultaneously emitting radiation.

The spectrum of the fluorescent radiation from an organic dye often has more than one maximum, and it usually spans a region no less than several handred angstroms wide. The reason for this large bandwidth is that the radiation is actually made up of hundreds of components, corresponding to transitions originating from various sublevels of the first excited singlet state and terminating at various sublevels

of the ground state. These sublevels are associated with specific vibrations of the molecule as a whole. See Figure 4.3.2. Since some of the vibrational sublevels of the ground state may be high enough in energy so that they are normally unoccupied, a population inversion sufficient for laser action can be established between the states from which fluorescence originates and some of the higher vibrational levels of the ground state.

Once threshold conditions are reached, the laser light that is produced has frequencies centered about one of the broad fluorescence peaks. The bandwith of such broadband operation can range up to 250 $\mathring{A}$ for flashlamp-pumped dye lasers.

To reduce the naturally large bandwidth of the flashlamp-pumped dye laser output, a tuning element such as a diffraction grating can be placed in the laser cavity. With the proper choice of grating characteristics, such as blaze wavelength, grooves per millimeter, and power-density handling capabilities, e.t.c., the desired laser frequency and bandwidth are attainable, and may be chosen to match the absorption peak and troughs for NO_2.

The dye temperature has an important effect on lasing wavelength and output efficiency. If the dye is allowed to get hot, fluorescence is broadened and lasing is red shifted. Higher reabsorption takes place, the gain becomes lower and the laser output decreases. Experiments have also shown that too low a temperature of the dye also decreases

the output efficiency.

To control the temperature the flowing dye is cooled by flow through a tap-water cooled heat exchanger. This cooling system permits the temperature of the dye to be kept fairly constant at approximately 15 ^{o}C, where the laser was empirically found to operate more efficiently.

Since the dye fluid is actually flowing inside the optical laser cavity, scattering could have a pronounced effect on the laser efficiency. It is therefore important to remove particulate matter from the dye solutions before using them in the recirculating system. This particle removal is achieved by filtering the dye through mechanical filters with pore sizes smaller than the laser wavelengths. Filtering of dyes in this manner typically results in a two-fold increase in laser output in comparison to the unfiltered output. Thus for the same output energy, the laser can be operated at lower flashlamp pump energies, greatly enhancing lifetimes of all the components.

4.3.3 Intra-Cavity Grating for Wavelength Selection

To tune the laser outputs to the required wavelengths, at 4478.5 Å and 4500 Å, gratings were used in a Littrow configuration with the Blaze angle in the first order. In this manner, all the other orders extinguish and the diffracted energy is concentrated in the first order (at the wavelength desired).

Gratings have different efficiencies (percentange of

light incident on a grating that is diffracted into the desired order) for light that is polarized perpendicularly or in parallel to the groove profile. For the gratings used, perpindicularly polarized light gives the better efficiency. This is no detriment to our system, since as will be seen in the next section, a polarizing beam splitter is introduced intra-cavity to simultaneously produce outputs at two wavelengths that are orthogonally polarized.

It should be noted, that the bandwidth of the laser lines obtained are determined by the dispersion of the grating and the effective aperture crated by the geometry of the lasing medium, which in turn depends upon the distance of the grating from the laser head. The dispersion of the grating is the angular separation obtained for two different radiations. Therefore, the farther the grating is from the laser head containing the lasing medium the smaller the lasing bandwidth.

4.4 Cavity Design

4.4.1 Introduction

To obtain laser action at the two orthogonally polarized wavelengths simultaneously, the arrangement shown in Figures 4.4.1 and 4.4.2 with a polarizing beam-splitter in the cavity, was evolved and used successfully[50]. With the beam splitter the light into two beams polarized at right angles to each other, each of the two wavelengths lases along one of the polarizations. Two types of polarizing beam splitters

were tested for this application:

1. a polarizing beam-splitting cube utilizing dielectric coatings, and
2. an air-spaced Glan-Taylor prism.

While both provided simultaneous laser action for close-lying wavelengths in the 4500 Å spectral region, it was found that each suffered some drawbacks. Both types of beam splitters are examined further below.

4.4.2 Dielectric coated polarizing Beam Splitter

The principle of this device shown in Figure 4.4.3, is that it is always possible to find an angle of incidence so that the Brewster condition for an interface between two materials of differing refractive index is satisfied. When this occurs, the reflectance for the parallel-plane (p) of polarization vanishes. Perpendicularly-polarized (s) light is partially reflected and transmitted. To increase the s-reflectance, retaining the p-transmittance at or very near unity, the two materials are then made into a multilayer stack. The layer thicknesses are quarter-wave optical thicknesses at the appropriate angle of incidence.

When the Brewster angle for normal thin-film materials is calculated, it is found to be greater than 90 degrees referred to air as the incident medium. In other words, it is beyond the critical angle for the materials. This presents a problem which is solved by building the multilayer filter into a glass prism so that the light can

be incident on the multilayer at an angle greater than critical, Figure 4.4.3.

The dielectric-interface polarizing beam-splitting cube tested and found to have an acceptance angle of up to 5 degrees and a passband extending from approximately 2245 Å to 6739 Å. It was coated to have a center wavelength at approximately 4490 Å. The entrance and both exit faces were polished to $\lambda/10$, and were also antireflex coated for 4490 Å.

Utilizing the dielectric-interface polarizing beam-splitting cube, simultaneous two-orthogonally polarized wavelength operation was readily achieved, with the flashlamp pumped Phase-R laser. Typical pulse output energies were approximately 100 mj, simultaneously at 4478.5 Å and 4500 Å with bandwidth of 5 Å.

4.4.3 Air-spaced Glan-Taylor Prism

The air-spaced Glan-Taylor Prism was also tested for use as a polarizing beam splitter in the laser cavity. Its power handling capabilities far exceed that of the dielectric-interface prism, since the medium sandwitched between the two prisms is air rather than a delicate dielectric coating. The prism is in fact comprised of two linearly birefringent calcite ($CaO^{\cdot}CO_2$) prisms separated by the air gap.

In each prism the optic axis is perpendicular to the incident beam and to lateral faces. The operation of the device may be readily understood in view of Figure 4.4.4.

This shows the air-spaced prism, its optic axis, and the incident unpolarized beam. When an unpolarized laser beam is incident upon the input face, two refracted orthogonally linearly-polarized beams are produced. The E-ray, the refracted beam whose polarization direction is parallel to the optic axis, experiences no change in index as it propagates through the prism-air-gap-prism combination.

The O-ray, the refracted beam whose polarization direction is perpendicular to the optic axis, experiences a large change in index at the calcite-air-gap interface and is thus totally internally reflected.

Use is made of both the E and O-rays to simultaneously obtain laser action on beams polarized at right angles to each other with gratings terminating the laser cavities beyond each prism. The optical arrangement is shown in Figure 4.4.1.

In the manufacture of the air-spaced prism it was only possible to polish the input face and the axial output face to within $\lambda/4$ because of the crystal structure. The lateral faces are perpendicular to the optic axis, and since calcite belongs to the hexagonal crystallographic system, attempts to polish these faces to better than $\lambda/4$ would result in hexagonal pitting, giving rise to large scattering losses.

The high losses on the lateral face meant that for geometrically identically optical arrangements the low-loss axial resonator dominated, and laser action was restricted to it. When the axial resonator was blocked however, laser

action was also obtainable in the lateral resonator.

By greatly reducing the off-axial resonator length it was possible to obtain laser action simultaneously in both resonators. Under these conditions, competition effects were clearly observed between the two resonators. However, because of the high losses associated with the lateral faces, it was found that when conditions were arranged to obtain equal energies and equal linewidths from both resonators simultaneously, the output energies were too low to be usefull.

Thus in spite of the higher power-density handling capabilities of the air-spaced prism, it was decided to abandon its use in the Lidar transmitter, in favor of the dielectric-interface prism. The air spaced beam splitter was used instead for polarization discrimination in the Lidar receiver, where a slightly higher (a few percent) loss in the transmission of the polarized component versus the other, would have no significance or impact on the backcatter measurements where only ratios of the same polarization were being measured.

It was therefore with the dielectric-coated beam splitter in the laser cavity, that the field experiments described in later sections were carried out.

4.4.4 Stability of Output

Output wavelengths were adjusted to the desired 4478.5 Å and 4500 Å by grating adjustments, and using a spectrometer

to examine outputs. The bandwidths were set to approximately 5 Å, as measured by analysis of spectrometer photographs, by appropriate geometric spacing of the gratings and polarizing beam splitters (larger spacing to obtain narrower bandwidths).

Measurements of the laser output showed no detectable swing in wavelengths or change in peak output from shot to shot. This is attributed to the case taken to ensure stability of the system in terms of cooling water temperature control, N_2 flow rates in the spark gap of the discharge circuit for the flash lamp used for pumping the dye laser, and improved mechanical stability of mirrors and the laser system as a whole. Pulse output energies were measured to be stable within $\pm$ 2.5 percent, which in any case was of no concequence to the polarization discrimination DASE scheme where purely relative measurements are required.

4.4.5 Polarization of Laser Output

To check that the laser cavity arrangement with the dielectric beam splitter gave the desired orthogonally polarized outputs, the calcite polarizing beam splitter was placed in front of the laser in the arrangement of Figure 4.4.5. The gratings were arranged to provide orthogonally polarized laser action at the two wavelengths 4478.5 Å and 4500 Å, with approximately equal amplitudes, with the two outputs orthogonally polarized.

With the spectrometer set to detect both signals in turn, with a photomultiplier on the spectrometer where output was displayed on an oscilloscope, it was found that the fraction unwanted cross polarization in the outgoing polarized components was less than 1 part in 10^5, the limits of accuracy of the measuring system. Thus, to that extent, the outputs of the polarizing beam splitter cavity laser system could be considered to be effectively properly orthogonally polarized.

4.5 Laser Beam Transmitted in the Atmosphere

To guide the laser beam from the laser output to emerge colinearly with the axis of the Lidar receiver, the mirror arrangement of Figures 4.5.1 and 4.5.3 was used. The mirrors were front surface aluminum mirrors.

In the context of the Lidar discrimination scheme, it is important to determine the degree of undesirable cross polarization that might occur through the use of such mirrors. It is therefore worthwhile to first examine the depolarization that can occur from planar aluminum mirrors. The arrangement used for this purpose is shown in Figure 4.5.2.

The direction of polarization of the reflection of a 6328 Å He-Ne linearly polarized laser beam, with respect to the plane of incidence was observed as a function of the polarization of the incident beam and its relative orientation with respect to the reflecting mirror. It was

found that the minimum depolarization occured when the direction of polarization was parallel or perpendicular to the plane of incidence. The depolarization under these circumstances was found to be too small to be detected, in contrast to other relative inclinations of the plane of polarization and the plane of reflection where depolarizations as high as 2-3 percent were detected. Accordingly the orientations of the mirrors used to deflect the beams were arranged to comply with the above requirements for minimum depolarization by ensuring appropriate orientations of their planes of incidence to the polarizations of the two outgoing wavelengths.

4.6 Conclusion

Through the use of a dielectric coated intra-cavity polarizing beam splitter, orthogonally polarized co-linear laser beams are obtained at two close-lying laser wavelengths from a flush-lamp pumped dye laser. The two wavelengths are tuned by means of gratings to 4478.5 and 4500 Å respectively. By appropriate geometric spacing of the gratings and of the laser aperture, linewidths were restriced to approximately 5 Å.

Temperature and mechanical stabilities attained ensured that pulse to pulse outputs were stable as far as wavelength was concerned. Small variations measured in output pulse energy are of no consequence to the polarization discrimiation scheme where only relative measurements are

required. Output measurements showed polarization of output in the desired directions to be better than 1 in 10^5 which, as is discussed in the error analysis section is more than adequate for use in the polarization discrimination scheme. Directing the output beam to be co-linear with the receiver axis is achieved though the use of mirrors which are found to produce no measurable depolarizations provided that they are properly oriented.

In the receiver, the light is gathered by a Fresnel lens, focussed and collimated into a Glan-Taylor prism, which is effectively used to separate the two orthogonally polarized backscattered signals. These are then directed onto photo-multipliers for detection and subsequent display. The Lidar transmitter and receiver systems thus essentially achieve what is required of them for use in a polarization discrimination scheme. It remains to determine, in the experiments discussed in the next Chapter whether external factors, related to atmospheric scattering properties permit practical implementation of the scheme.

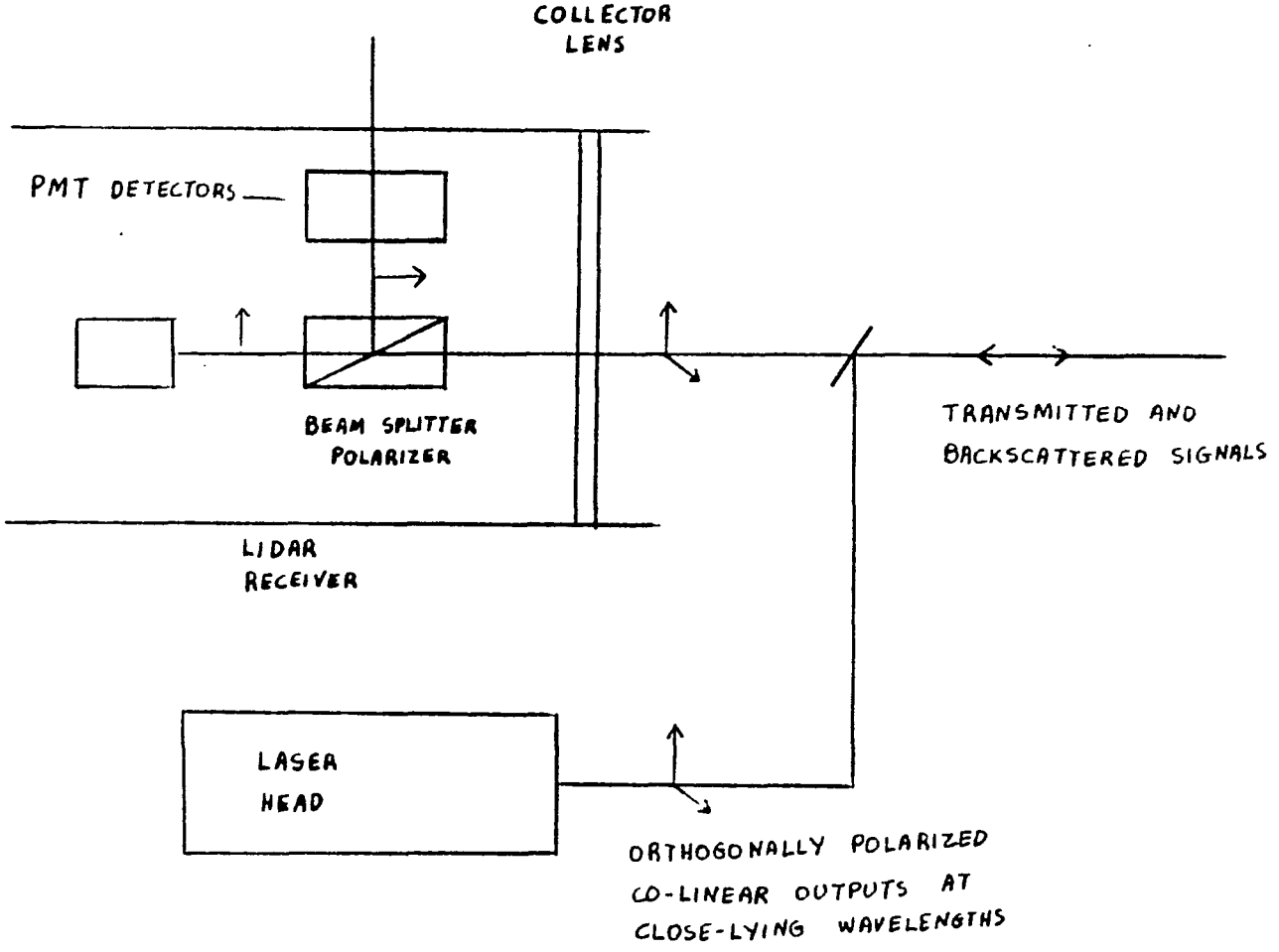

FIGURE 4.1.1 Schematic for DASE Lidar system utilizing polarization discrimination.

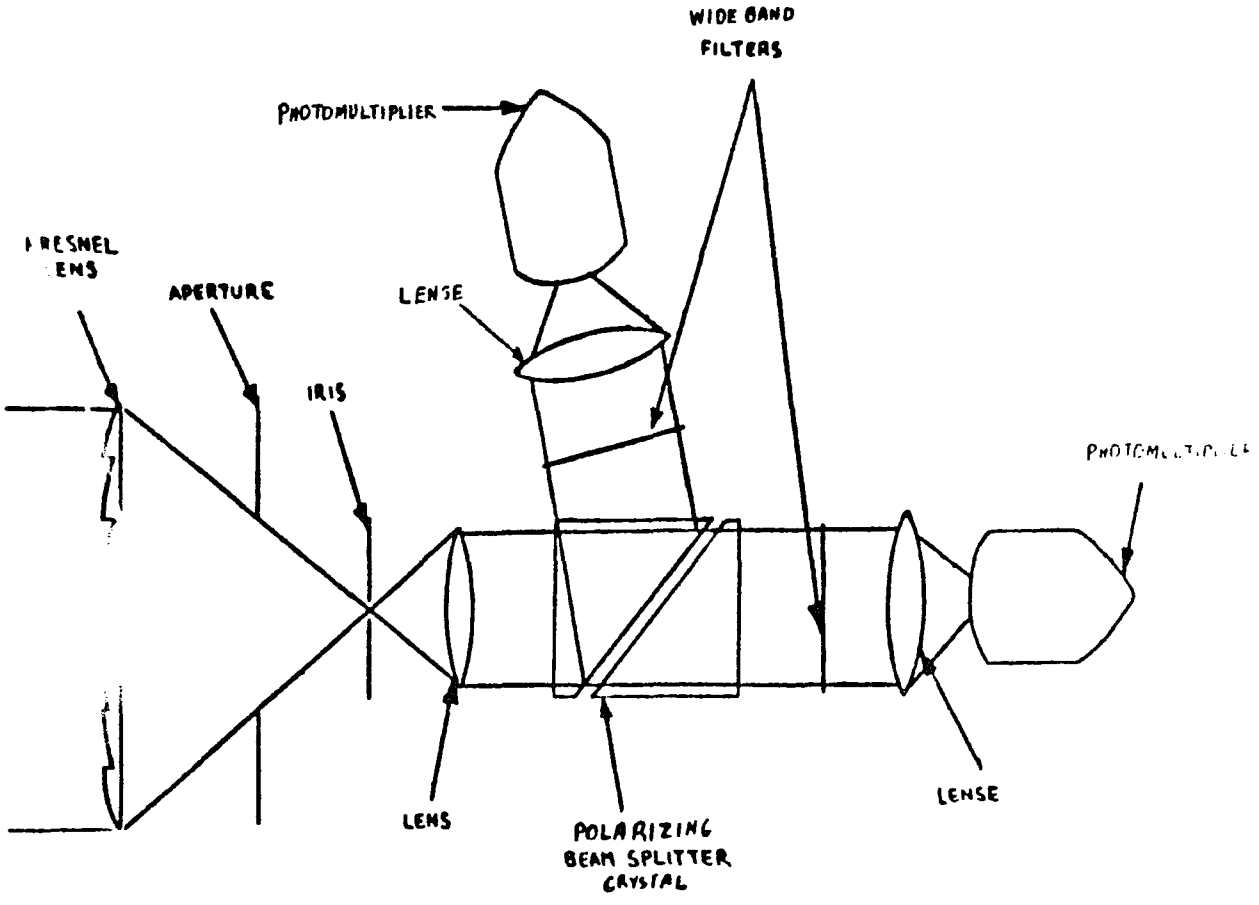

FIGURE 4.2.1 The optical receiver system for polarization discrimination.

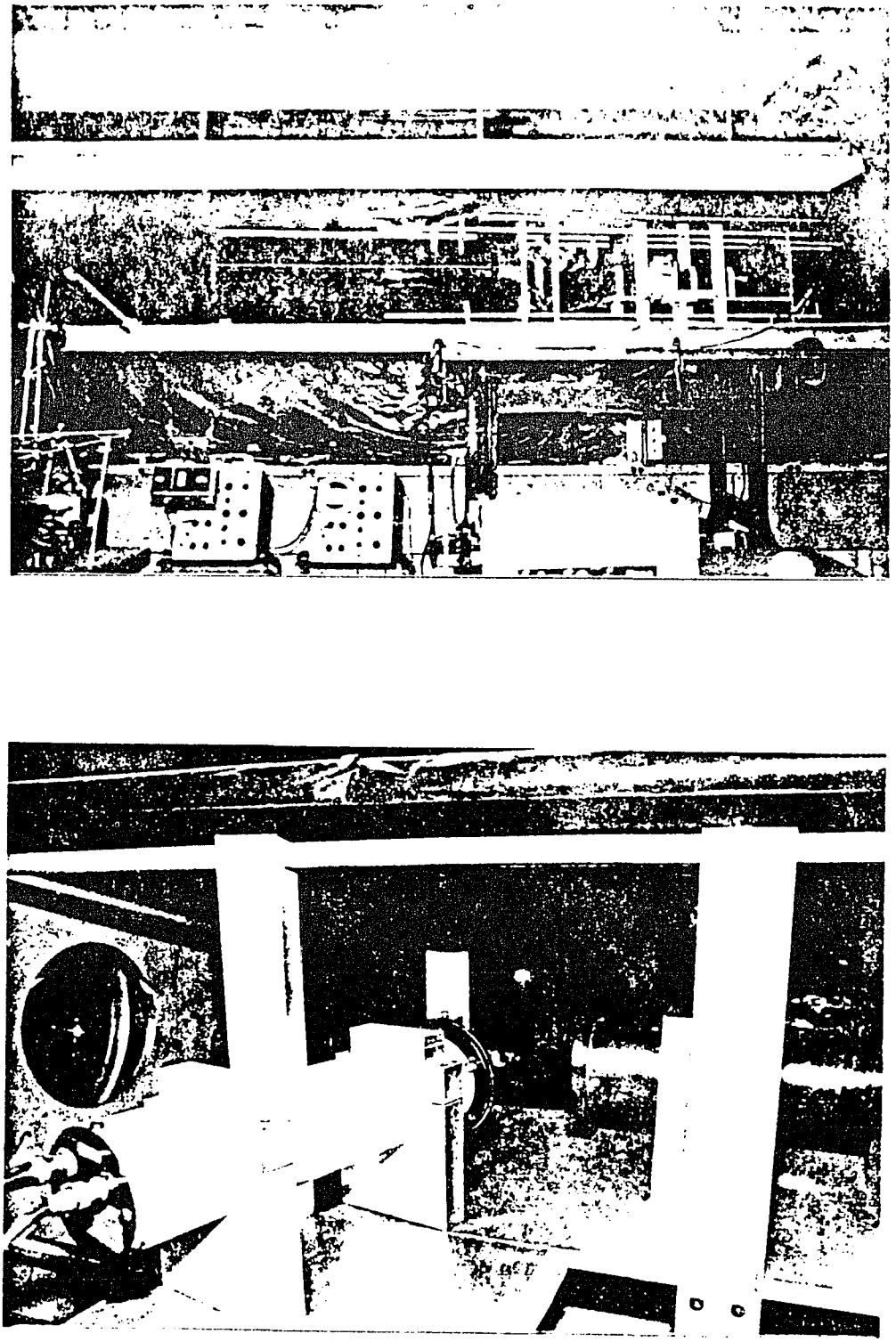

FIGURE 4.2.1a Photographs of the optical receiver.

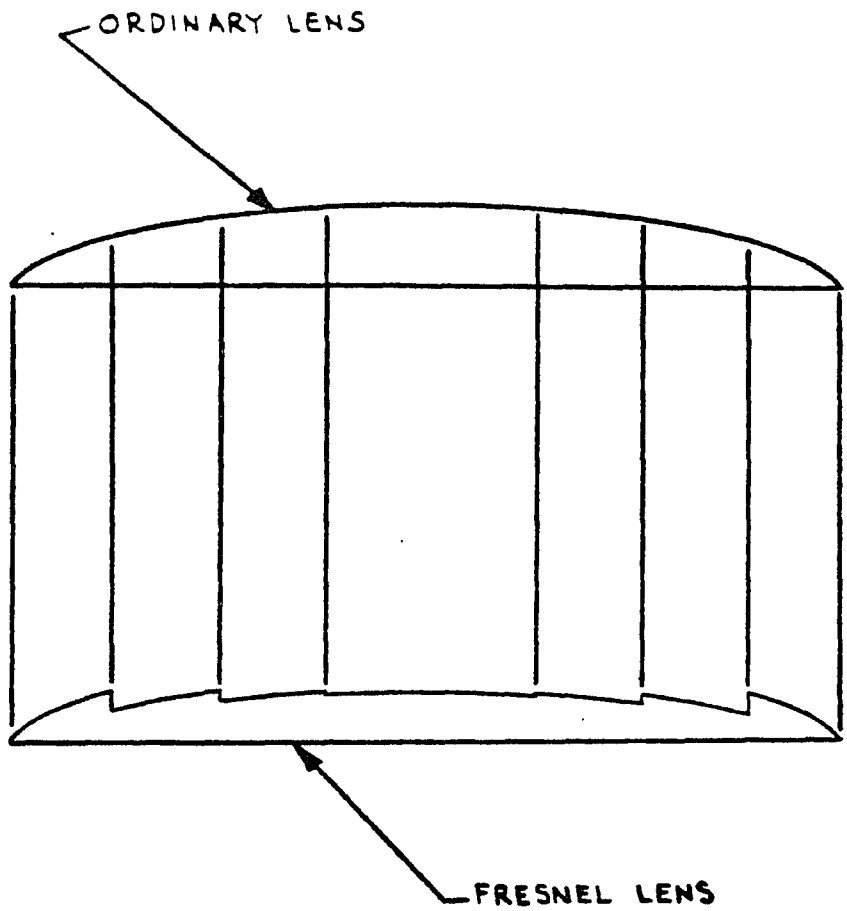

FIGURE 4.2.2 Fresnel Lens.

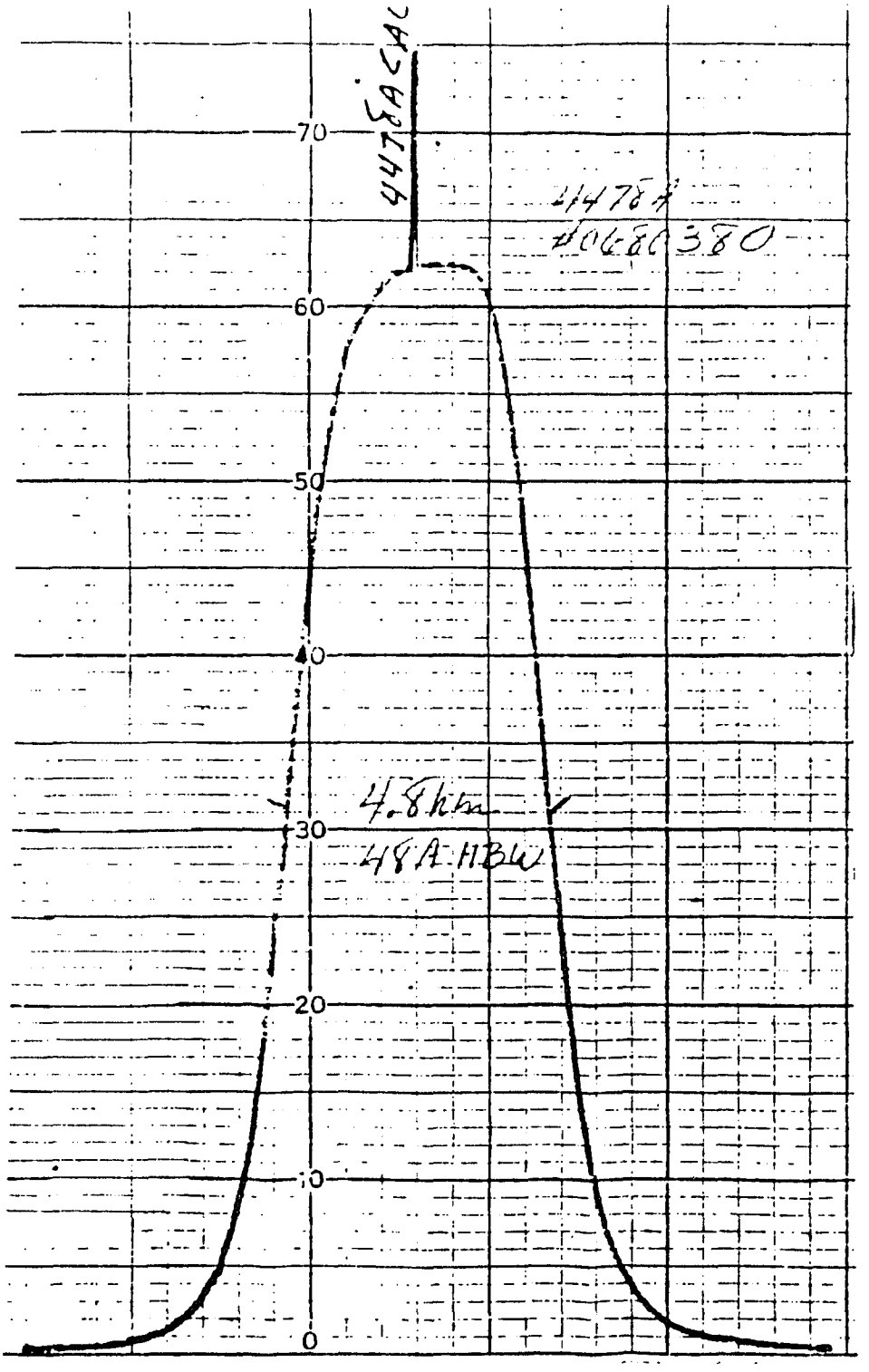

FIGURE 4.2.3a Transmission characteristic for the broad band filter centered at 4478.5 Å.

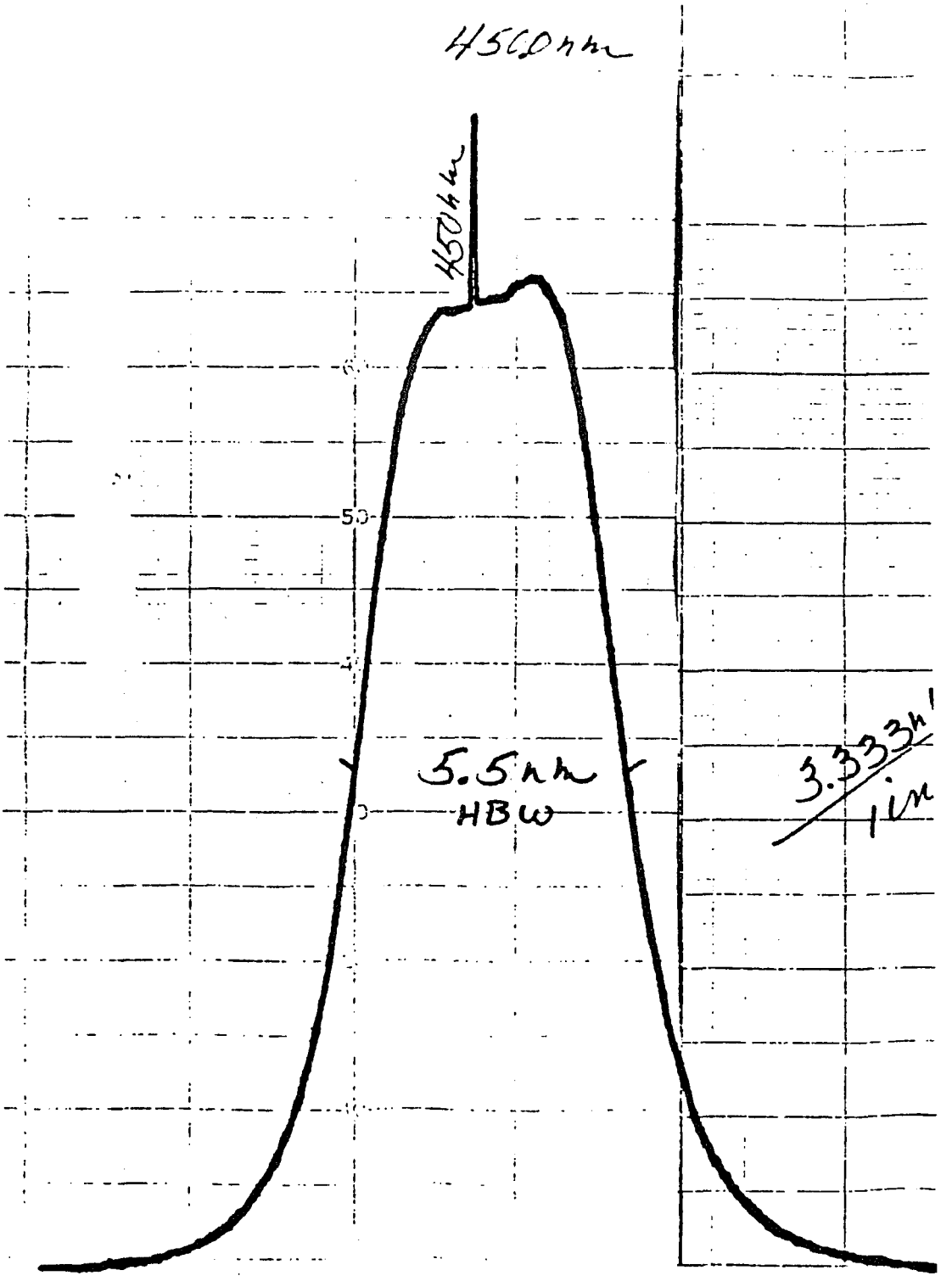

FIGURE 4.2.3b Transmission characteristic for the broad band filter centered at 4500 A.

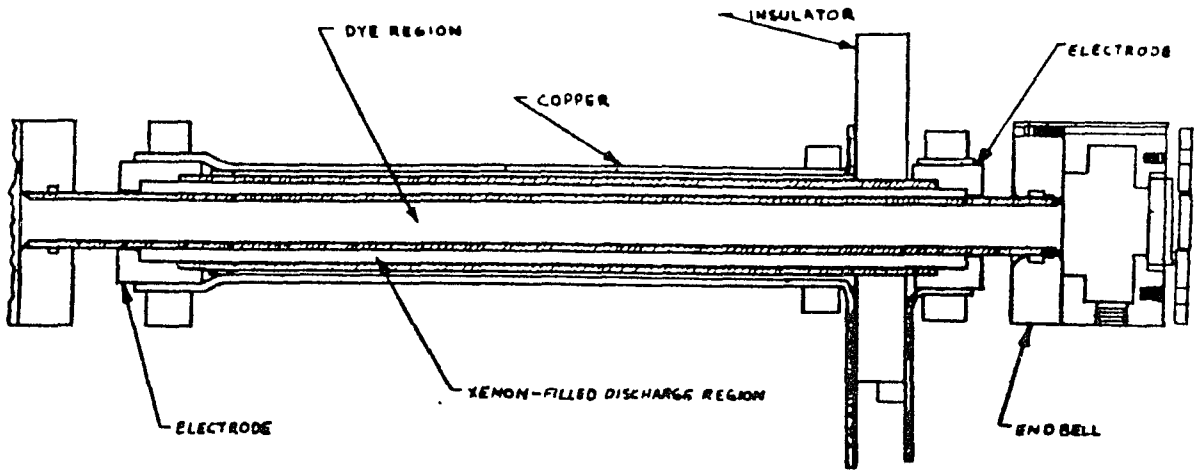

FIGURE 4.3.1 Schematic of flashlamp pumped dye laser.

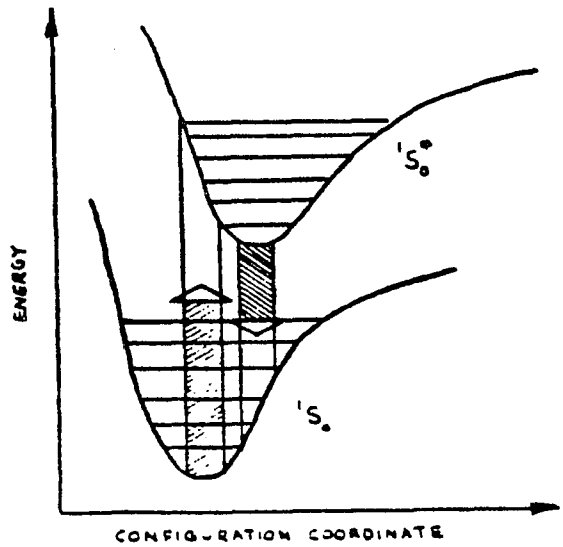

FIGURE 4.3.2 Energy level structure for typical dye molecule.

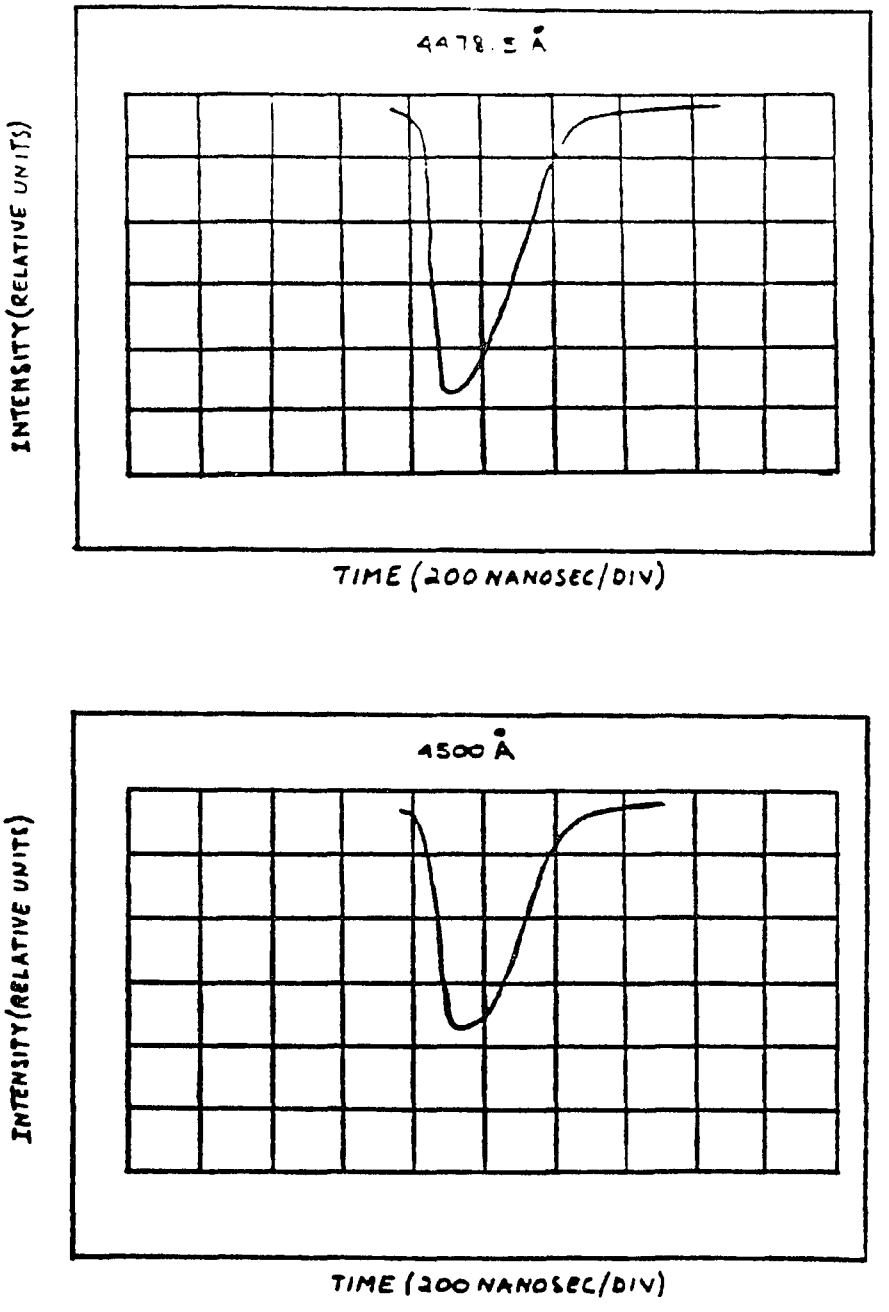

FIGURE 4.3.3 Typical flashlamp-pumped dye-laser output pulse.

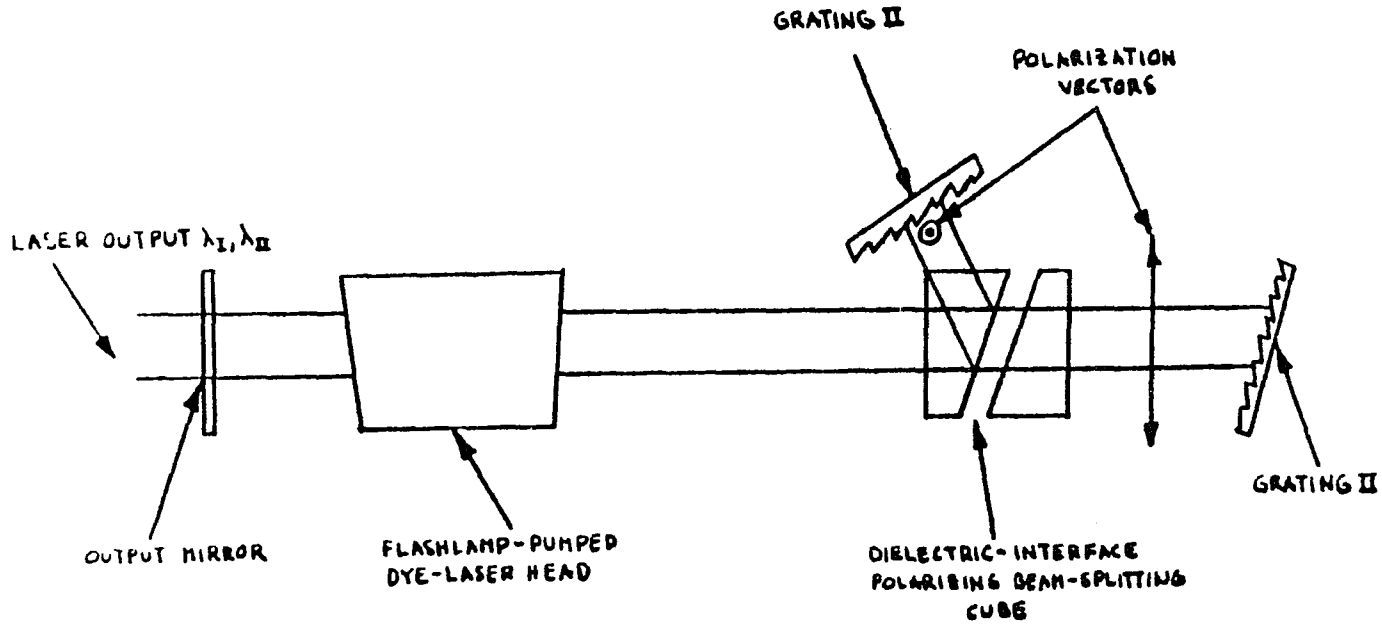

FIGURE 4.4.1 Optical arrangement for simultaneous two orthogonally polarized wavelength output.

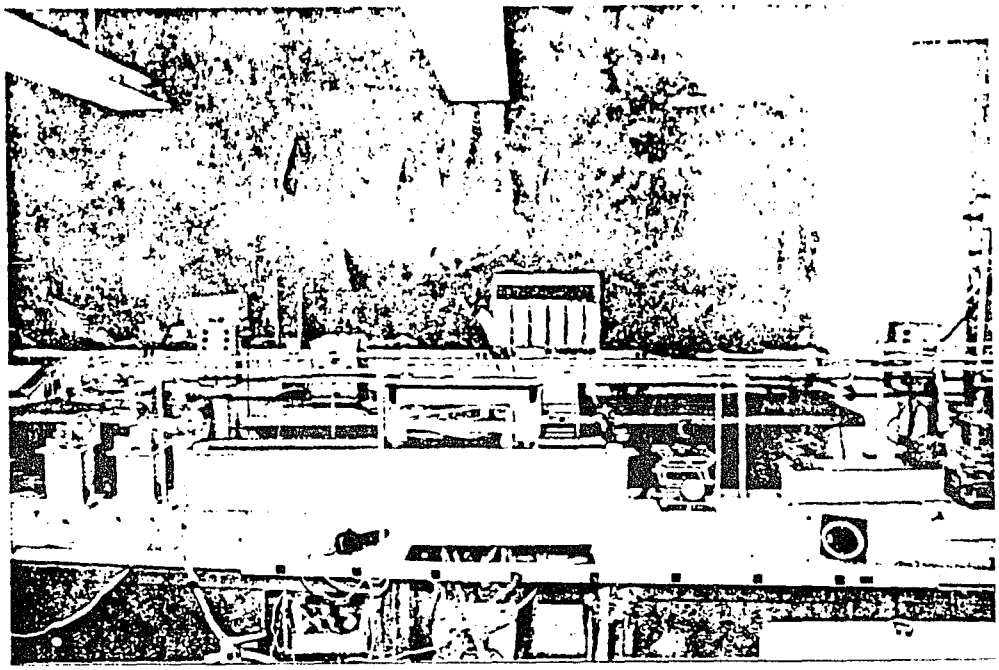

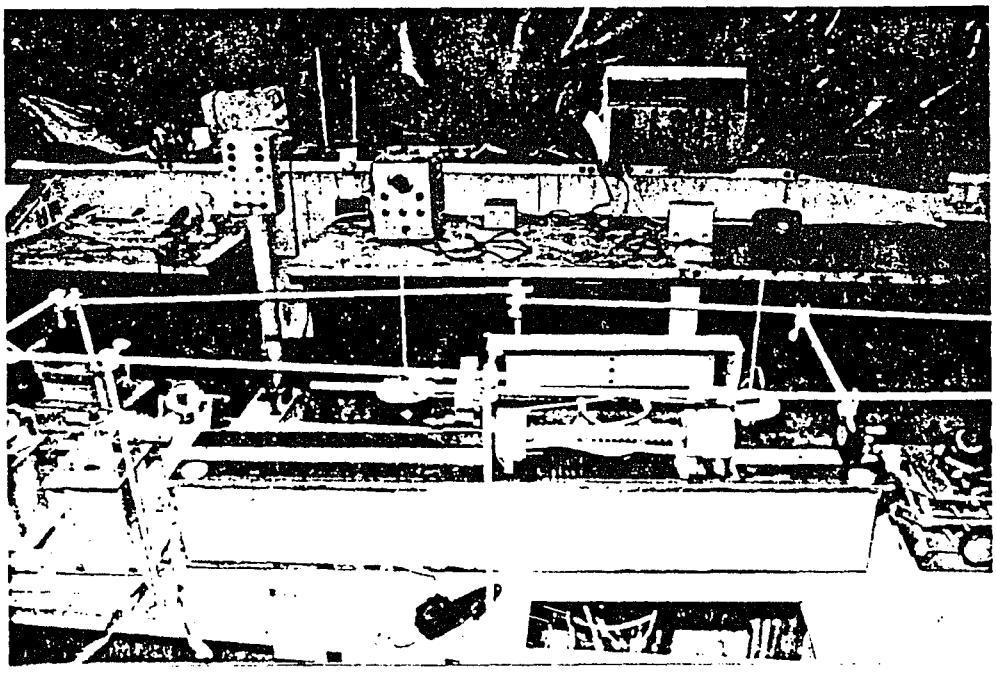

FIGURE 4.4.2 Photographs of the laser head and the cavity.

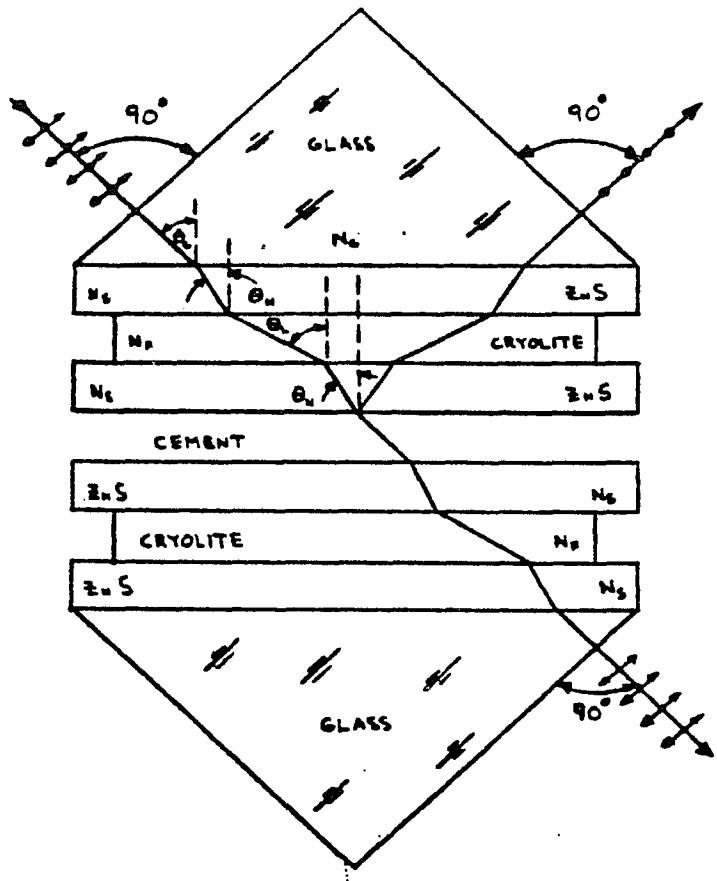

FIGURE 4.4.3 Dielecric-interface polarizing beam splitter.

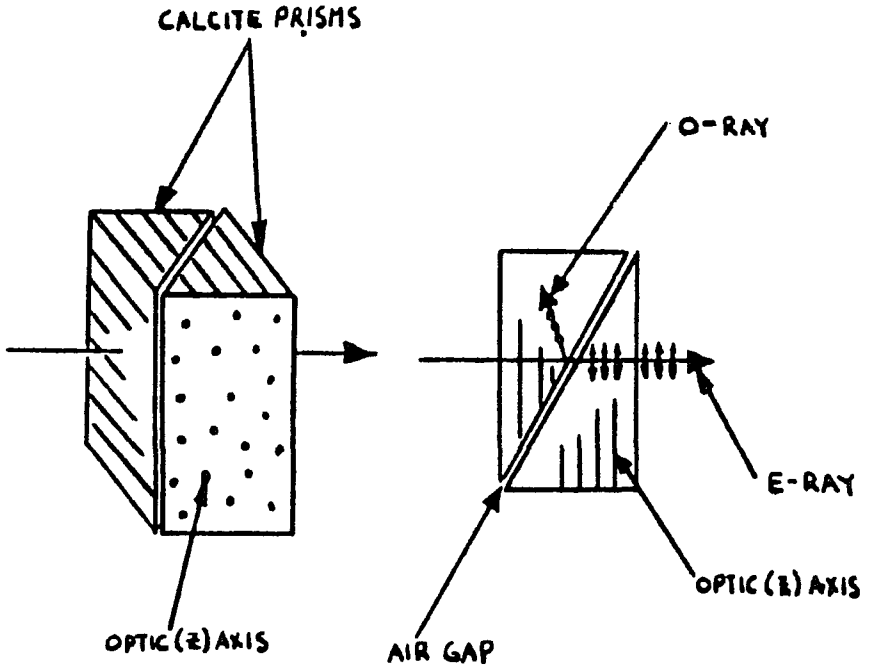

FIGURE 4.4.4 Air-spaced Glan-Taylor beam splitter polarizer.

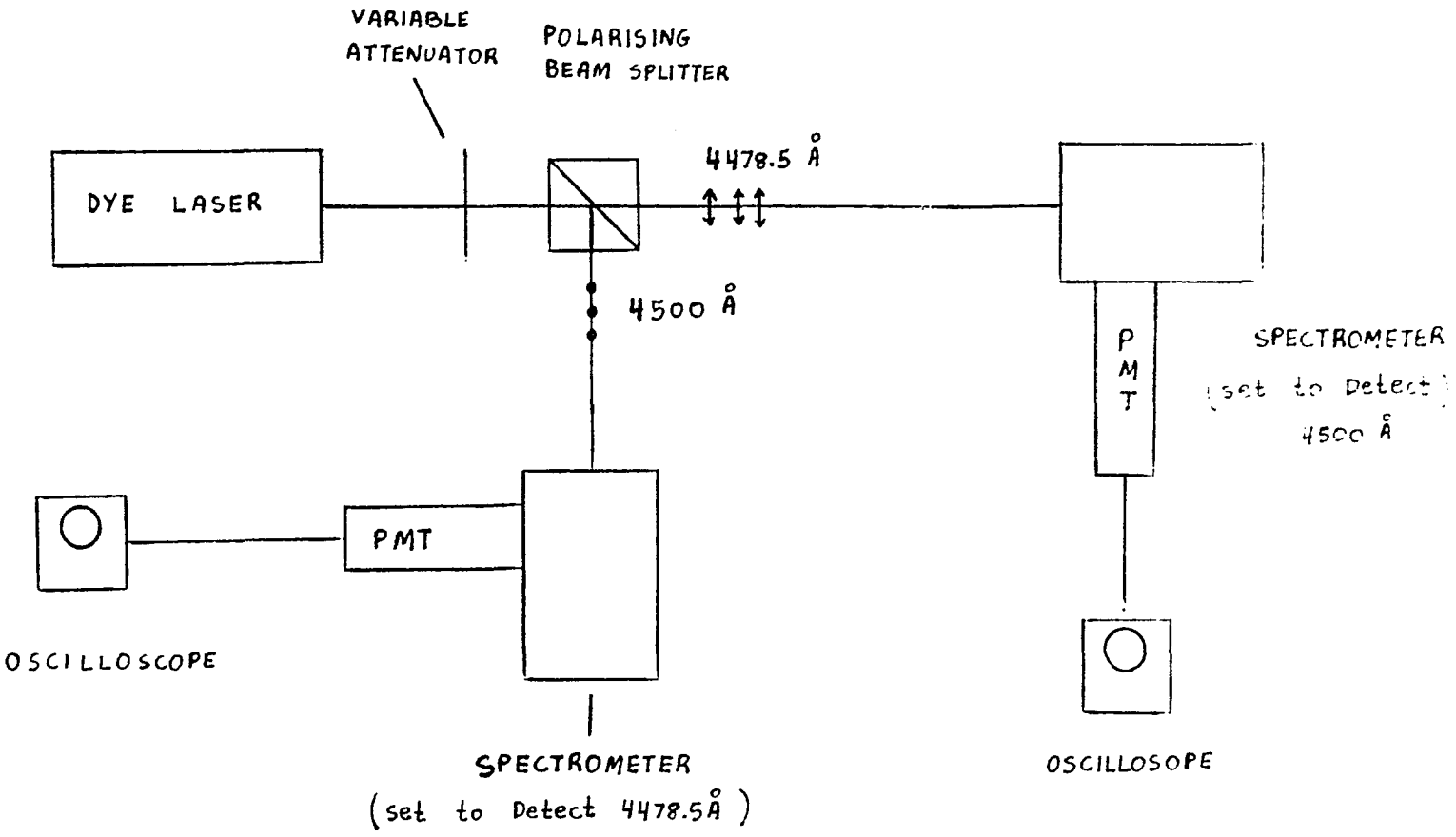

FIGURE 4.4.5 Experimental arrangement for testig the polarization of the laser outputs.

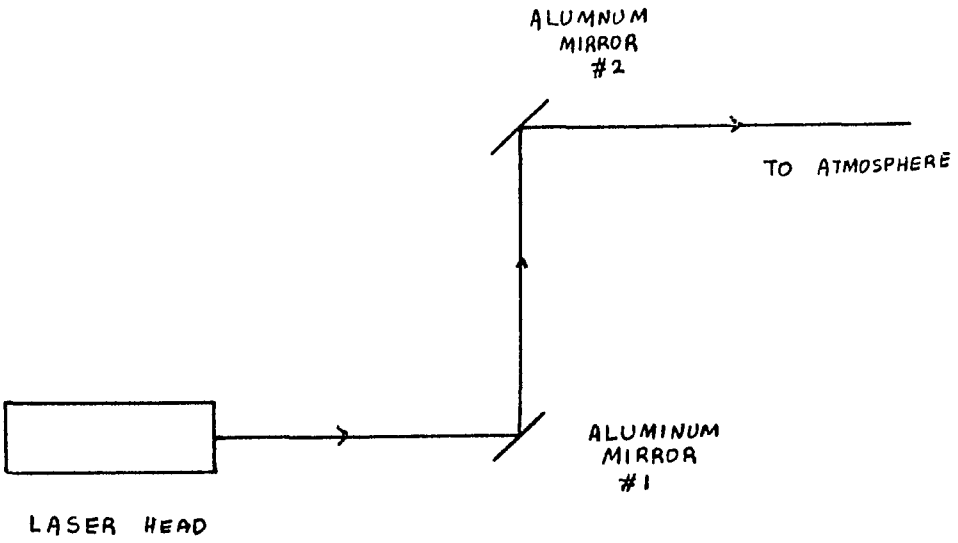

FIGURE 4.5.1 Aluminum mirror arrangement to ensure minimum depolarization.

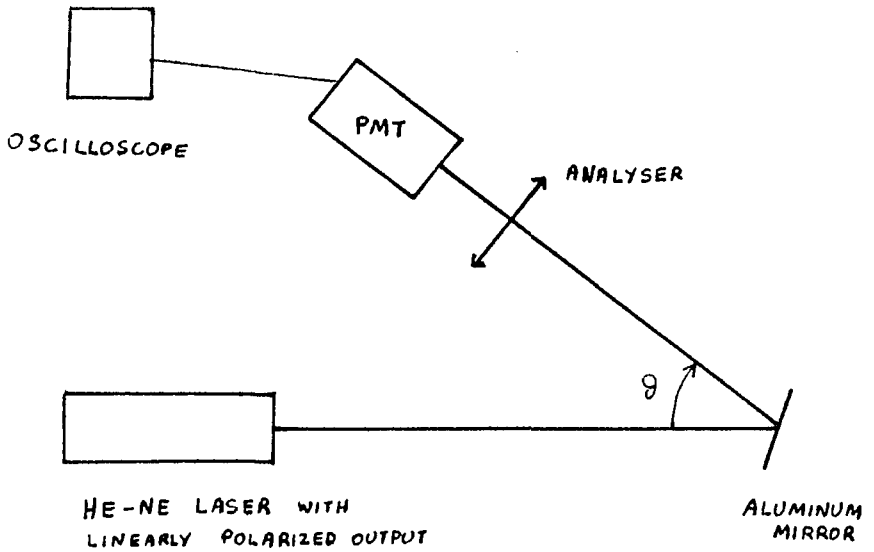

FIGURE 4.5.2 Experimental arrangement for testing depolarization properties in mirrors.

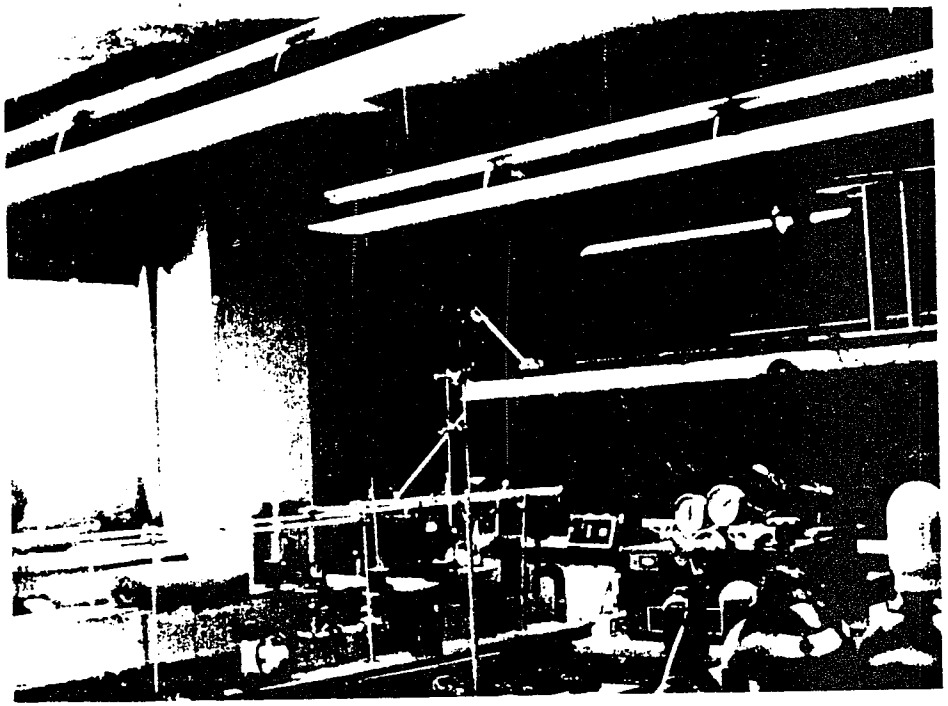

FIGURE 4.5.3 Photooraph of the laser head and the aluminum mirrors guiding the output beam through the window to the atmosphere.

CHAPTER 5

EXPERIMENTAL RESULTS

5.1 Introduction

To develop and test the viability of the polarization discrimination DASE Lidar systems both laboratory tests and field tests were carried out, culminating in the application of the technique to the Lidar measurement of atmospheric NO_2 in the field tests from the CCNY laboratory window overlooking the East Side of upper Manhattan.

The initial laboratory tests concerned the examination of particulate scattering process (in smoke) and depolarization results from them.

These were followed by field tests with the Lidar system to examine the effects of depolarization due to atmospheric scattering that would result from Lidar returns at typical atmospheric conditions and ranges that would be used with the Lidar technique.

These experiments which included examination of backscattering as a function of the field of view of the Lidar receiver, were also designed to examine the scattering and depolarization picture developed in Chapter 3, which relates depolarization to single step 180^{o} backscatter from asymmetrical particles plus two-step particulate scattering processes from any particles. The results obtained confirm this picture. Furthermore they show that when the receiver

field of view is reduced by the same order as the outgoing Lidar beam divergence, the depolarization in the backscattered signals is so small, that, taken in conjunction with the error analysis of Chapter 3, section 3.4 undesirable depolarization effects do not seriously affect the accuracy of the system.

Finally atmospheric measurements were carried out using the complete polarization discrimination DASE Lidar system through the CCNY laboratory windows, and readings of NO_2 pollution concentrations at ranges 1-2 Km were obtained, demonstrating the viability of the system.

5.2 Depolarization due to Mie Scattering - Laboratory Experiments with Smoke

5.2.1 Introduction

Most of the theoretical results for depolarization due to scattering by particles have been derived assuming single scattering mechanism and particles with specific geometric shape i.e. spherical, cylindrical, particles with rotational symmetry e.t.c. The above approximations simplify the problem though, as is discussed in Chapter 3, it is reasonable to believe that depolarization in th atmosphere is also primarily related to multiple Mie scattering processes.

It was therefore important, before designing a system utilizing polarization discrimination, to test, in laboratory experiments, the effects of particulate

scattering on depolarization, and relate these to the theorical picture being developed, and use the results to define Lidar system parameters that would result in a minimum depolarization in received signal.

For these purposes, sets of laboratory experiments were performed. In these, smoke (obtained from cigarettes) was introduced into the test chamber to serve as the scattering medium.

5.2.2 The experimental arrangement

Figure 5.2.1 shows the arrangement used to measure the depolarization of linearly polarized light scattered by smoke particles. The values of depolarization were taken for various angles of scattering, incident polarization, and optical thicknesses.

The experimental arrangement was assembled on a horizontal table. Figure 5.2.2 is a photograph showing the system. The light source was a He-Ne laser, .5 mW output power, positioned to give a beam parallel to the plane of the table (Horizontal). The laser beam passed through a variable polarizer. The polarizer was a Glan-Taylor polarizing prism mounted on a rotary positioning table. The positioning table was perpendicular to the beam and was capable of measuring the angle of rotation with an accuracy of .1 degree. The angular positioner was carefully adjusted so that the 0 degree of its scale corresponded to a Horizontally polarized laser beam as the output of the

polarizer.

The output beam from the polarizer passed through a cylindrical transparent glass cell, 20 inches long and 4 inches in diameter, positioned to be coaxial to the laser beam. The cell had two flat windows parallel to each other and at an angle 80 degrees approximately, with respect to the cylinder axis. That orientation was necessary in order to direct the component of the incident beam reflected from the windows, away from the region where scattering was measured. The cell had on the top of the cylindrical surface, near the windows, two openings with stopcocks. Through them, smoke was blown to fill the cell, solvent was introduced to wash the cell and air circulated to dry the washed cell or remove smoke in order to reduce its density.

The output from the cell was collected by the lens of a JEA He-Ne optical power meter, which measured the attenuation, due to the windows of the cell plus that due to the smoke.

The scattered light was collected by an optical receiver at various angles of scattering. The receiving system was designed to collect scattered light directed horizontally. According to that design the plane of scattering was the horizontal plane through the laser beam.The components of the optical receiver were a thin tube, an analyser, a He-Ne filter and a photomultiplier with photometer. The thin tube was a straight, long cylindrical tube. Its dimensions were 40 cm in length and 7 mm in diameter. It was coated with

light absorbing velvet black paint, to absorb the light hitting the walls of the tube. The axis of the tube corresponded to the propagation direction of the scattered light and its projection, drawn on the table, together with the projection of the laser beam axis, was the angle of scattering ϑ. The tube selected was small, allowing only light scattered in direction parallel to the axis of the tube, or in the paraxial region to pass. From the available tubes, an optimum size for the diameter was found to be 7 mm for a tube length 40 cm. Further reduction of the diameter, could result in stronger diffraction effects and consequently further depolarization of the received scattered light, as well as significant loss of signal power. The accuracy in measuring the angle of scattering was within $\pm$.5 degrees, due to the fact that the diameter of the tube was not infinitely small.

The analyzer was a linear polarizer, mounted in the rotatable part of a mount. The polarizer was an HN-32 sheet, made by Polaroid Corporation. That polarizer, for the He-Ne laser frequency (6328 $\mathring{A}$), gives a principal transmittance k_1 approximately equal to .68 and a principal transmittance ratio k_1/k_2 approximately equal to 3.4×10^4. Those values though lower than for a birefringence polarizer, are acceptable for laboratory (Dark-room) conditions with good SNR, considering the sensitivity of the available photo-multiplier and the lowest expected level of depolarization ratio in the experiment. Figure 5.2.3 and Table 5.2.1 show

the wavelength variation of the principal transmittances k_1 and k_2 for the HN-32 sheet polarizer, assuming that no reflection losses occur. The mount of the analyser had a circular scale engraved 0-360 degrees, in one degree increments with each 10 degrees numbered. The zero of the scale corresponded to the principal axis of the polarizer. The plane of the polarizer was perpendicular to the axis of the thin tube and therefore vertical. An index was positioned on the fixed part of the mount. The index was pointed at the zero of the circular scale when the principal axis of the polarizer was perpendicular to the horizontal plane of scattering. With the above design, the analyzer could detect the orientation of the electric field components of the scattered light, with respect to the horizontal plane of scattering.

After the analyzer, the scattered light, was passed through a He-Ne filter, and collected by a Q4283 SA 25 Centronic Photomultiplier. Figure 5.2.4 gives the spectral response of the filter. The Photomultiplier characteristics are shown in Figures 5.2.5a, 5.2.5b and Table 5.2.2. A laboratory photometer, model 110 made by Pacific Photometric Instruments, was connected to the Photomultiplier. The Photometer supplied the High Voltage for the photomultiplier and measured its output current that was proportional to the power of the analysed scattered light. Using the above receiving system, the polarization states of the scattered light were determined.

5.2.3 Laboratory measurements of Depolarization by Smoke Particles

In order to investigate the dependance of depolarization on the polarization angle of the incident linearly polarized light and the angle of scattering ϑ, several sets of measurements were carried out.

The incident polarization angle φ_i (angle of the incident electric vector with respect to the horizontal plane of scattering) varried between 0 degrees (Horizontally polarized light) and 90 degrees (Vertically polarized light), in steps of 10 degrees, by rotating the variable polarizer. Figure 5.2.6a shows the orientation of the incident linearly polarized light.

The polarized light first passed through the cell without smoke, to measure the attenuation due to the windows. The optical power meter was used for that purpose. No measurable depolarization due to the windows was observed for the light transmitted through the cell. Also the light scattered from the windows was found to be negligible. Then cigarette smoke, the scattering medium, was blown into the cleaned and dried cell. The cell with the smoke was well shaken, to assure uniform smoke distribution and a measurement of the optical thickness was taken, using the optical power meter. The optical thickness of the empty cell was subtracted from the optical thickness of the cell with smoke, in order to calculate the optical thickness of the smoke only. To change the optical thickness, the smoke

density was adjusted, introducing more smoke or expelling it by air circulation through the cell. Then the cell was shaken again and the optical thickness was measured. That procedure was repeated until the desired optical thickness was achieved. The optical thickness τ of the smoke for the depolarization measurements was set to 5, that is typical for an atmospheric path 1 km. A problem in keeping constant optical thickness, during the measurements, was the decrease of the density of the smoke with the time, due to deposit of smoke particles on the walls of the cell. Considering as an acceptable error a 5% for δ, due to the change of τ with time, it was found (Figure 5.3.9b) that, for $\tau=5$ the corresponding change in δ was 15%. Dividing the measured time necessary for that change, by the average time (approximately 15 sec) of a measurement, it was found that a readjustement of the smoke density was necessary every 3 measurements, in order to maintain approximately the same scattering conditions. Furthermore to avoid error in the optical thickness measurements, due to the smoke deposit on the windows of the cell, cleaning of the cell was necessary after a few measurements. For those reasons, the smoke was used for a maximum of 3 measurements. Then the cell was cleaned, dried and fresh smoke was blown and adjusted to the proper density. The cell after shaking was always left at the same position marked on its base.

The angle of scattering ϑ varied between 180 degrees and 90 degrees, in steps of 10 degrees, by moving the optical

receiver to the proper positions, marked on the horizontal table.

From the experimental set up and the previous discussion it is clear that the time necessary to change φ_i, by rotating the polarizer mount, was much less than the time required for change of ϑ, by moving and adjusting the receiver. Also the time available for each measurement was relatively small. For those reasons each set of measurements was taken with constant ϑ and φ_i varying between 0 degrees and 90 degrees. After each set of measurements a change of by 10 degrees followed, until the whole range of ϑ (180 deg. to 90 deg.) was covered in steps of 10 degrees.

5.2.3.1 Results

The scattered signal was found, as might be, expected, from the discussion of Chapter 3, to be elliptically polarized. For each φ_i and ϑ, by rotating the analyser, the maximum $I_{s,max}$ and the minimum $I_{s,min}$ of the intensity of the scattered light passed through the analyser were measured, as well as the angle $\varphi_{s,max}$, where the maximum was found, with respect to the plane of scattering. The maximum and minimum corresponded to the major and minor semiaxes of the polarization ellipse respectively, while the angle $\varphi_{s,max}$ indicated the orientation of the ellipse with respect to the plane of scattering.

Figure 5.2.6b shows the parameters of the polarization ellipse measured in the experiment. The ratio $I_{s,min}/I_{s,max}$

is equal to the square of the ellipticity (Equation 3.2.6). In general, the orientation of the major semiaxis of the polarization ellipse ($\varphi_{s,max}$), with respect to the plane of scattering,is not the same as the orientation of the incident field (φ_i). The difference $\Psi = \varphi_{s,max} - \varphi_i$, was calculated for each measurement. The depolarization ratio δ, was calculated using Equation 3.2.20.

Figures 5.2.7a, 5.2.7b and 5.2.7c show the values of depolarization for difrerent ϑ and φ_i.

The orientation of the polarization ellipse , with respect to the plane of scattering is shown in Figures 5.2.8a, 5.2.8b and 5.2.8c. The straight line corresponds to the case of specular reflection, from a mirror, introduced for the purpose of comparison. A good quality aluminum mirror was used for reflection measurements. The Depolarization due to reflection was found negligible compared to the case of scattering by smoke particles. For that reason it is not included in Figures 5.2.7.

5.2.4 Conclusions

Two following main effects were observed from the preceeding laboratory experiments.

1. For a given scattering angle the minimum depolarizations occur when incident polarization is either parallel or perpendicular to the scattering plane. The minimum depolarizations are generally small δ=2-5%. The maximum

depolarizations , typically δ=60% occurs when the incident polarization approximately is 45^{o} with respect to the scattering plane. (Figures 5.2.7). These results are consistent with those expected in Chapter 3, for scattering by large particles, which can be approximated to planar specular scattering.

2. The orientation of the polarization of the scattered field relative to the incident polarization varies as a function of the incident polarization angle φ_i(relative to the scatter plane) and the scattering angle ϑ shown in Figures 5.2.8. When the incident field direction is parallel or perpendicular to the scatter plane (φ_i=0 or φ_i=90^{o} respectively), the orientation of the major polarization axis of the scattered radiation is parallel to that of the incident. This has important practical implications for the Lidar polarization discrimination scheme, since it means that a backscattered signal will have its major polarization axis aligned with that of the outgoing laser beam. (Note that the variations for other φ_i values (Figures 5.2.8) are variations about the 45^{o} line which is equivalent line for specular reflections. Since our smoke particles are large particles, these results are again consistent with the picture developed in Chapter 3, approximating large particles to planar specular reflectors at the appropriate orientations with respect to the scattering

plane. Thus it can be concluded that backscattering by large particles, for incident polarization parallel or perpendicular to the plane of scattering, will generally be in accordance with the picture developed in Chapter 3, approximating them to specular reflectors.

3. Experiments were also carried out relating extent of depolarization to optical thickness of scattering medium for $\varphi_i=0^o$ and 90^o and scattering angles ϑ close to 180^o backscatter ($\vartheta=180^o$), since it was physically impractical to obtain 180^o exactly. The extent of depolarization measured (Figures 5.2.9), which was smaller for angles close to 180^o backscatter, for $\varphi_i=0$ or 90^o, varied linearly with optical thickness for small optical thicknesses. This is expected since it is reasonable that the amount of depolarization varies with the number of scatterers, which in turn varies as optical thickness (for small values.

5.3 Depolarization in Atmospheric Backscattered Lidar Signals and Receiver field of view.

To examine the effects of depolarization due to atmospheric backscatter that result from Lidar returns at typical atmospheric conditions, field tests were carried out from the CCNY laboratory window using the polarization discrimination DASE Lidar system.

As discussed in Chapter 3, it is expected that there are

two main sources of depolarization in signals backscattered to the Lidar receiver. The first of these is the depolarization of $\vartheta = 180^{o}$ single step backscattered radiation from particles, (Figure 3.3.3) without rotational symmetry about the backscatter direction, and where the wavelength λ is not much smaller than ρ, the radius of the particle scattering surface. In that case the backscattered component from the assymetrical particles would be depolarized.

In this single step process, provided the receiver field of view (acceptance angle) is larger than the outgoing Lidar beam divergence, the depolarized backscattered signal should not vary with increasing receiver field of view.

The second depolarizing scattering process expected is that due to multi-step scattering, Figure 3.3.4 from any particles, where as expected theoretically, this component of the return signal is also unpolarized. In practice, it is expected that at normal visibility conditions encountered (i.e. greater than 5 Km) it is only two step process that will be responsible, because of the small scattering cross-sections making 3 step process, relatively improbable.

As can be seen from Figure 3.3.5a and 3.3.5b, the depolarized signal due to multiple scattering can be expected to increase with receiver field of view. From simple geometric arguments, the depolarized backscatter due to this process can be expected to be proportional to the area of the scattering plane being, viewed, or for small angles, to the square of the field of view (or acceptance

angle). Obviously this argument can hold true only for small acceptance angles both for simple geometric reasons, as well as the following reason: as the field of view increases, the dependance of intensity on the square of the distance (square law effects) will start to dominate and reduce the backscatter intensity.

Thus, experiments which examine intensity of depolarized backscatter signal as a function of receiver field of view, should show the sum of the polarized signals due to the two effects. This should be a sum of a constant amount for the first depolarization effect due to a 180^{o} single step backscatter from assymetric particles plus an amount which varies monotonically with the receiver field of view (acceptance angle), due to two step backscatter from any particles. In fact, as discussed above, simple geometric considerations lead one to excpect square law variation of intensity of depolarized signal with respect to receiver field of view for the second effect, for small acceptance angles.

To examine these effects in the case of atmospheric backscatter, the Lidar system was operated in a series of tests at a wavelength of 4500 $\mathring{A}$. The transmitted signal was sent out at one polarization and the received signal deteced at both the same polarization (for reference) and the cross polarization, to observe the depolarization effects due to the atmospheric backscatter, as function of the field of view of the Lidar receiver.

The field of view of the receiver was varied by means of a variable aperture iris at the focal point of the Fresnel lens collector. The aperture of the iris could be varied from 1 cm down to zero.

To proceed with the backscatter experiment it was first necessary to determine the Lidar transmitter beam divergence and the Lidar receiver field of view. The Lidar beam divergence angle was determined in the laboratory with simple geometric measurements to be approximately 1 miliradian.

To determine the receiver field of view, as a function of iris diameter, a Helium-Neon laser was mounted in front of the telescope and its inclination varied and measured with respect to the Lidar receiver axis to determine the maximum acceptance angle for different iris apertures. Figure 5.3.1 shows the variation of field of view with iris aperture.

The Lidar returns obtained for different aperture sizes were of the type shown in Figures 5.3.2a, and 5.3.2b, which were obtained on a relatively clear spring day. Returns at that time were very steady, giving less than 2 percent variation from shot to shot for the same aperture setting. The parallel and cross polarized returns were obtained simultaneously for both the parallel and cross polarized returns.

The results of these series of tests at 4500 Å is plotted in Figure 5.3.3a showing the depolarization δ from

signal backscattered from a distance of approximately 1 Km as a function of the receiver field of view. Below 1 miliradian setting, the signal decreased rapidly as the receiver aperture decreased below the divergence of the outgoing beam.

To further analyze the results, they are shown in Figure 5.3.3b plotted on log-log coordinates. It can be seen that up to a field of view of 6 miliradians, the depolarized signal increases approximately as the square of the field of view (receiver acceptance angle). Beyond that, the depolarized signal ceases to increases as rapidly. These results are in conformity with the simple geometrical picture evolved in Chapter 3, and reiterated in this section, explaining the depolarization as the sum of a single step $\vartheta = 180^{o}$ backscatter process plus two step scattering from all other particles.

In any event, as can be seen from the results, the depolarization, δ, was less than 1 percent for a 1.2 mm diameter iris aperture, giving a field of view of approximately 1 miliradians, or easily larger than the minimum necessary to encompass the transmitted beam divergence of 0.5 miliradians.

While this depolarization is small, the resultant errors are even smaller, since as seen in the error analysis, the maximum fractional error in pollution concentration measurement would be typically 10 x $(\delta_1 - \delta_2)$, where δ_1 is the depolarization signal received from the start of a sample

region Δr, and δ_2 is the depolarization signal received from the end of the sample region. Now in no case was $\delta_1-\delta_2>0.001$ for sampling region of 100 meters. This means that a maximum error of 1 percent could be introduced in pollution measurements as a consequence of depolarization differences between on end of a 100 meter sample region to the other. Even for larger 500 meter sample lengths no depolarization differences $(\delta_2-\delta_1)>0.002$ were observed, i.e. resulting in potential maximum errors of 2 percent in pollution measurements. Needless to say error contributions of these levels are certainly acceptable in DASE Lidar systems, being below errors due to other factors (e.g. defocussed scope traces).

5.4 Simultaneous Twc Wavelength measurments of Atmospheric NO_2

A series of field tests were carried out with the polarization discrimination DASE Lidar to measure the atmospheric NO_2 pollution in a path extending from the CCNY laboratory window out over the eastern side of upper Manhattan. The purpose of these tests was not to carry out an extended pollution survey, but simply to demonstrate the viability of utilizing polarization discrimination techniques with the DASE Lidar, to carry out time resolved atmospheric pollutant measurements of this type.

To carry out these tests, the Lidar arrangement was that of Figures 4.2.1 and 4.4.1, described in sections 4.2, and

4.4 and set up to simultaneously emit two orthogonally polarized colinear laser beams at two wavelengths: 4478.5 Å and 4500 Å, corresponding to a prominent peak and trough of the NO_2 absorption line respectively. The Lidar receiver was designed as described in section 4.2, Figure 4.2.1 to separate each of the two backscattered signals by means of the calcite beam splitter and detect them simultaneously by photomultipliers covered by wide band (50 Å filters). The outputs from the photomultipliers were displayed on storage scopes.

Typical scope curves obtained for the backscattered signals are shown in Figures 5.4.1. Some of the typical pollution measurements derived from the results of the series of tests are shown in table 5.4.1. The results are comparable to these previously obtained using narrow band filters, and serve the purpose of the experiment, namely to demonstrate the viability of utilizing polarization discrimination for the DASE Lidar approach.

It might be noted that pollution values obtained were compared to data obtained from the New York Department of air resources and as in the case of previous narrow band filter measurements were generally found to be within $\mp$ 20 percent for the samples chosen.

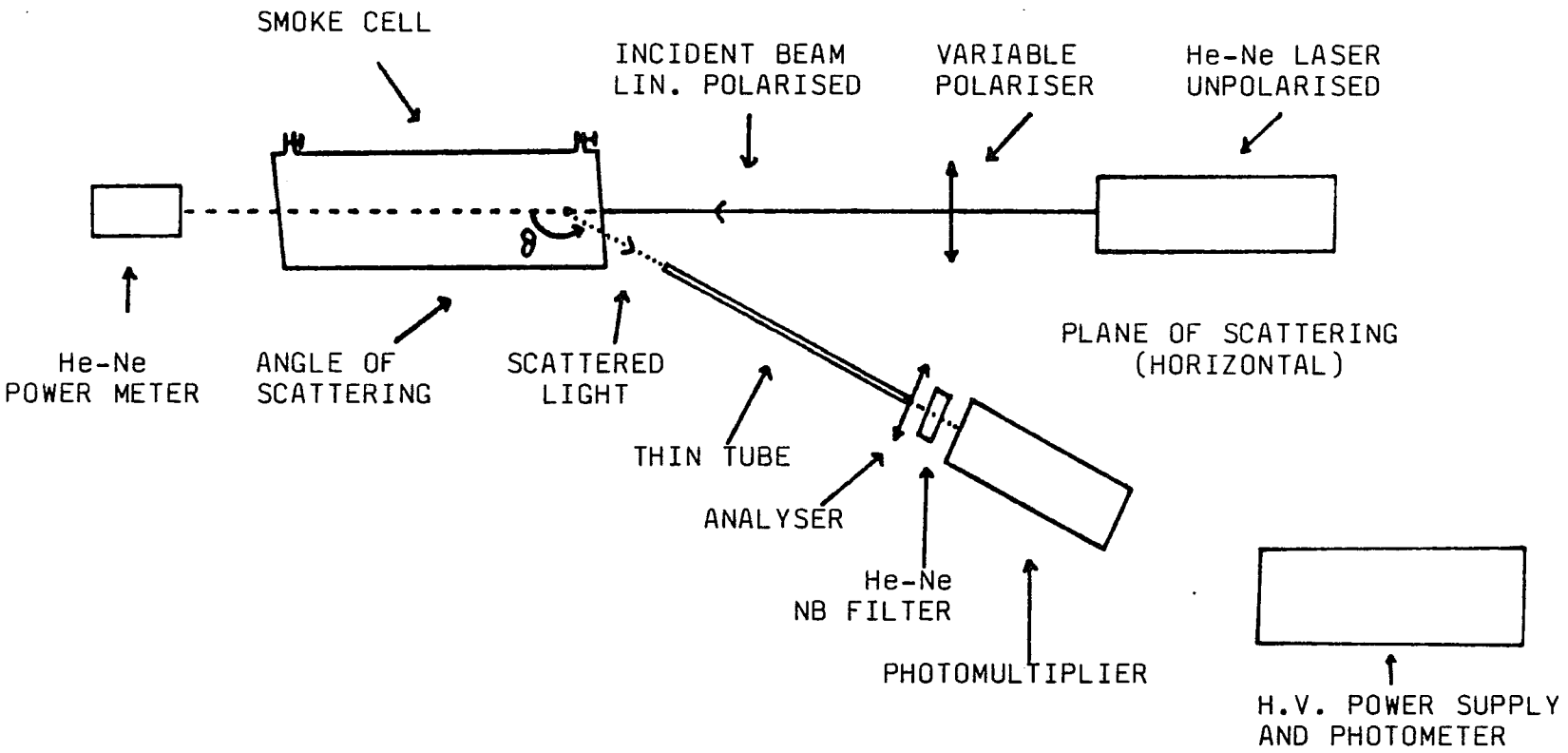

FIGURE 5.2.1 Experimental setup for depolarization measurements of He-Ne laser light scattered by smoke particles at different angles.

FIGURE 5.2.2 Photograph of the experimental setup for depolarization measurements of He-Ne laser light scattered by smoke particles.

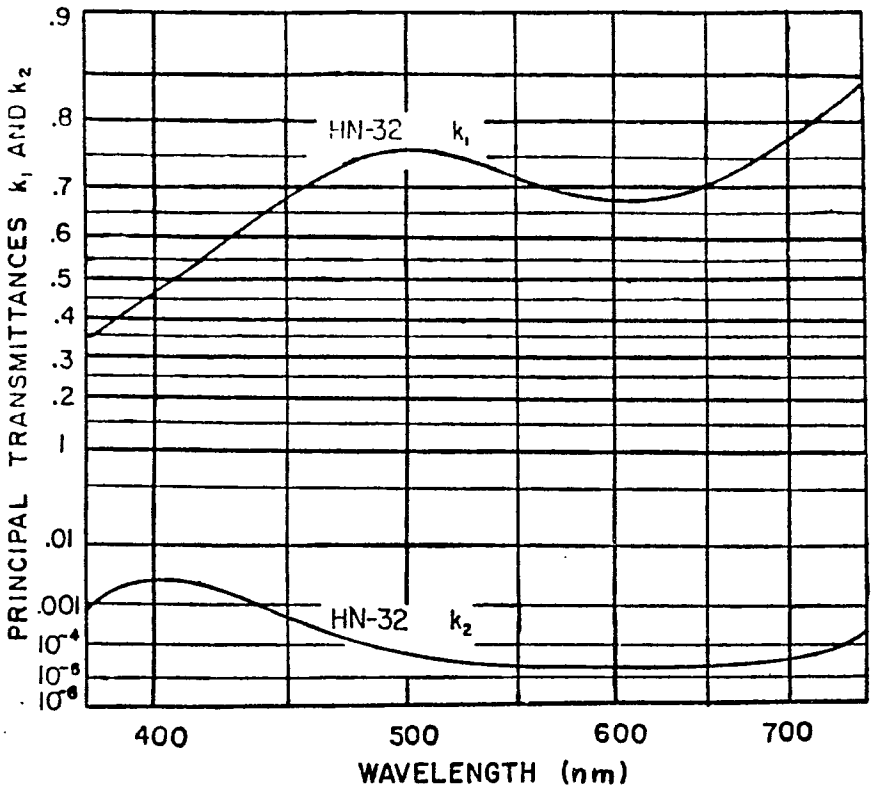

FIGURE 5.2.3 Dependence of the principal transmittances k_1 and k_2 on the wavelength in the visual range for HN-32 polarizer. The vertical scale is linear in log(1/k).

Wavelength (nm)	k_1	k_2
375	.33	.001
400	.47	.003
450	.68	.000,5
500	.75	.000,05
550	.70	.000,02
600	.67	.000,02
650	.70	.000,02
700	.77	.000,03
750	.84	.000,2

TABLE 5.2.1 Principal transmittance values k_1 and k_2 for HN-32 polarizer at representative wavelengths in the visual range.

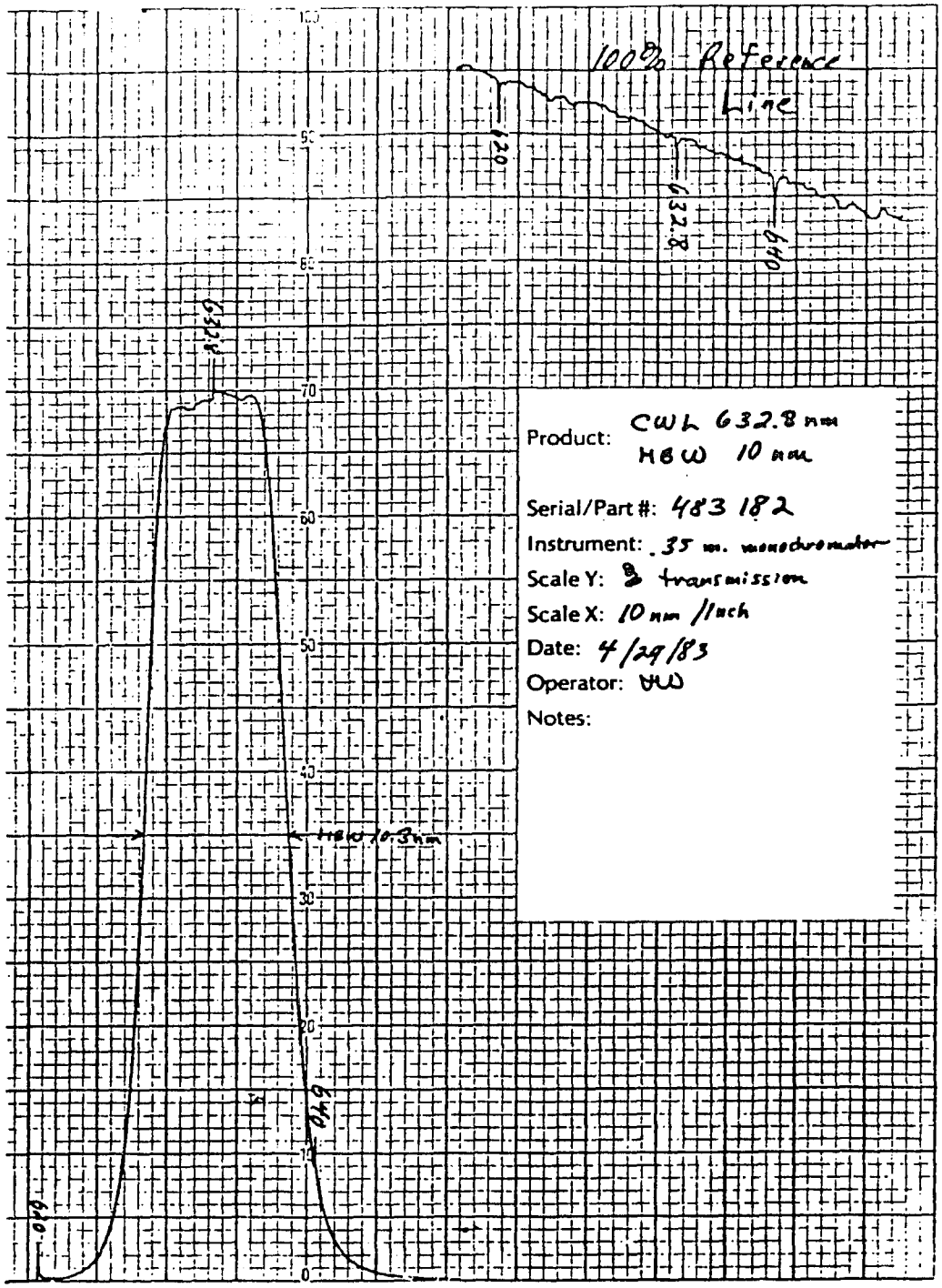

FIGURE 5.2.4 Spectral responce of the He-Ne filter used in the receiver for the experiment of scattering by smoke particles.

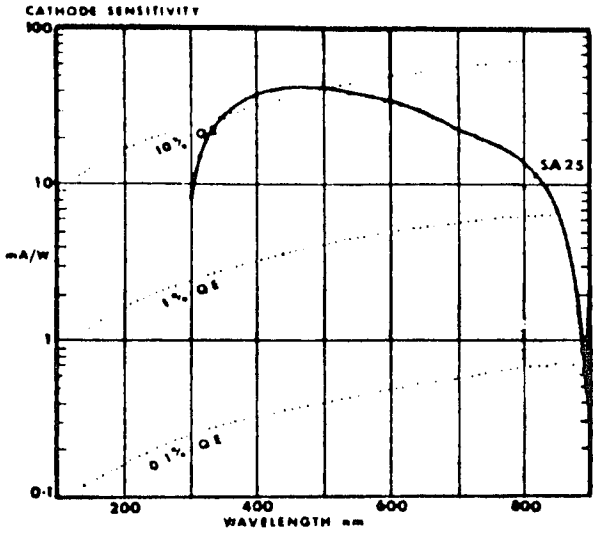

FIGURE 5.2.5a

Typical Cathode Sensitivity vs Wavelength for a Centronic Q4283SA-25 Photomultiplier.

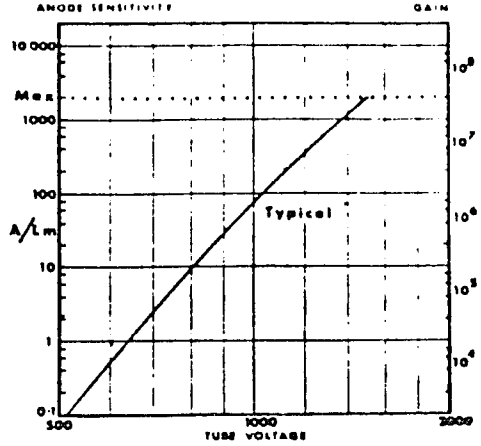

FIGURE 5.2.5b

Typical Anode Sensitivity and Gain vs tube Voltage for a Centronic Q4283SA-25 Photomultiplier.

OPERATING CONDITIONS	NORMAL	LIMIT
ANODE SENSITIVITY (A/Lm)	200	2000
ANODE CURRENT	10uA	1mA
CATHODE CURRENT	--	50uA
MAX. TEMPERATURE	30°C	70°C
MIN. TEMPERATURE	-60°C	-18°C
CATHODE-DI VOLTAGE	150V	300V
SUPPLY VOLTAGE		

TABLE 5.2.2 Operating Conditions for a Q428SA-25 Centronic Photomultiplier.

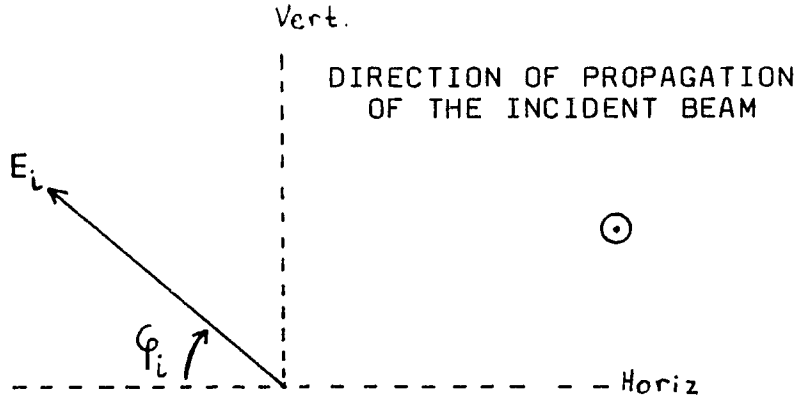

FIGURE 5.2.6a Polarization angle of the incident linearly polarized light with respect to the plane of scattering (Horizontal).

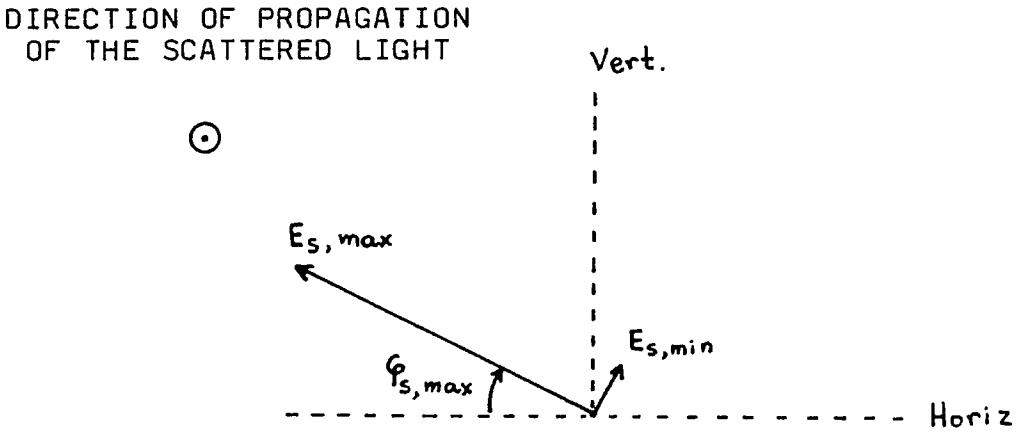

FIGURE 5.2.6b Orientation of the semiaxes of the polarization ellipse, with respect to the plane of scattering, for light scattered by smoke particles.

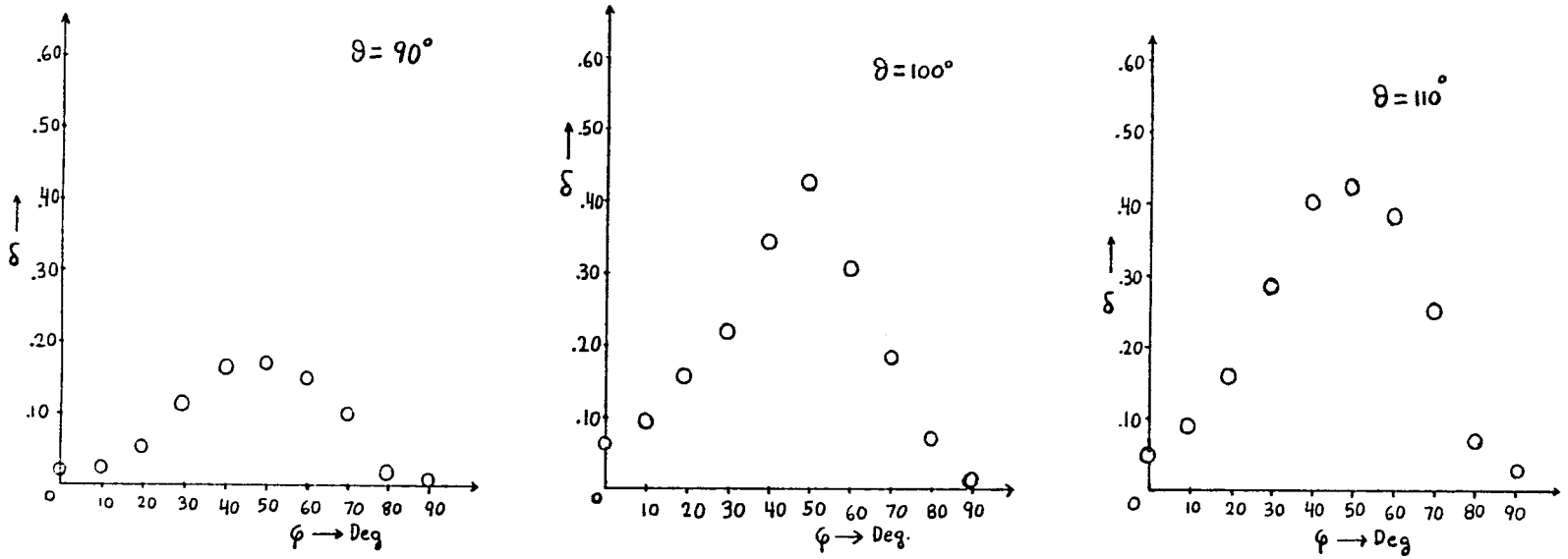

FIGURE 5.2.7a Depolarization of linearly polarized light scattered by smoke particles Vs the polarization angle of the incident light with respect to the plane of scattering, at different angles of scattering.

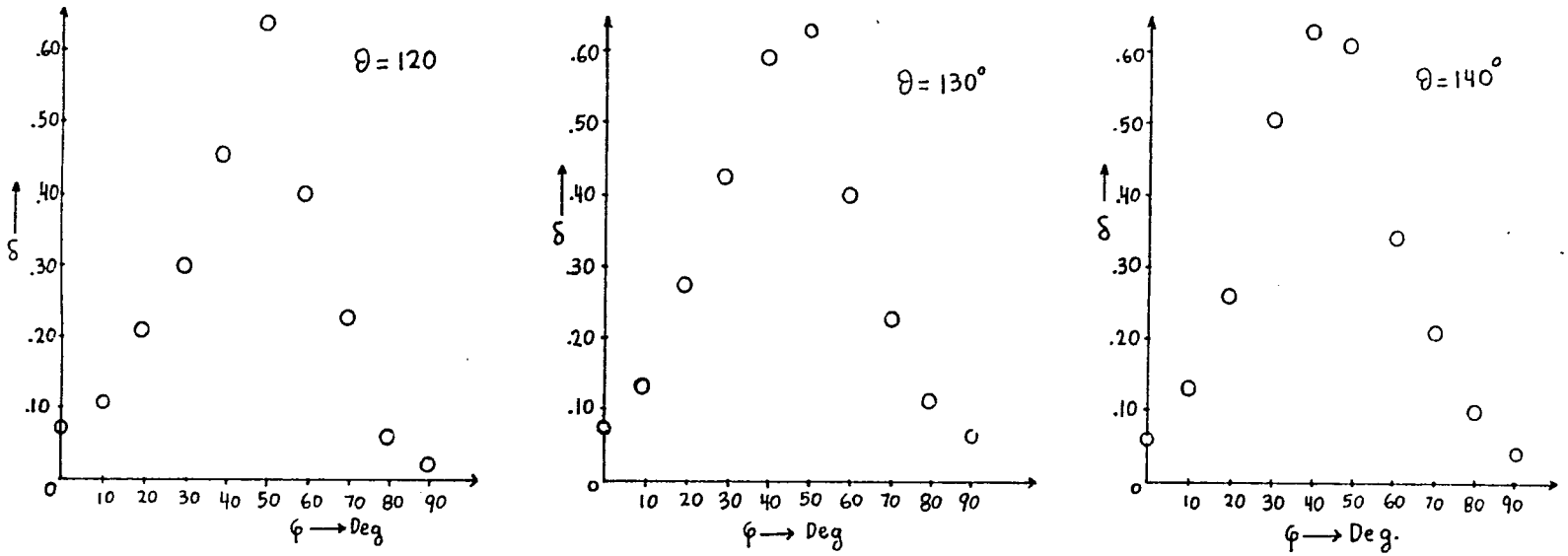

FIGURE 5.2.7b Depolarization of linearly polarized light scattered by smoke particles Vs the polarization angle of the incident light with respect to the plane of scattering, at different angles of scattering.

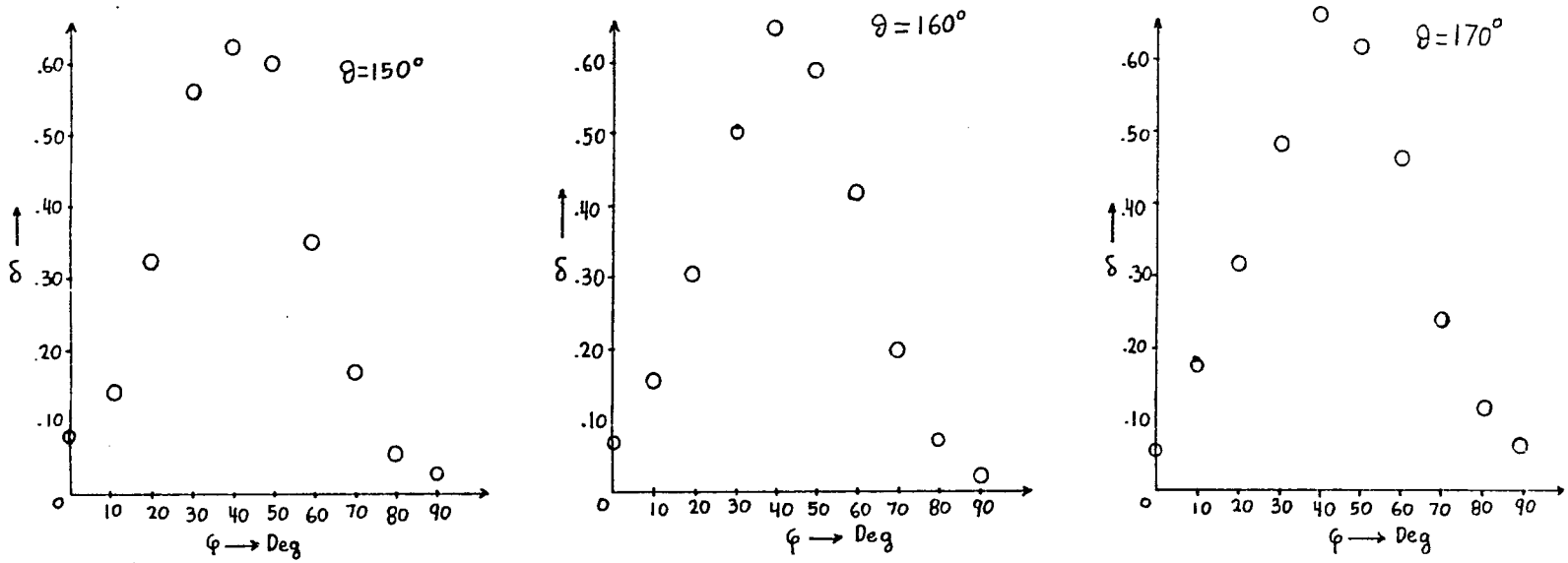

FIGURE 5.2.7c Depolarization of linearly polarized light scattered by smoke particles Vs the polarization angle of the incident light with respect to the plane of scattering, at different angles of scattering.

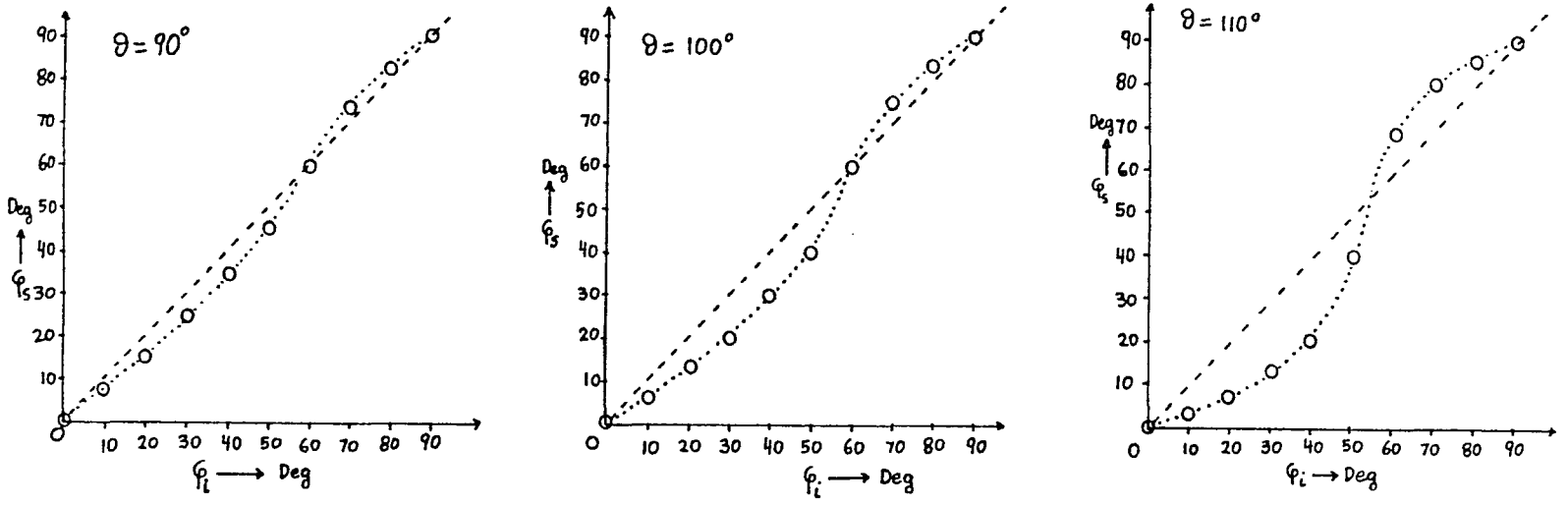

FIGURE 5.2.8a Orientation angle of the major axis of the polarization ellipsis of light scattered by smoke particles, Vs the incident polarization angle, for different scattering angles. Comparison with the case of reflection at the same angles (straight line).

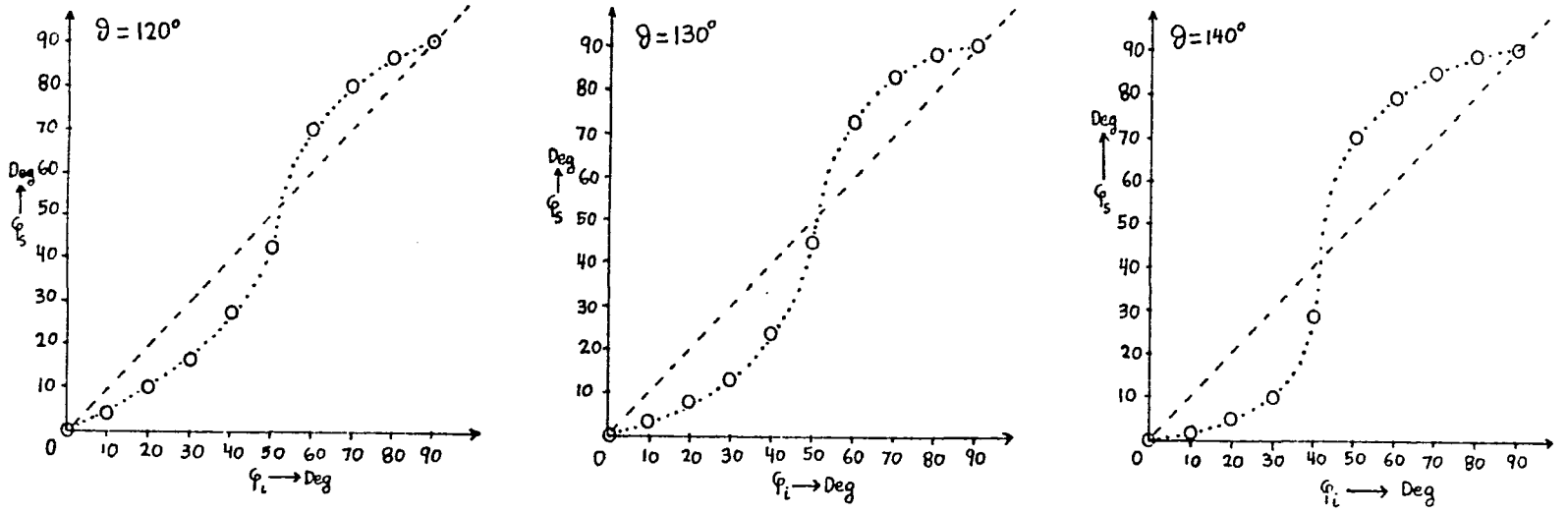

FIGURE 5.2.8b Orientation angle of the major axis of the polarization ellipsis of light scattered by smoke particles, Vs the incident polarization angle, for different scattering angles. Comparison with the case of reflection at the same angles (straight line).

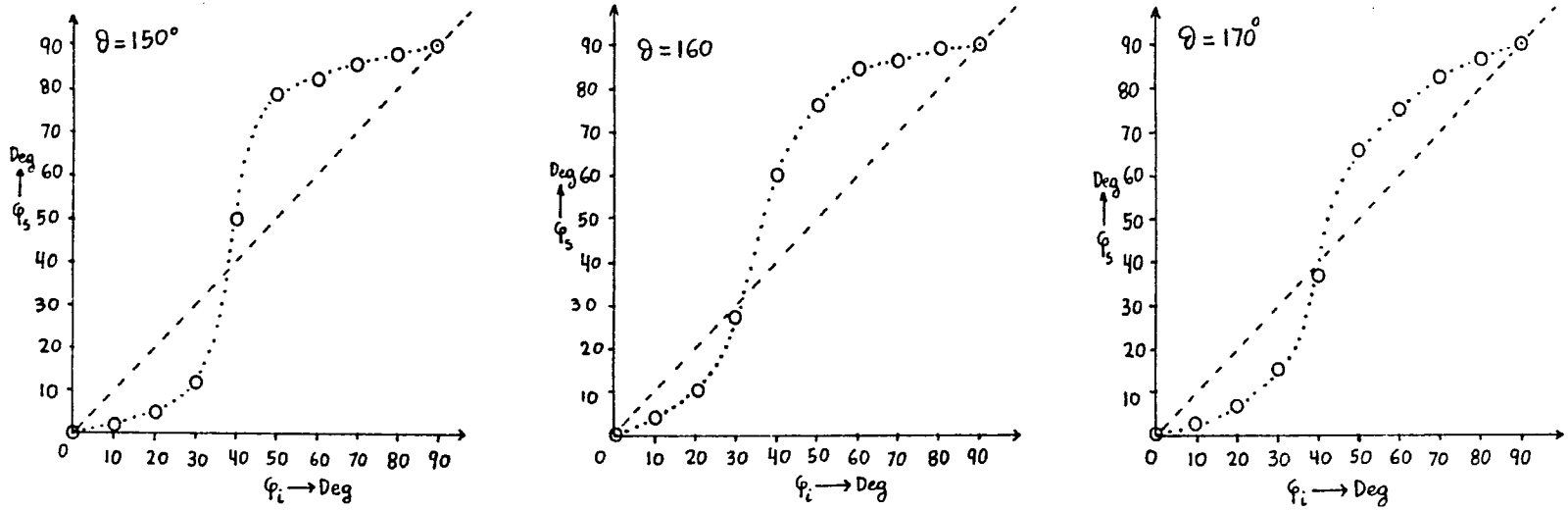

FIGURE 5.2.8c Orientation angle of the major axis of the polarization ellipsis of light scattered by smoke particles, Vs the incident polarization angle, for different scattering angles. Comparison with the case of reflection at the same angles (straight line).

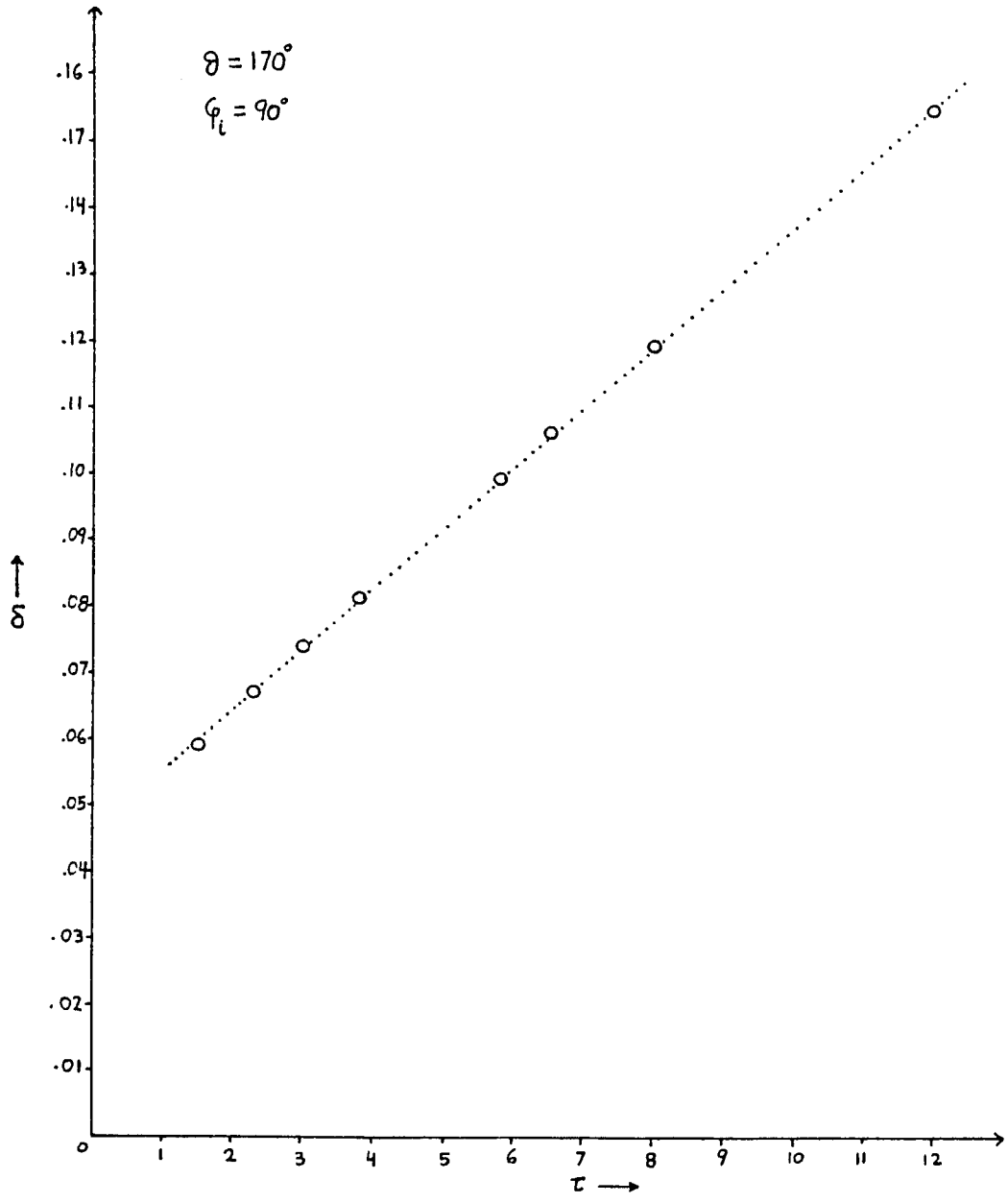

FIGURE 5.2.9a Depolarization of linearly polarized light scattered by smoke particles Vs the optical thickness of the scattering medium.

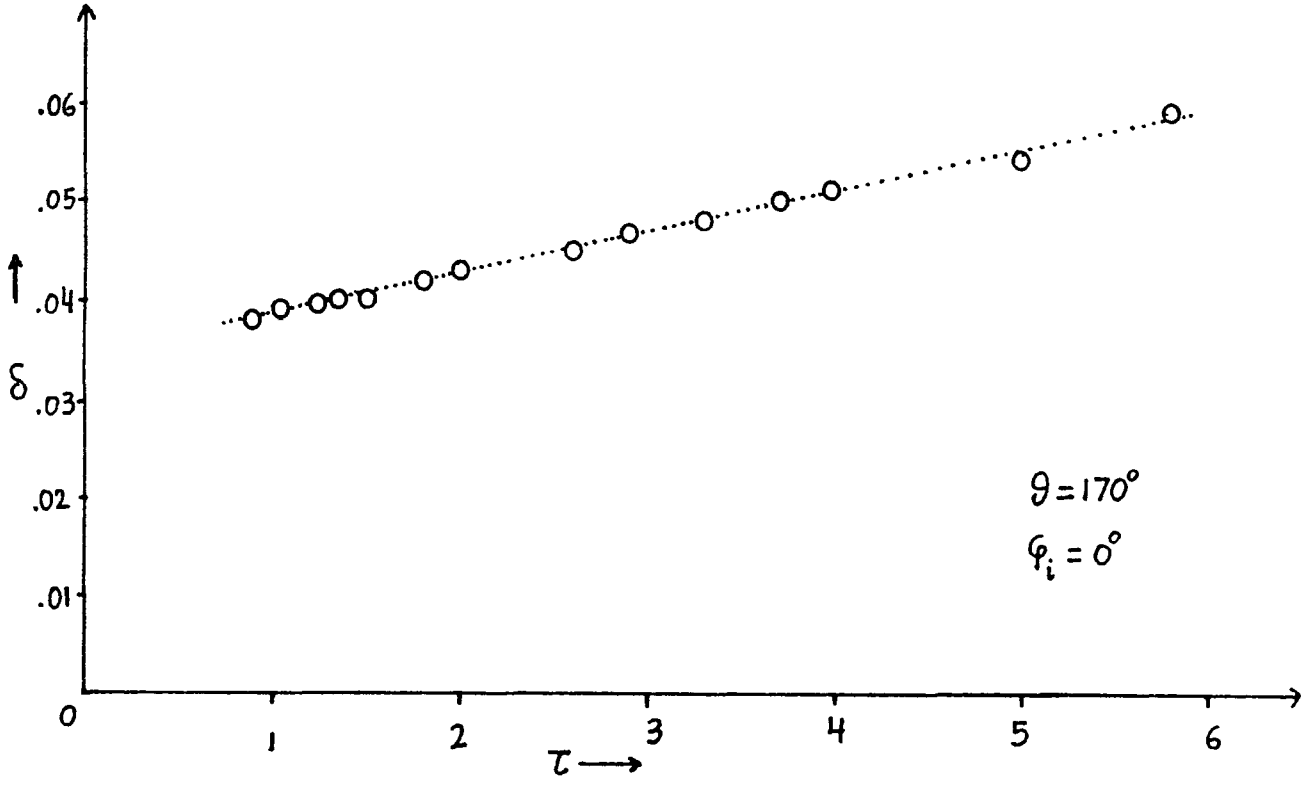

FIGURE 5.2.9b Depolarization of linearly polarized light scattered by smoke particles Vs the optical thickness of the scattering medium.

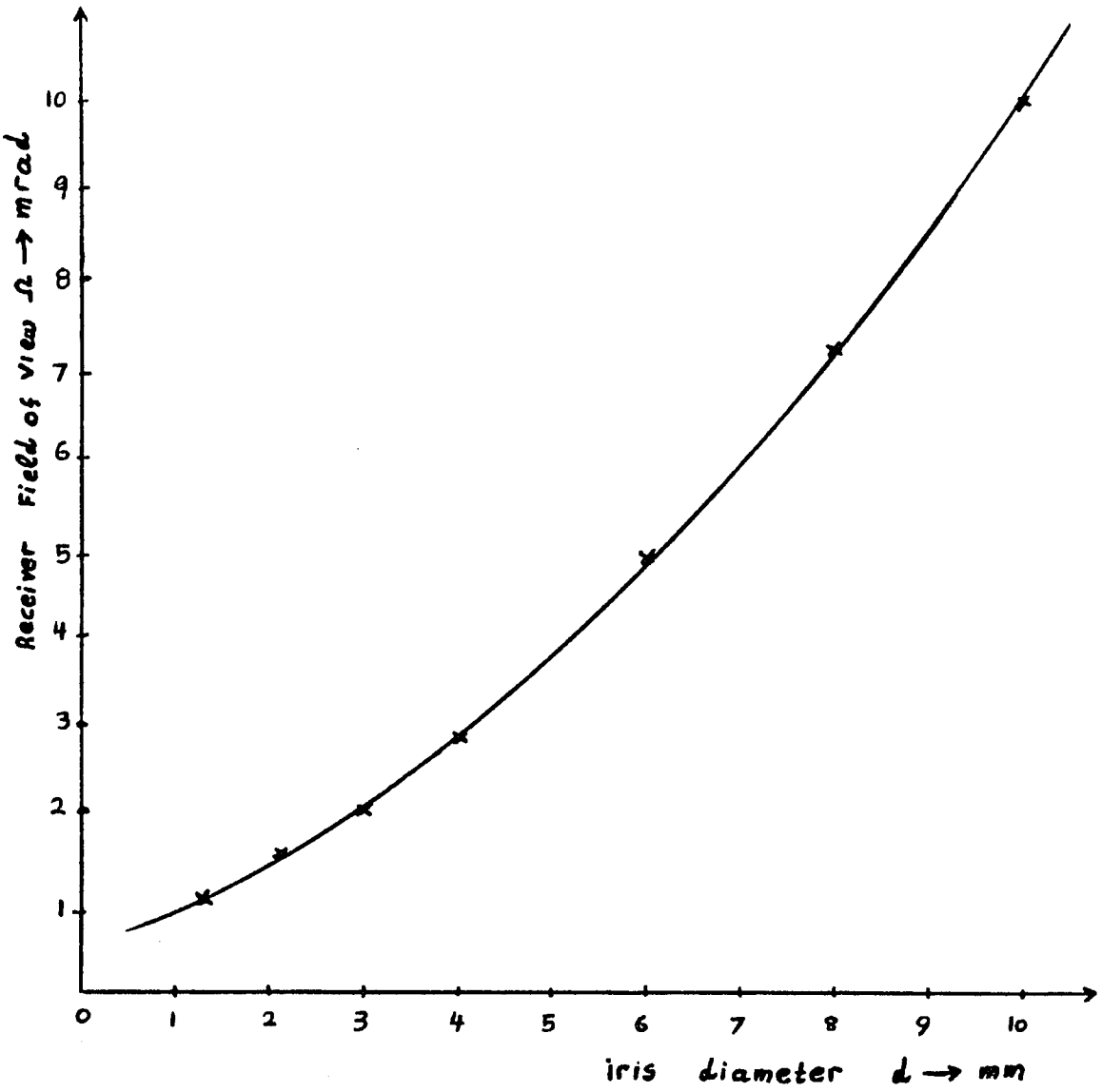

FIGURE 5.3.1 Field of view of the optical receiver versus aperture diameter.

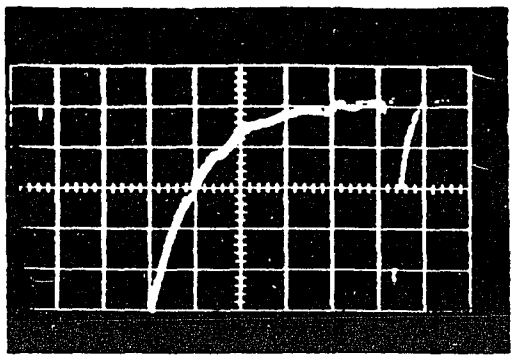

PARALLEL COMPONENT
APERTURE DIAMETER : 10 mm

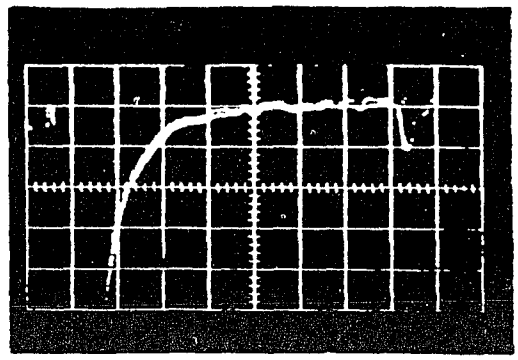

CROSS - POLARISED COMPONENT
APERTURE DIAMETER: 10 mm

WAVELENGTH : 4500 Å
2 mV / DIV
1 μsec / DIV

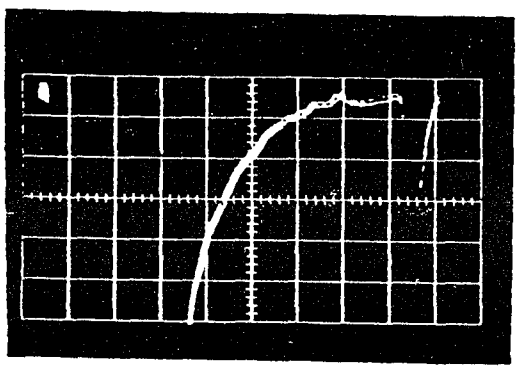

PARALLEL COMPONENT
APERTURE DIAMETER : 2 mm

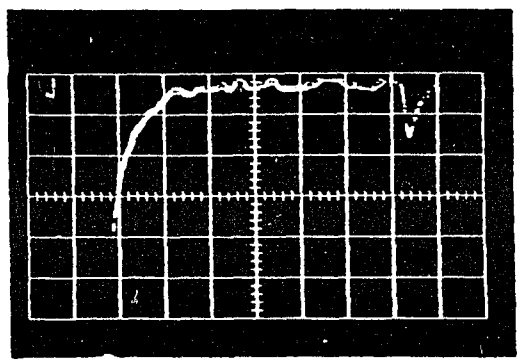

CROSS - POLARISED COMPONENT
APERTURE DIAMETER : 2 mm

FIGURE 5.3.2a Parallel and cross polarized backscatter components for 2 and 10 mm receiver aperture sizes.

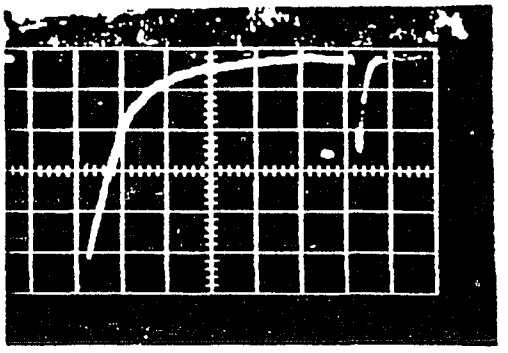

IRIS DIAMETER : 2 mm

PARALLEL COMPONENT
WAVELENGTH : 4500 Å
10 mV/DIV
2 μsec/DIV

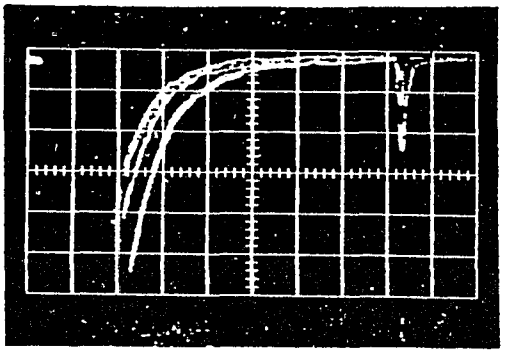

IRIS DIAMETER

UPPER CURVE : 0.5 mm
MIDDLE CURVE : 1 mm
LOWER CURVE : 2 mm

FIGURE 5.3.2b Decrease of received power for receiver aperture sizes below 1 mm.

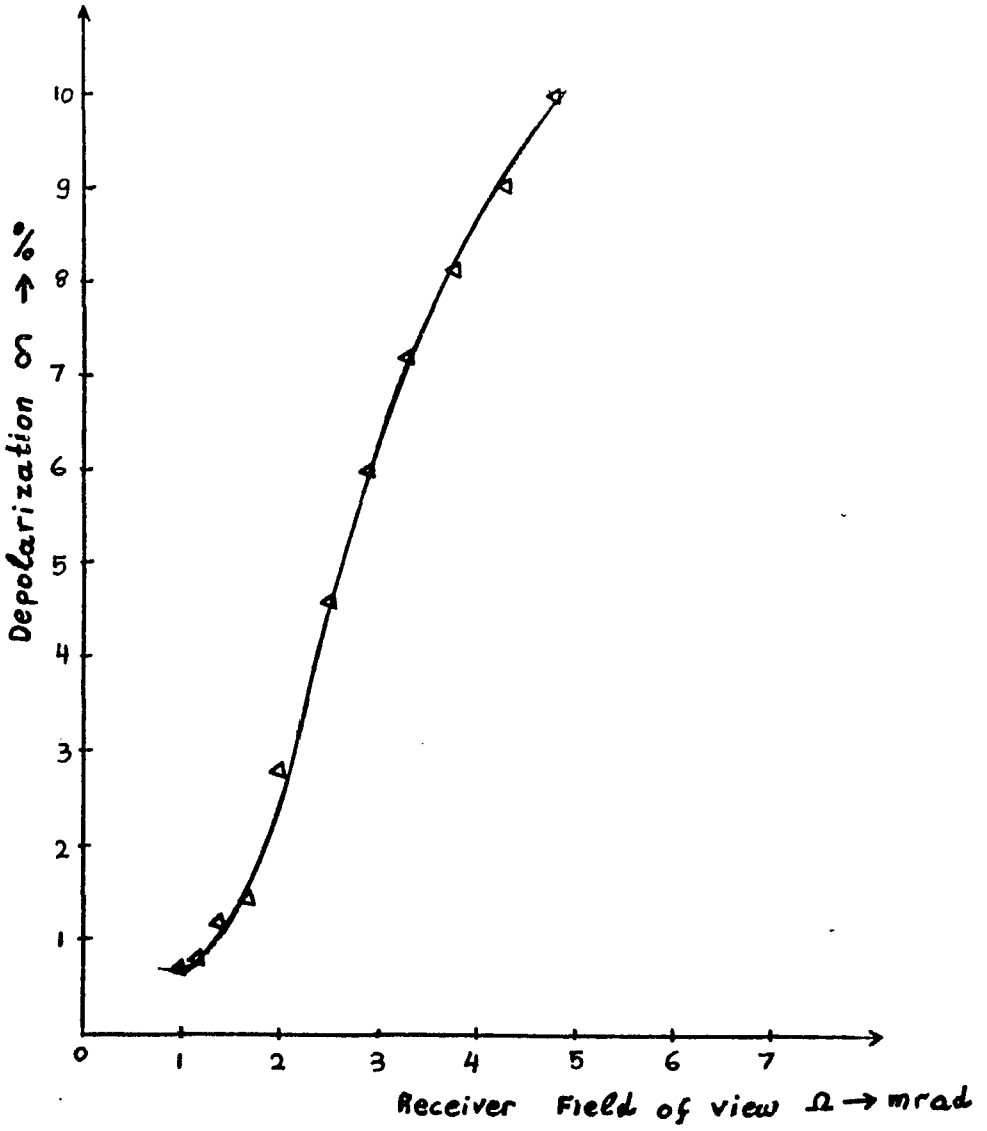

FIGURE 5.3.3a Depolarization of backscattered signal versus receiver field of view.

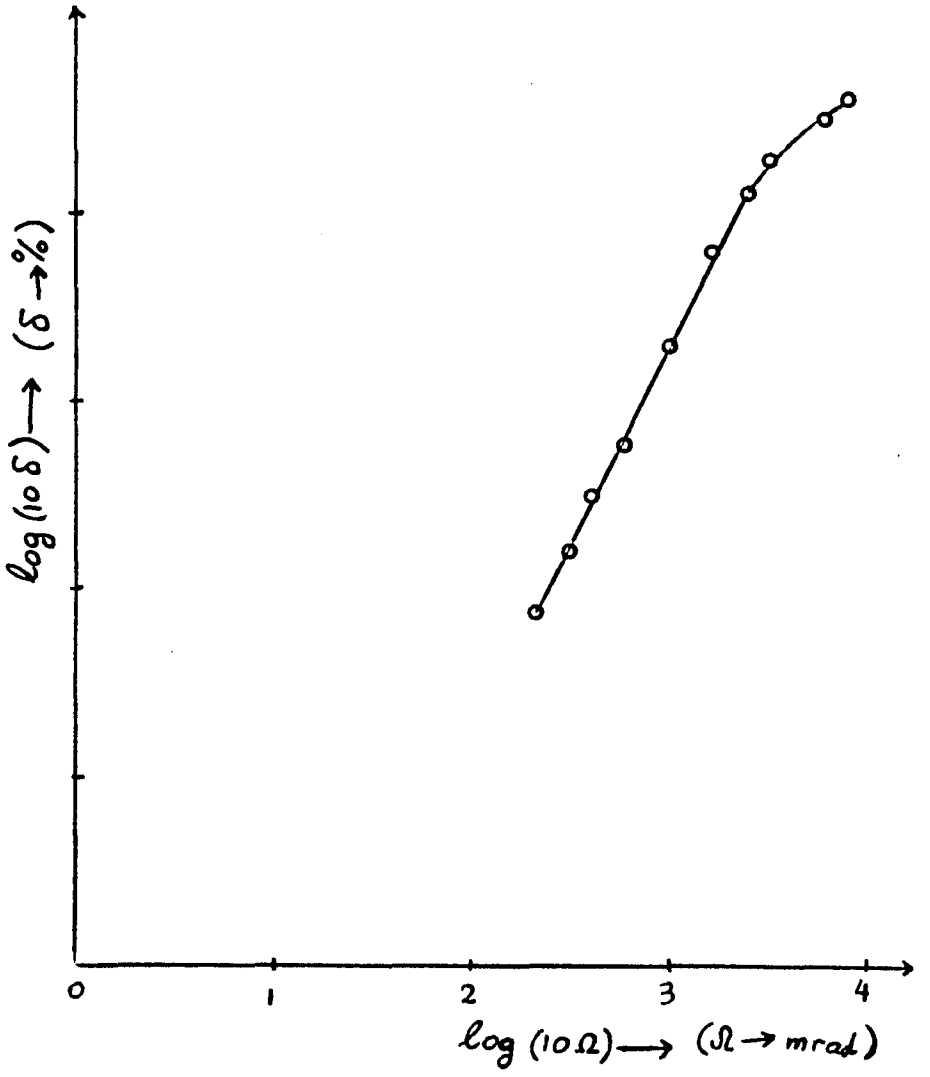

FIGURE 5.3.3b Logarithmic variation of depolarization with respect to the field of view of the receiver.

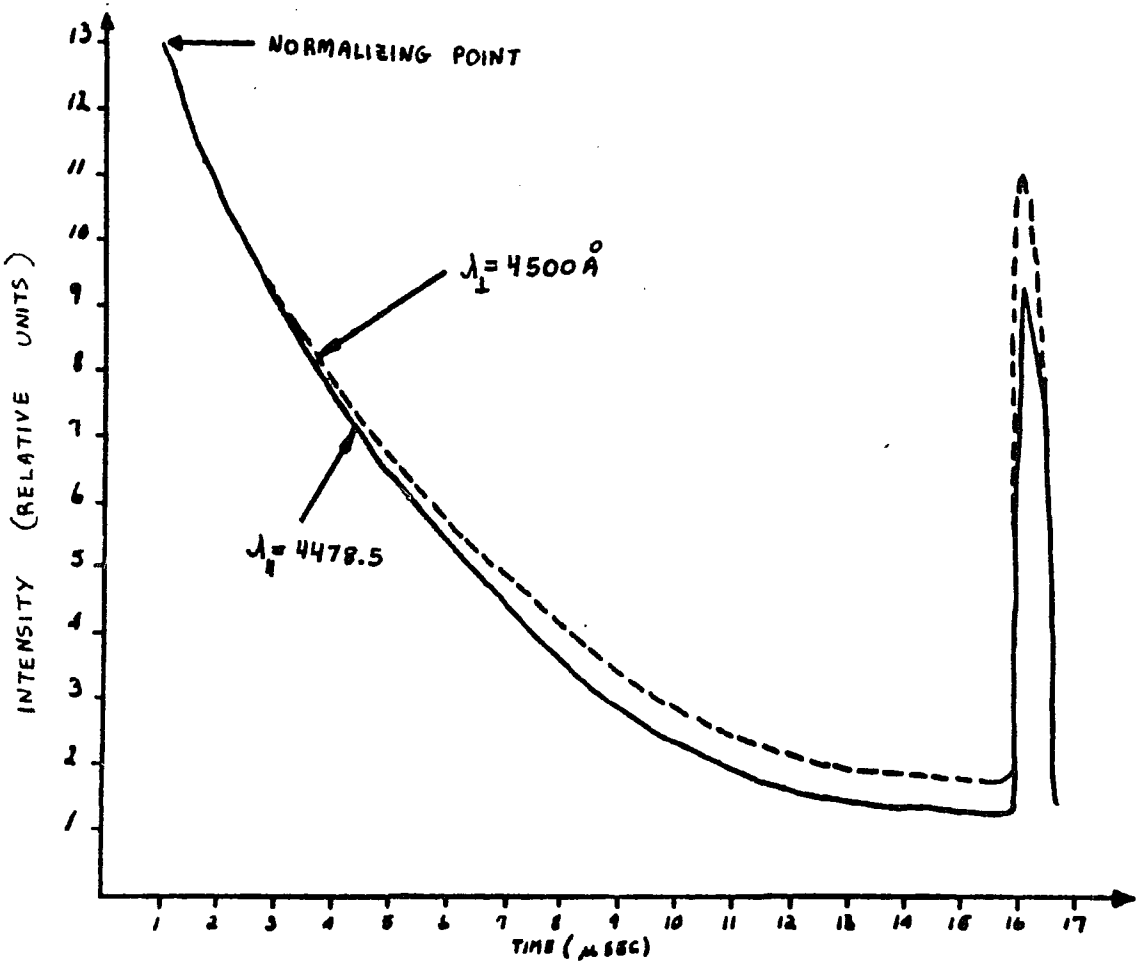

FIGURE 5.4.1 Typical Lidar returns at the two wavelengths 4500 A and 4478.5 A.

	Time	NO_2 Concentration (ppm)
Range 1000m	9.00 AM	0.26
Resolution 200m	5.00 PM	0.28
	6.00 PM	0.20
	8.00 PM	0.12
Range 500	9.00 AM	0.20
Resolution 200	5.00 PM	0.16
	6.00 PM	0.14
	8.00 PM	0.12

TABLE 5.4.1 Range, Resolution, NO_2 Pollution concentration for various times during the day.

CHAPTER 6

SUMMARY AND CONCLUSIONS

The basic objective of the work reported was to analyse the basic requirements for a polarization discrimination DASE scheme, for atmospheric molecular pollution monitoring, and to examine the atmospheric factors which affect these requirements, and, based on this analysis, to design construct and demonstrate an operating, polarization discrimination DASE Lidar system. Following a detailed analysis of atmospheric elastic scattering and polarization effects and comprehensive error analysis, a polarization discrimination DASE Lidar system was designed built and successfully used to test out the basic design premises, through atmospheric backscatter depolarization field measurements, as well as to demonstrate the operational viability of the system in field measurements of atmospheric Nitrogen Dioxide concentrations.

The polarization discrimination approach was evolved to overcome some of the limitations of previously existing DASE systems and to extend their applications and versatility. In the polarization discrimination approach, Lidar outputs are emitted simultaneously at two close-lying wavelengths, with the outputs orthogonally polarized. The output wavelengths correspond to a peak and trough in the absorption spectrum of the pollutant being monitored. The concentration of

pollutant is determined by measuring the relative attenuations of the Lidar backscattered signals at each of the wavelengths as they traverse the sample region. To be able to measure these relative attenuations, it is necessary to be able to separate and measure separately each of the backscattered signals. The premise of the polarization discrimination scheme is, that backscattered signals retain sufficiently the initial polarizations of the outgoing signals to permit polarization discrimination techniques, alone, to be used to separate the return signal at each of the two wavelengths.

To examine the basic feasibility of the polarization discrimination scheme, atmospheric scattering features, and their effect in depolarization of backscatter, were examined in some detail. Included in this examination was Rayleigh backscatter from atmospheric molecules and water vapor, Mie (particulate) backscatter from particles with sizes both comparable and large with respect to wavelength, with symmetric and non-symmetric shapes, as well as multiple scattering processes. From this examination it was determined that depolarization effects were to be expected primarily from 180^{o} backscatter from non-symmetric small particles, as well as from multiple scattering (two-step) from particles of all sizes and shapes.

A comprehensive error analysis was also carried out to determine the impact of such depolarization in backscatter as may be found to exist, on the accuracy of measurements

with the polarization discrimination DASE scheme. Because of the relative nature of measurements used in the scheme, it was found that errors introduced by undesirable depolarization backscatter were likely to be limited to negligible values.

The polarization discrimination system was then built using a polarizing beam splitter in the laser cavity to produce orthogonally polarized laser outputs at two close-lying wavelengths. A similar arrangement was designed for the Lidar receiver, where the separated signals were detected by separate photomultipliers.

Measurements on backscatter depolarization, a factor of key importance in the approach used, were then carried out both in laboratory tests and field tests. In the laboratory tests, it was found that backscatter, from particles large compared with the wavelength, retained a large degree of specularity as far as polarization was concerned. This meant that 180^{o} backscatter largely retained the initial incident polarization. Atmospheric field tests showed depolarization consistent with a picture of 180^{o} backscatter depolarization plus depolarization due to multiple scatter. The latter effect was the predominant one, and could be largely eliminated by reducing the optical receiver aperture to match the 1 miliradian divergence of the outgoing Lidar beam.

Under these conditions, the depolarizations measured in backscattered signals were of the order of 1 percent. Taken

in conjuction with the error analysis, it is found that undesirable backscatter depolarization effects can be neglected as a practical source of error in a polarization discrimination DASE Lidar system.

Finally field experiments were carried out, to measure, from the laboratory window, concentrations of nitrogen-dioxide at kilometer ranges over the upper East Side of Manhattan. The results of these experiments, which measured pollution concentrations of low ppm demonstrated the viability of the polarization discrimination DASE Lidar system.

REFERENCES

1. R. Perry, R.J Young, "Handbook of Air Polution Analysis", John Wiley & Sons, Halsted Press, (1977).

2. A. Stern, "Air pollution", Third Edition, Vol. 3, Academic Press N.Y. (1976).

3. W.F. Herget, W.D. Conner, Environmental Science Technology, 11, No. 10, Oct., (1977).

4. B.B. Snavely, Proc. IEEE, 57, Aug., (1969), p. 1374.

5. R. Bureau, Meteorologie (Paris), 3, (1946), p. 292.

6. S.S. Frieland, J. Katzenstein and M.R. Zatzick, J. Geophys. Res., 61, (1956), p. 415.

7. M.H. Horman, J. Opt. Soc. Amer., 51, (1961) p. 681.

8. G. Fiocco and L.O. Smullin, Nature 199, (1963), p. 1275.

9. M.G.H. Lingda, Proc. 1st Conference on Laser Technology, 1, (1963), p. 63.

10. D.A. Leonard, Nature, 216, (1967), p. 142.

11. T. Kobayashi and H. Inaba Appl. Phys. Letts. 17, (1970), p. 139.

12. T. Hirschfeld, Appl. Opt., 13 (1974), p. 1435.

13. H.J. Bernstein, Paper presented at the 1973 Spring Meeting of the Optical Society of America, N.Y., April, 11-13.

14. H.P. Rosen, R. Robrish and O. Chambelain, "Feasibility of the Remote Detection of Pollutants Using Resonance Raman Scattering", Lawrence Berkeley Lab., Energy and Environment Div., U.C. Berkeley, California (1975).

15. P.L. Hanst and J.A. Morreal, J. Air Pollut. Cont. Ass., 18, (1968), p. 754.

16. H. Kildal and R.L. Byer, Proc. IEEE, 59, (1971), pp. 1644-1663.

17. T. Henningsen, M. Garbuny and R.L. Byer, Appl. Phys. Letts, 24, (1974), p. 242.

18. M.R. Bowman, A.J. Gibson and M.C.W. Sandford, Nature, 221, (1969), p. 456.

19. J.A. Geldwachs, M. Birnbaum, A.W. Tucker and C.L. Ficher Opto-Electronics, 4, (1972), p. 155.

20. R.M. Schotland, E.E. Chermack and D.T. Chang, Proc. First International Symp. of Humidity and Moisture p. 569, (Reinhart Bood Div., New York, N.Y. (1964),

21. R.M. Schotland, Proc. Third Symp. on Remote Sensing of the Environment, Oct. 14-16 (1964), p. 215, Univ. of Michigan, Ann Arbor, Mich.

22. R.L. Byer and M. Garbuny, Appl. Opt., 12, (1973), p. 1496.

23. R.L. Measures and G. Pilon, Opto-Electronics, 4, (1972), p. 141.

24. S.A. Ahmed and J.S. Gergely, "Laser Radar Study Using Resonance Absorption for Remote Detection of Air Pollutants", Fifth Conf. on Laser Radar Studies of Atm., June 4-6 (1973), Williamsburg, Va.

25. S.A. Ahmed, Appl. Opt., 12, (1973), p. 901.

26. M.L. Wright et al. Final Report for NASA CR-132724, "Air pollution measurement by Active Remote Sensing Techniques", Contract NA SI-11657, Stanford Research Institute, Menlo Park, Ca., (1976).

27. T. Igarashi, "Laser Radar Study Using Resonance Absorption for Remote Detection of Air Pollutants", Fifth Conf. on Laser Radar Studies of the Atm., June 4-6 (1973) Williamsburg, Va.

28. R. Byer, Opt. and Quant. Elect., 7, (1975), p. 147.

29. W.B. Grant, R.D. Hake, Jr., E.M. Liston, R.C. Robbins and E.K. Proctor, Jr., Appl. Phys., Letts., 24, (1974).

30. Igarashi T., Fifth Conference on Laser Radar Studies of the atmosphere, Abstracts, p. 57, June (1973), Williamsburg, Va.

31. H. Inomata and T. Igarashi, Journal of the Radio Research Laboratories, 21, No. 107, (1974), p. 573.

32. Junge C.E., Air Chemistry and Radioactivity, Academic Press, New York, (1963).

33. K. Bullrich, Advances in Geophysics, Vol. 10, ed. by L. Landsberg, Ch. 3, (1964), Academic Press, New York.

34. "Handbook of Optics", ed. by Walter G. Driscoll, McGraw Hill book Co., New York, pp 14.3-14.9.

35. Volz F.E., Appl. Opt., 11, (1972), p. 755.

36. Kerker M.,"The Scattering of light", Academic press New York, pp. 35, 47.

37. Van De Hulst, Light Scattering by Small particles , John Wiley Sons, New York, pp. 119-129.

38. R.T. Menzies, Appl. Opt., 10, (1971), p. 1532.

39. Davis J.I., Appl. Opt., 5 (1), Jan. 1966, pp. 139-147.

40. W.K. Pratt, Laser Communication Systems, Wiley, N.Y. (1969).

41. R.M. Schotland, J. Appl. Meteorology, 13, (1974), pp. 71-77.

42. T.D. Wilkerson, B. Ercoli and F.S. Tomkins, Absorption Spectra of Atmospheric Gases , Tech, Note BN-784, Institude for Fluid Dynamics and Applied Mathematics, Feb., (1974).

43. R.M. Schotland, J. Appl. Meteorology, 13, (1974), pp. 71-77.

44. H. Hodara, Proc. IEEE, 54, No. 3, March (1966), pp. 368-375.

45. A.A.M Saleh, IEEE J. Quant. Electronics, Vol. QE-3, No. 11, Nov. (1967), pp. 540-542.

46. J. Strohbehn, S. Clifford, IEEE Trans. Antennas and Propag., Vol. AP-15, No. 3, May (1967), pp. 416-421.

47. Davies, M.,"Some Electrical and Optical Aspects of Molecular Behavior", Oxford, Pergamon Press, (1965), p. 133.

48. Stuart, H.A. Die Struktur des Freien Melekuels, Berlin Springer Verlag, (1952), p. 609.

49. P. Beckmann,"The depolarization of electromagnetic Waves", The Golem Press, Boulder, Co. (1968).

50. S.A. Ahmed, J.S. Gergely and F. Barone, "Remote monitoring of Gaseous pollutants by differential Absorption Laser techniques", EPA-600/2-80-049, Feb. 1980.